CNWRA *A center of excellence in earth sciences and engineering*

A Division of Southwest Research Institute®
6220 Culebra Road • San Antonio, Texas, U.S.A. 78228-5166
(210) 522-5160 • Fax (210) 522-5155

May 20, 2003
Contract No. NRC–02–02–012
Account No. 20.06002.01.091

U.S. Nuclear Regulatory Commission
ATTN: Mr. Jeffrey Pohle
Division of Waste Management
TWFN, Mail Stop 7-D13
Washington, DC 20555

SUBJECT: Thermal Effects on Flow KTI Intermediate Milestone 06002.01.091.310: Modeling In-Drift Environmental Conditions—Letter Report

Dear Mr. Pohle:

Enclosed please find the report titled "Laboratory and Numerical Modeling of the Cold-Trap Process." This report fulfills the requirements for the subject milestone, which is due May 21, 2003.

This report summarizes the data collected from the laboratory cold-trap experiment and associated modeling. Since similitude cannot be strictly followed, an extensive discussion of thermal scaling issues is included in this report. Analytical and computational fluid dynamics models were developed to simulate the laboratory experiment. The test demonstrated that the cold-trap process is viable and should be considered in evaluating the environmental conditions in the emplacement drifts at Yucca Mountain. Convective movement of air under a range of temperature gradients led to condensation downgradient from the heat source. The methods described in this report will be used to develop and analyze larger-scale experiments, including the analysis of the DOE natural convection laboratory experiment at the Atlas Facility in North Las Vegas, Nevada. This work will support the review of DOE and NRC technical agreements TEF.2.04 and TEF.2.05, which cover the effect of the cold-trap process on process models and performance assessment models.

If you have any questions, please contact Randall Fedors at 210-522-6818 or me at 210-522-5151.

Sincerely yours,

Asadul H. Chowdhury, Manager
Mining, Geotechnical, and Facility Engineering

AHC/ph
Enclosure
cc: M. Leach, D. DeMarco, B. Meehan, E. Whitt, W. Reamer, L. Campbell, A. Campbell, J. Schlueter, K. Stablein, D. Brooks, T. McCartin, P. Justus, J. Greeves, J. Bradbury, M. Nataraja, B. Jagannath, W. Patrick, B. Sagar, R. Fedors, J. Prikryl, S. Domine (SwRI)
Letter only: CNWRA Directors, CNWRA Element Mgrs., P. Maldonado

Washington Office • Twinbrook Metro Plaza #210
12300 Twinbrook Parkway • Rockville, Maryland 20852-1606

LABORATORY AND NUMERICAL MODELING OF THE COLD-TRAP PROCESS

Prepared for

U.S. Nuclear Regulatory Commission
Contract NRC–02–02–012

Prepared by

R. Fedors
D. Walter
F. Dodge
S. Green
J. Prikryl
S. Svedeman

Center for Nuclear Waste Regulatory Analyses
San Antonio, Texas

May 2003

ABSTRACT

Natural convection in drifts and its effect on moisture redistribution has not been sufficiently studied to assess the effect of the cold-trap process on performance of the proposed repository at Yucca Mountain, Nevada. This report documents the results from a small laboratory-scale cold-trap model and the tools developed to simulate the laboratory model. The laboratory-scale model may not adequately represent conditions in emplacement drifts, for two reasons. One, it was not practical to include important details of the engineered barrier system in the laboratory-scale model (1-percent scale of the emplacement drifts). Two, there are significant difficulties in strictly following similitude for thermal scaling. The uncertainty of thermal scaling is extensively discussed and an approach is recommended for using at least two laboratory experiments at different scales combined with numerical models to adequately estimate environmental conditions in emplacement drifts. The laboratory-scale model, however, does provide support to the conclusion that the cold-trap process will likely occur under expected repository conditions and sheds light on the general pattern of condensation that occurs when considering axial airflow in drifts. Based on the results of the laboratory-scale experiment, latent-heat transfer and boundary-layer resistance will be included in models for simulating the large-scale cold-trap laboratory model currently under development by the U.S. Nuclear Regulatory Commission and its contractors.

CONTENTS

CONTENTS (continued)

FIGURES

FIGURES (continued)

TABLES

ACKNOWLEDGMENTS

This report was prepared to document work performed by the Center for Nuclear Waste Regulatory Analyses (CNWRA) for the U.S. Nuclear Regulatory Commission (NRC) under Contract No. NRC–02–02–012. The activities reported here were performed on behalf of the NRC Office of Nuclear Material Safety and Safeguards, Division of Waste Management. The report is an independent product of the CNWRA and does not necessarily reflect the views or regulatory position of the NRC.

The authors wish to thank C. Patton for help in producing Figures 3-5 through 3-10, R. Green for a thorough technical review and useful insights, L. Wilson for the editorial review, L Selvey for the format review, and B. Sagar for the programmatic review. The administrative and format support provided by P. Houston is also greatly appreciated.

QUALITY OF DATA, ANALYSES, AND CODE DEVELOPMENT

DATA: Original CNWRA-generated data contained in this report meet quality assurance requirements described in the CNWRA Quality Assurance Manual. Sources for other data should be consulted to determine the level of quality for those data. The work presented in this report is documented in CNWRA Scientific Notebooks 432, 536, 554, and 576.

ANALYSES AND CODES: The commercial package FLOW–3D® Version 8.1.1 was used to generate results for this report and is controlled under the CNWRA software procedure TOP–018. In addition, MathCad2000 Professional and Microsoft® Excel 97 SR-2 were used to generate results.

References:

Flow Science, Inc. "FLOW–3D User's Manual." Version 8.1.1. Sante Fe, New Mexico: Flow Science, Inc. 2003.

1 INTRODUCTION

The cold-trap process refers to the redistribution of water in pipes or subterranean openings (e.g., drifts) driven by temperature gradients. The proposed emplacement of high-level radioactive waste in drifts at Yucca Mountain, Nevada, will significantly elevate the temperatures of the drift environment. Temperature gradients along drifts will lead to the movement of air and vapor in natural convection cells. In the cold-trap process, water evaporates at hotter locations, is carried in the vapor phase by convective airflow, and condenses at cooler locations. For hot zones, where the wallrock dries out from the thermal pulse, the cold-trap process could move water from cooler moist areas to the hotter dry areas. While not leading directly to condensation, cooler areas that did not dry out, or have already rewet, could supply water vapor to convective cells that gradually elevate the relative humidity of hotter areas. Elevated relative humidity combined with deliquescence may lead to liquid-phase water contacting waste packages in peripheral zones of the repository where wallrock temperature may not exceed the boiling point, or in internal zones of the repository when the thermal pulse is dissipating. The geometry of the components of the engineered barrier system (e.g., waste package and support, drip shield, invert) and interaction with the wallrock adds complexity to the problem of simulating airflow and condensation associated with the cold-trap process.

The cold-trap process is expected to lead to elevated vapor pressures migrating inward along the drifts that potentially could lead to the presence of liquid water and enhanced localized corrosion of some waste packages. For extended periods, benign in-drift conditions will likely occur. Aggressive conditions, however, may exist in portions of the drifts for shorter periods of time dependent on a confluence of the temperature, condensation, and chemistry. The waste package outer layer, Alloy 22, may be susceptible to localized corrosion in the presence of liquids with high halide content. The chemistry of water associated with the cold-trap process will differ markedly from that of ambient percolation and thermally-refluxed water. The chemistry of condensed water also may vary markedly along the drifts or in the micro-environments of the engineered barrier system due to variations in reactivity with the substrates (e.g., rock bolts, drip shield, wallrock) on which condensation occurs. Interaction with dust or evaporative residues will also significantly modify the chemistry of the condensate. The cold-trap process will elevate relative humidity in the vicinity of waste packages earlier than would be estimated using porous media models that define the distribution of percolation and seepage. The elevation of relative humidity, which may lead to the presence of liquid-phase water, may lead to localized corrosion of waste packages when temperatures are above 80 °C [176 °F]. The degree to which the cold-trap process will elevate the relative humidity in drifts, however, cannot be quantitatively assessed with much reliability at this time.

Three-dimensional airflow patterns driven by temperature gradients in the drift will lead to two scales of convection. Large-scale convection from temperature gradients between sections of a drift caused by the edge-effect, differential heat loading, and lithological variations along the drift will create axial convection cells along the drifts. Heat transfer from convection will moderate the large-scale temperature differences along drifts caused by the edge effect, differential heat loading, and lithological variations. However, the extent to which temperature differences along drifts will be moderated has not yet been assessed. The axial airflow from hot areas to cool areas will occur beneath both the drift and drip-shield crowns. Cooler air will return, flowing in the opposite direction, near the invert on both sides of the waste packages. These large-scale convection cells are one source of moisture being supplied to hot areas that is not currently considered by the U.S. Department of Energy (DOE). Based on DOE modeling, waste packages

in hot areas remain dry for an extended period of time because there is no local (wallrock) source of water to elevate the relative humidity. While not leading to condensation, cool return flow in convective cells may provide moisture to elevate the relative humidity in hot areas. Other sources of water to the drift are (i) dripping from preferential flow penetrating the dryout zone, (ii) dripping from ambient percolation along fractures, and (iii) evaporation from fracture and matrix water once the wallrock has rewet. As the thermal pulse dissipates, the redistribution of moisture along the drifts caused by the cold-trap process will increase the rate of wallrock rewetting in areas where the dryout front has not disappeared. The cold-trap process will also accelerate the rewetting of the invert, thus possibly negating the drift-shadow barrier proposed by DOE (Bechtel SAIC Company, LLC, 2001a).

Small-scale convection between and around waste packages will be effective at removing heat from the waste packages. Early during the thermal pulse, thermal radiation may exceed convection in hotter areas of the repository as the dominant heat-transfer mechanism. In cooler areas of the repository, or in hotter areas when the thermal pulse is dissipating, convection may be the dominant heat-transfer mechanism. It is at these two situations that the cold-trap process may play its most prominent role in repository performance. Cross-sectional flow patterns driven by the heat load from eccentrically located waste packages in the drifts may be strong enough to impede the large-scale axial-flow patterns. The cross-sectional flow patterns will also lead to a nonuniform distribution of temperature around the engineered barrier system. Temperatures on the outside of the waste package are not expected to be uniform because of the combined influence of conduction (waste package supports), convection, and thermal radiation. Specific locations where the relative humidity will be elevated near the waste packages, thus increasing the likelihood of condensation, will be controlled by convection in the micro-environments of the engineered barrier system.

The specifics of natural convection in emplacement drifts and its effect on moisture redistribution have not been sufficiently studied to assess the effect of the cold-trap process on the performance of the repository. Computational fluid dynamics codes are needed to simulate in-drift airflow patterns, and experimental data are needed to support the numerical models developed using these codes.

This report documents the results of a small laboratory-scale cold-trap experiment and the tools developed to simulate the laboratory model. The focus is on demonstrating that axial convection in drifts will occur at the expected temperature gradients, and furthermore, that convective airflow will lead to condensation. The remainder of Section 1 discusses the background, technical agreements, and risk insight of the cold-trap process. Section 2 presents the analytical and numerical tools used to design and simulate the laboratory cold-trap experiment. In addition, the difficulties in strictly applying similitude to thermal scaling are discussed. Section 3 presents the design, measured data, and simulation results of the small laboratory-scale cold-trap experiment.

1.1 Background

Understanding convection in drifts is the first step in understanding the cold-trap process. Several publications address natural convection between two nested, infinitely long cylinders oriented either eccentrically or concentrically. A thorough treatment of two-dimensional flow for the case of concentrically nested cylinders is reported by Kuehn and Goldstein (1976) and extended to the case of an eccentrically positioned inner cylinder in a subsequent publication, Kuehn and Goldstein (1978). These authors focused on the estimation of heat-transfer

coefficients, but also included descriptions of expected flow patterns. Outside the Yucca Mountain Program, nothing was found in the technical literature that specifically addressed the issue of natural convection in long drifts with an axial temperature gradient and a consideration of associated water vapor transport processes.

DOE is studying natural convection in drifts, but only to support parameter estimation of effective thermal conductivity for the in-drift cells of their thermohydrologic porous media models (CRWMS M&O, 2001). Thermohydrologic modeling is used to estimate in-drift temperature and relative humidity for the DOE performance assessment. DOE uses results from computational fluid dynamics models to estimate effective thermal conductivity values for in-drift cells that account for the heat-transfer processes of conduction and convection (Francis, et al. 2003a,b). A separate estimate of the effect of thermal radiation is included in the thermohydrologic models. The use of effective thermal conductivity to incorporate the effects of in-drift convection into porous media models does not capture the nonuniform conditions created by convection. Results of a natural convection test at the Atlas Facility in North Las Vegas are expected tol be used to support the development of effective thermal conductivity values for in-drift grid cells in drift-scale thermohydrologic porous media models. Computational fluid dynamics simulations of the laboratory natural convection test will advance knowledge about the convective flow patterns around the engineered barriers in the drift, which are important in understanding how the cold-trap process will affect in-drift environmental conditions, particularly near the waste package. The natural convection tests at the Atlas Facility, however, do not include moisture effects because they were run at low vapor pressure conditions.

Within the Yucca Mountain Program, various documents have referred to the possibility of the cold-trap process occurring in the emplacement drifts (Wilder, 1996; CRWMS M&O, 2000a,b), but no investigations addressing the cold-trap process have been documented. Recent work by DOE using computational fluid dynamics simulations (Francis, et al., 2003a) contemplated the addition of evaporation, transport, and condensation to their models, though the focus of their work was on estimating effective thermal conductivity for in-drift cells for the porous media models.

A field test at Yucca Mountain brought the cold-trap process back into consideration. The presence of liquid water in the Passive Test of the Enhanced Characterization of the Repository Block drift supported the likelihood of the cold-trap process occurring in the emplacement drifts, but the results of the Passive Test have not yet been documented. The original test objectives focused on the ambient distribution of percolation and seepage along the tunnel, rewetting of the dryout zone in the wallrock, and recovery of the relative humidity back to nearly 100 percent. Small temperature gradients inadvertently imposed by the monthly startup of the tunnel boring machine at the west end of the Passive Test were thought to cause condensation to occur at various locations along the closed-in drift, thus making the source of the water that dripped and formed pools in the closed tunnel uncertain. The distribution of liquid water axially along the tunnel could be attributed to seepage, condensation from a cold-trap process, or a combination of both (Bechtel SAIC Company, LLC, 2001b). Measurements are being made in the closed-in section in hopes of discovering the source of water that accumulated along the tunnel. The utility of the Passive Test for collecting data on the cold-trap process has been reduced because the heat source from the tunnel boring machine was eliminated before many of the measurement devices were installed.

Besides the difficulties in capturing conductive, convective, radiative, and latent-heat transfer, difficulties in modeling the cold-trap process arise from the disparate scales needed for adequate description of the process. Mountain-scale models are needed to capture the temperature gradients along drifts. Drift-scale models are needed to capture the local environments around the waste package and drip shield. Approximations for conduction, convection, and thermal radiation are needed for the porous media models generally used to estimate temperature and relative humidity at the waste package.

Large-scale temperature gradients along drifts may drive axial convection cells that move water in the vapor phase to locations where condensation could occur. The edge effect, differential heat loading between sections of a drift, and lithological variations along the drift would all act to create repository-scale temperature gradients. The edge effect is the phenomenon where cooler temperatures are experienced at the ends of drifts relative to the centers because of the influence of the cooler rock beyond the edge of the repository. The specific heat load imposed on a drift is subject to emplacement strategies and different thermal history profiles for various waste types. A strategy to lessen the edge effect is to place hot waste packages at the ends of drifts and cool waste packages in the center. However, no strategy will eliminate temperature gradients. Lithological changes affect thermal properties along the drift (e.g., the lower lithophysal unit of the Topopah Spring Tuff has larger saturated thermal conductivity than the middle nonlithophysal unit and hence would conduct heat away from the drifts at a faster rate). An approach for defining temperature gradients along drifts, and the portions of drifts affected by those gradients, was described in Manepally and Fedors (2003). Complementing that approach, the work in this report focuses on the effect of natural convection on in-drift environmental conditions.

1.2 Technical Agreements

Two U.S. Nuclear Regulatory Commission (NRC) and DOE technical agreements were generated on the topic of the cold-trap process.

Agreement TEF.2.04: "Provide the Multi-Scale Thermohydrologic Model AMR, Rev. 01. The DOE will provide the Multi-Scale Thermohydrologic Model AMR (ANL–EBS–MD–00049) Rev 01 to the NRC. Expected availability is FY 02."

Agreement TEF.2.05: "Represent the cold-trap effect in the appropriate models or provide the technical basis for exclusion of it in the various scale models (mountain, drift, etc.) considering effects on TEF and other abstraction/models (chemistry). See page 11 of the Open Item (OI) 2 presentation. The DOE will represent the "cold-trap" effect in the Multi-Scale Thermohydrologic Model AMR (ANL–EBS–MD–00049) Rev 01, expected to be available in FY 02. This report will provide technical support for inclusion or exclusion of the cold-trap effect in the various scale models. The analysis will consider thermal effects on flow and the in-drift geochemical environment abstraction."

The presentation on resolution of the cold-trap process at the Thermal Effects on Flow technical exchange and management meeting[1] noted that DOE would consider the cold-trap effect and would incorporate important effects in the thermohydrological model for performance assessment. The DOE discussed possible approaches for modifying the drift-scale and mountain-scale models. To support these modifications, DOE intended to use a "computational fluid dynamics approach" for independently assessing heat and mass transfer in the emplacement drifts.

1.3 Risk-Informed Aspects

The uncertainty of moisture movement in drifts associated with the cold-trap process is part of the more general concern of how water enters the drifts and how the water pathway dictates the chemistry of liquids contacting the engineered barriers. The chemistry of water contacting waste packages when waste package temperatures are still above 80 °C [176 °F] is important for corrosion. Both uniform and localized corrosion of the titanium drip shield are being extensively studied. Since the cold-trap process offers a moisture pathway that bypasses the drip shield, only waste package corrosion is discussed below. Also, drift degradation will have a prominent effect on environmental conditions in the drifts. The impact of drift degradation is part of ongoing work that will be reported elsewhere. Comments on drift degradation are included here because such degradation likely would dampen natural convection in the drifts.

1.3.1 Waste Package Corrosion

From a risk-informed perspective, it is important to quantify factors that affect the duration of the localized window for corrosion of Alloy 22 and the processes by which water contacts the waste containers. Localized corrosion for Alloy 22 is most likely to occur between approximately 80 and 120 °C [176 and 248 °F], though liquid water may also occur at higher temperatures. Within this temperature window, Alloy 22 may be susceptible to localized corrosion in the presence of solutions with high halide (e.g., chloride) content[2] (Brossia, et al., 2001). Below the temperature window for localized corrosion, the process of generalized corrosion associated with an increase in the water flux contacting the drip shield and waste package will continue to occur. During the performance period, generalized corrosion is not expected to be important, but the uncertainty of localized corrosion plays a prominent role in the uncertainty of dose (Mohanty, et al., 2002).

The period encompassing the temperature window has been predicted to span several hundred to several thousand years depending on thermohydrological model inputs and assumptions (CRWMS M&O, 2001; Manepally and Fedors, 2003). During the window of localized corrosion, the physical process by which water comes in contact with the waste container must be understood well enough to support estimation of the chemistry of the liquid phase contacting the

---

[1]Reamer, C.W. "U.S. Nuclear Regulatory Commission/U.S. Department of Energy Technical Exchange and Management Meeting on Thermal Effects on Flow (January 8–9, 2001)." Letter (January) to S.J. Brocoum, DOE. Washington, DC: NRC. 2001.

[2]Dunn, D.S., O. Pensado, C.S. Brossia, G.A. Cragnolino, N. Sridhar, and T. Ahn. "Modeling Corrosion of Alloy 22 as a High-Level Radioactive Waste Container Material." International Workshop on the Prediction of Long-Term Corrosion Behavior in Nuclear Waste Systems, Caderache, France, November 26–29, 2001. D. Feron, ed. London, United Kingdom: The Institute of Materials. In press.

waste container. Hydrological processes by which water enters and redistributes in drifts, possibly coming in contact with the waste packages, include seepage and dripping, uniform condensation, cold-trap movement of moisture within a drift, and film and rivulet movement of liquid phase water on the engineered barrier. Assuming the integrity of the drip shield is maintained, natural convection associated with the cold-trap process could elevate the relative humidity near waste packages. One possible mechanism to elevate the relative humidity beneath the drip shield is evaporation from the invert. Redistribution of water in the invert and evaporation beneath the waste package will lead to an elevation of vapor pressure. A dry invert may be rewetted by drainage condensation on the drift wall and drip shield on the invert. Deliquescence enables liquid phase water to form on waste package surfaces at relative humidity values well below the saturated vapor pressure. Because it is an important input to corrosion models, the uncertainty in timing and magnitude of relative humidity in the vicinity of waste packages, with and without considering the effect of the cold-trap process, requires further analysis.

Different modes of water movement lead to markedly different chemical conditions. Evaporated and initially condensated water is relatively dilute and will likely have a low pH. Interaction of the condensed water with the surface material on which it condenses, including any dust or residual mineralization left by previously evaporated water, will prominently alter the chemistry of the liquid phase water. Refluxed water that flows across a residue in fractures of the wallrock likely will be highly concentrated, and possibly highly corrosive. Inadequate knowledge of the relative portions of ambient seepage, refluxed, and condensed water entering the drifts would lead to uncertainty about the chemistry of solutions contacting the waste container.

1.3.2 Transport

Current DOE models predict that a dryout zone in the invert and below the drift will serve as a significant natural barrier to radionuclide transport. Dripping, along-wall seepage, and condensation from the cold-trap process will accelerate rewetting of the invert in cooler location. Increased wetness of the invert and the wallrock below the drift may serve to increase radionuclide transport rates if breaching of waste packages occurs in certain locations of the emplacement drift.

1.3.3 Effect of Drift Degradation

Current estimates of drift degradation based on thermal-mechanical modeling suggest that all of the repository drifts will likely be backfilled within 1,000 years after closure because of drift degradation processes (Gute, et al., 2003). Most of the drifts are estimated to be backfilled to some degree after 500 years. Both emplaced and natural backfill will lead to higher estimated temperatures in the drifts, though there may some important differences between the two backfills. One difference is that the thermohydrologic properties of natural backfill will be different from that of the aggregate suggested for use as a backfill emplaced at the time of repository closure. A second difference is that the timing and degree of natural backfilling will control the magnitude of increased temperatures estimated for the waste packages.

The thermal-mechanical response to the heat load imparted by the emplaced radioactive waste will lead to a natural backfill of coarse to fine blocks of varying shapes, dependent on characteristics of the wallrock lithology, that will likely be poorly packed. Estimates of bulking factor can be used to estimate the important thermohydrological properties of the natural backfill.

Thermal-mechanical results also provide thickness of the rubble pile and drift degradation height, both as a function of time, which can be used to estimate airspace above the rubble pile backfill.

Convective heat and moisture movement along the length in a backfilled drift will likely be reduced over that of the open drift that only has a drip shield. If the drip shield remains intact, convective heat transfer and moisture movement could occur both beneath the drip shield and in the air pocket above the rubble pile. Also, convection through the rubble pile will likely occur and is expected to be greater than natural convection through the intact fractured wallrock. Currently, the DOE does not take credit for any natural convection through the fractured tuff surrounding the drift, though there may be an element of convective heat transfer included in the *in situ* measurements of thermal conductivity. Drift degradation may also increase the heterogeneity of thermal properties of the material surrounding waste packages, possibly leading to localized temperature gradients capable of causing increased convective air and moisture transfer along the drift between waste packages or zones of waste packages. The magnitude of possible convection in the drift degradation scenario described above has not been assessed.

2 MODELS FOR IN-DRIFT AIRFLOW AND MOISTURE MOVEMENT

The occurrence and modeling of the cold-trap process in drifts is not well understood. The need to understand the combined effect of fundamental processes involved in the movement of moisture driven by convection necessitated the development of laboratory, analytical, and numerical models. Individually, the heat-transfer processes of conduction, convection, radiation, and latent heat are reasonably well understood. However, the combined effects of all heat-transfer processes in geometrically complex environments are poorly understood and difficult to model. The approach taken for this work was to simplify the analytical and numerical models by incrementally adding processes as evidence was found to justify their inclusion, particularly the less easily incorporated processes.

Temperature and moisture levels in the drift environment play an important role in waste package integrity. Large-scale temperature gradients along drifts may drive axial convection cells that move water in the vapor phase to locations where condensation could occur. Moisture movement from wet areas to areas previously dried out by the thermal pulse may elevate the relative humidity sooner than if no convection is considered. Also, local convection cells affected by the design of the engineered barrier system may also create zones of preferential condensation. These local zones around the complex geometry of the engineered barrier system are not addressed in this report, but will be in future work.

To gain insights on the cold-trap process, a laboratory experiment was performed using a porous ceramic cylinder surrounded by variably saturated sand to represent a drift located in fractured rock. A temperature gradient inside the drift was induced by placing a heater cartridge at one end of the cylinder and a heat sink at the other end. The variably saturated sand was intended as an external supply of water for inside the cylinder.

To help design the laboratory model, an analytical solution for airflow in a differentially heated drift was developed. A simple model of condensation was combined with the solution for airflow directions and magnitudes to estimate expected condensation rates. The analytical solution is described in Section 2.1. To incorporate needed details in the modeling of the cold-trap experiment, a computational fluid dynamics model was created. Sections 2.2 and 2.3 describe the computational fluid dynamics model used to numerically model the cold-trap experiment. A scale-model analysis is presented in Section 2.4 to illustrate the uncertainty in scaling laboratory experiments to full-scale repository conditions. The scale modeling is also used to demonstrate how a numerical model can be verified by laboratory-scale experiments and then applied with improved confidence to full-scale conditions.

2.1 Analytical Model

An analytical solution of airflow and heat transfer was developed as a tool to aid in designing and interpreting the cold-trap experiment. Heat transfer by conduction and convection were included in the model; thermal radiation and latent-heat transfer were not. In the analytical solution, the actual cylinder was represented as a two-dimensional vertically-oriented slice along the drift length. The analytical model also replaced the heater cartridge with an endwall held at a uniform temperature. The top and bottom walls were insulated and heat was removed at the opposite endwall, which was held at a uniformly colder temperature than the hot endwall. The overall geometry of the model problem is shown in Figure 2-1. A summary of the development of the analytical solution is included in this section; a detailed derivation is included in Appendix A. The

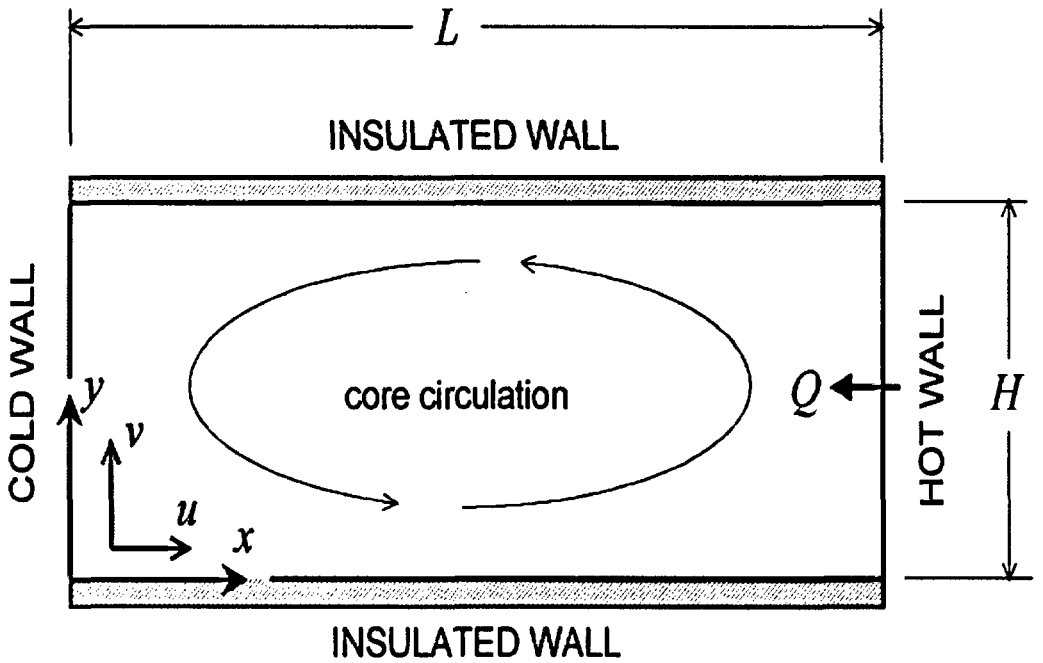

Figure 2-1. Two-Dimensional Simplification of Laboratory Experiment

objective of the analysis was to predict the magnitudes of the overall circulation in the drift and the rate at which moisture might be condensed at the cold portion of the drift.

For the analytical solution, steady flow was assumed. The Boussinesq assumption was used to approximate buoyancy effects. The Boussinesq approximation neglects the effect of fluid (air) density dependence on pressure of the air phase, but includes the density dependence on temperature. The equations of motion were made nondimensional using the following scheme.

$$X = x / L \quad \text{and} \quad Y = y / H \qquad \text{nondimensional coordinates}$$

$$U = u\left(\nu_o L\right)\left(g\beta_o H^3 \Delta T_o\right)^{-1} \qquad \text{nondimensional velocity in } x \text{ - direction}$$

$$V = v\left(\nu_o L^2\right)\left(g\beta_o H^4 \Delta T_o\right)^{-1} \qquad \text{nondimensional velocity in } y \text{ - direction} \qquad (2\text{-}1)$$

$$\theta = \left(T - T_c\right)/\Delta T_o \qquad \text{nondimensional temperature}$$

where

ΔT_O — temperature difference between hot and cold wall
T — air temperature at location x,y
T_C — temperature of the cold wall (x = 0)
g — gravitational acceleration
β_o — thermal expansion coefficient of air at the reference temperature
ν_o — kinematic viscosity of air at the reference temperature

The nondimensional variables for coordinates and temperature have a maximum value of one and a minimum value of zero.

Circulatory flow within the two-dimensional drift is governed by the following differential equations written in nondimensional form, which express the conservation of mass, momentum, and energy requirements.

$$\frac{\partial U}{\partial X}+\frac{\partial V}{\partial Y}=0 \tag{2-2}$$

$$\left(\frac{H}{L}\right)^4\left(\frac{Ra}{Pr}\right)\left[\frac{\partial}{\partial X}\left(U\frac{\partial U}{\partial X}+V\frac{\partial U}{\partial Y}\right)\right]-\left(\frac{H}{L}\right)^2\left(\frac{Ra}{Pr}\right)\left[\frac{\partial}{\partial Y}\left(U\frac{\partial V}{\partial X}+V\frac{\partial V}{\partial Y}\right)\right]=$$
$$\frac{\partial\theta}{\partial X}-\frac{\partial^3 U}{\partial Y^3}+\left(\frac{H}{L}\right)^2\left[\frac{\partial}{\partial Y}\left(U\frac{\partial^2 V}{\partial XY}+V\frac{\partial^2 U}{\partial X^2}\right)\right]+\left(\frac{H}{L}\right)^4\frac{\partial^3 V}{\partial X^3} \tag{2-3}$$

$$Ra\left(\frac{H}{L}\right)^2\left(U\frac{\partial\theta}{\partial X}+V\frac{\partial\theta}{\partial Y}\right)=\left(\frac{H}{L}\right)^2\frac{\partial^2\theta}{\partial X^2}+\frac{\partial^2\theta}{\partial Y^2} \tag{2-4}$$

where

Pr	—	Prandtl number (ν_o/α_o)
Ra	—	Rayleigh number [$g\beta_o H^3\Delta T_o/(\alpha_o\nu_o)$]
α_o	—	thermal diffusivity ($k_o/\rho_o C_{po}$) of air at reference temperature
k_o	—	thermal conductivity of air at reference temperature
ρ_o	—	density of air at reference temperature
C_{po}	—	specific heat of air at reference temperature

The boundary conditions for these differential equations were no slip for velocity at all walls, no heat flux at top and bottom ($Y = 0$ and $Y = 1$), $\theta = 0$ at the cold end ($X = 0$), and $\theta = 1$ at the hot end ($X = 1$).

The general approach used to solve Eqs. (2-2) through (2-4) for nondimensional temperature and velocity was to find a solution expressed in powers of $(H/L)^2$, noting that $(H/L)^2 << 1$. Expanded solutions in orders of $(H/L)^2$ for U, V, and θ were substituted into the differential equations for mass, momentum, and energy conservation, and terms were collected in powers of the parameter $(H/L)^2$.

Solutions were developed for the core area (area between the hot and cold ends of the drift) and the endwall areas. For the core area, the symmetry condition of $\theta = 0.5$ for $X = 0.5$, $Y = 0.5$ requires that

$$K_2+\frac{1}{2}K_1+Ra\left(\frac{H}{L}\right)^2\frac{K_1}{1440}=\frac{1}{2} \tag{2-5}$$

where the unknown constants K_1 and K_2 need to be determined for each specific problem.

Based on the solution for the core area, U would not be identically zero at $X = 0$ and $X = 1$ as the boundary conditions require. The average value of U across the drift height would be zero, however, so the $X = 0$ and $X = 1$ boundary conditions would be satisfied in an average sense. Similarly, the temperature θ would not be constant in a vertical profile near the hot end or the cold end. Thus, different solutions for the endwalls are needed.

The solution for the core region was expanded to the endwall region by considering the end effects separately using a boundary layer approach. The boundary layer approach was used because it converges quickly and an integral formulation can be used. From symmetry, the boundary layer would be the same on the cold wall and the hot wall. Thus, symmetry was imposed about the center of the drift and only the cold wall was considered. In addition, boundary conditions at the cold wall require that all velocities were zero and that the temperature was constant and equal to the cold-wall temperature. There were also conditions required to match the boundary layer to the core flow at the edge of the boundary layer and to make the boundary layer flow merge smoothly with the core flow. For an integral solution, physically reasonable functions were assumed for the velocities and temperature, which were then made to satisfy the governing equations in an integral sense. The equations for conservation of momentum and energy were put into an integral form by integrating them across the boundary layer thickness. By substituting the functional expressions developed for the endwall zone into the integral expressions of Eqs. (2-3) and (2-4) and performing the integrations, the following two equations that relate the unknown parameters were derived.

$$\frac{2}{5}\left(\frac{H}{L}K_1\right)\left[\frac{1}{4}-(\delta')^4\right]=\left[k_2+\frac{Ra}{1440}\left(\frac{H}{L}K_1\right)^2\right](\delta')^3 \tag{2-6}$$

$$\frac{Ra^2}{725760}\left(\frac{H}{L}K_1\right)^3\delta'=k_2+\frac{Ra}{1440}\left(\frac{H}{L}K_1\right)^2 \tag{2-7}$$

where

$\delta' = \delta\,(L/H)$ — scaled boundary layer thickness

These two expressions and Eq. (2-5) were sufficient to determine the three unknowns: K_1, K_2, and δ'.

In addition, the net heat flow from the hot end of the channel to the cold end is a combination of conduction through the air and the energy carried by the flow. Net heat flow was modeled using the following integral.

$$Q=\int_0^H\left(k_o\frac{\partial T}{\partial X}-\rho_o C_{po}uT\right)dy \tag{2-8}$$

Note that the integral does not depend on position X in the drift. Integration gives

$$Q = k_o \Delta T_o \left(\frac{H}{L}\right)\left[K_1 + \frac{K_1^3}{362880}\left(\frac{H}{L}Ra\right)^2\right] \quad (2\text{-}9)$$

Using Eqs. 2-5, 2-6, 2-7, and 2-9, either ΔT_o or Q can be specified in solving for the unknown constants K_1, K_2, and δ'.

To check on the reasonableness of the analytical solution, a comparison of vertical temperature and axial velocity between the results from the two-dimensional analytical solution and a three-dimensional computational fluid dynamics simulation was made using the same heat source and boundary conditions. This check assessed the approximation of using a two-dimensional solution of a rectangular drift to represent a three-dimensional cylindrical drift. The computational fluid dynamics code, FLOW–3D® (Flow Science, Inc., 2003), is described in Section 2.2. The problem design consisted of a 5-cm [1.97-in] diameter and 60-cm [23.6-in] long drift with a temperature of 305 K [89 °F] at the hot end and 295 K [71 °F] at the cold end and insulated top and bottom walls. The vertical profiles of the axial velocity at the midpoint were in close agreement with only a slight dampening of the velocity extremes (Figure 2-2). The vertical temperature profile from the two-dimensional analytical solution exhibited up to a difference of 0.5 K [0.9 °F], as compared to the computational fluid dynamics simulation result (Figure 2-3).

Once the airflow rates were known, the condensation rate could be estimated for the entire drift. Moisture transport was computed using the following observations and assumptions: (i) the flow from the hot end to the cold end carries wetter air to the cold end; (ii) the reverse flow from the cold end to the hot end carries drier air back to the hot end; (iii) the air has a 100-percent relative humidity at the hot end; (iv) when the air gets to the cold end, it will be supersaturated and some moisture will condense on the target (the air will still have a 100-percent relative humidity, but because it is colder, the actual mass of water in the air will be less); (v) the airflow from one end to the other equals the average density of the air times the average velocity in either the upper (hot to cold) or lower (cold to hot) half of the tube; and (vi) the same airflow rate occurs in the circular channel as in the two-dimensional drift.

For the laboratory cold-trap experiment, the assumption of 100-percent relative humidity will lead to overestimates of condensation rate. Since the ceramic cylinder is saturated, relative humidity at the driftwall will be nearly 100 percent. However, relative humidity of the air mass above the heater will be depressed over that of the dirftwall because of the temperature difference between the two locations. If applied to emplacement drifts, the assumption of 100-percent relative humidity would be further in error because the driftwalls may be dry.

The average velocity in the hot or cold half of the drift can be obtained by integrating the core velocity distribution. Once the mass-flow rate of air in the upper or lower half of the drift is known, the amount of moisture condensed can be calculated as the difference in the absolute humidities at the hot and cold ends of the drift multiplied by the flow rate of air. To get a distribution of condensation along the drift, temperature and integrated velocity values can be calculated for specified axial positions. Then the condensation rate for each section of the drift can be estimated. Where temperature and axial velocity values change rapidly, a finer discretization can be used.

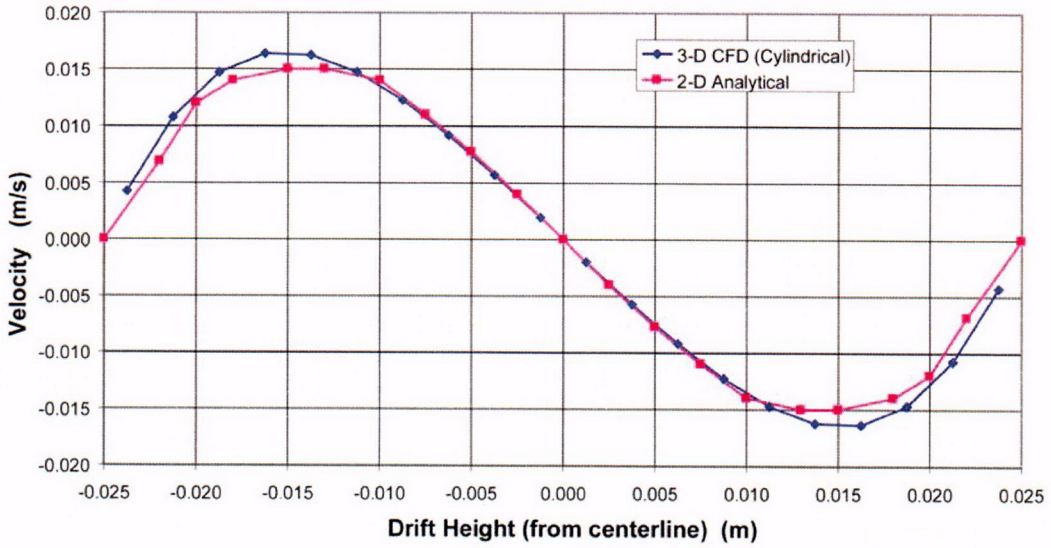

Figure 2-2. Comparison of Axial Velocities in a Vertical Profile Using the Two-Dimensional Analytical Solution and the Three-Dimensional Computational Fluid Dynamics Solution (Shown as CFD in Figure) [0.3048 m = 1 ft; 0.3048 m/s = 1 ft/s]

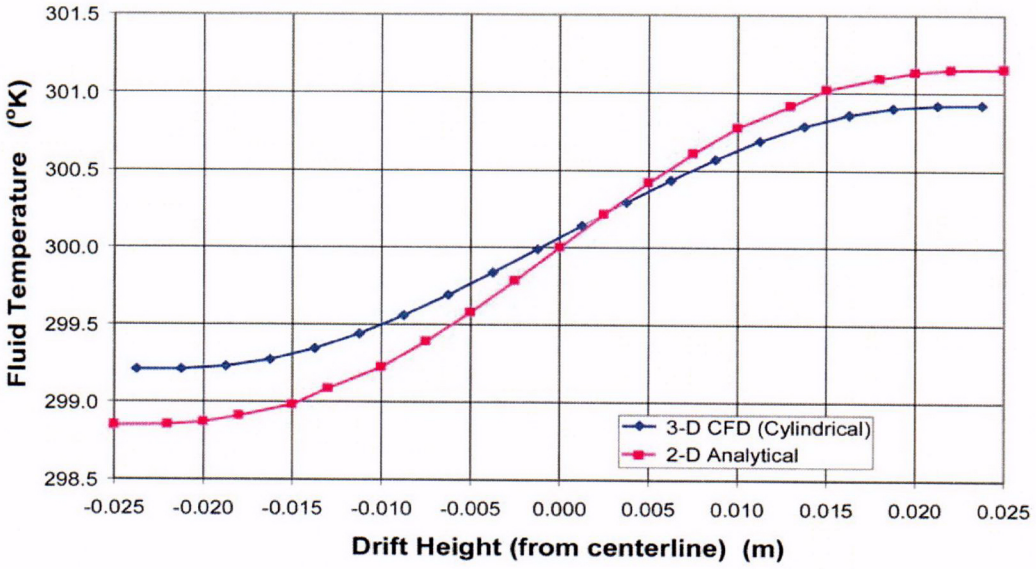

Figure 2-3. Comparison of Axial Temperature Values in a Vertical Profile Using the Two-Dimensional Analytical Solution and the Three-Dimensional Computational Fluid Dynamics Solution (Shown as CFD in Figure) [0.3048 m = 1 ft; °F = 1.8 × T K – 459.67]

C-01

2.2 Numerical Model

To better capture the details of the flow field in the drift and allow the inclusion of complicated geometries, computational fluid dynamics numerical codes can be used. Numerical modeling of the cold-trap laboratory experiment was accomplished with the commercially available finite-volume computational fluid dynamics code FLOW-3D® (Flow Science, Inc., 2003). The primary goal of numerical modeling was to demonstrate that natural convection in the drift can transport moisture from the hot end to the cold end of the drift. General patterns of the resulting detailed flow field can be used to infer the general pattern of condensation along a differentially heated drift. As a secondary goal, modeling was used to refine and verify analytical and numerical modeling techniques for the future development of large-scale laboratory models or for simulating conditions in emplacement drifts.

The three-dimensional computational fluid dynamics model incorporated the major components and geometry of the laboratory-scale cold-trap experiment setup. Appendix B includes detailed schematic drawings of the computational fluid dynamics model geometry, solid material properties, boundary conditions, and other modeling parameters. The drawings are shown in the coordinate system used for computational fluid dynamics modeling and throughout this report for the experimental and numerical results. Note that Figures B–1 and B–2 use a different coordinate system than that used for the analytical model.

Three features of the numerical model are worth noting. One, to reduce the computational fluid dynamics simulation time, only half the cold-trap geometry was modeled by imposing a symmetry condition in the x-z plane (vertical plane down the center of the drift axis). Two, the Boussinesq approximation was used to simulate natural convection in the drift. That is, the air was assumed to be nominally incompressible in which the density varies with temperature but does not vary with pressure. Three, laminar airflow was used in the numerical model as supported by estimates of the Rayleigh Number for the small-scale laboratory experiment. For large-scale experiments, or simulation of emplacement drifts, turbulent airflow may occur.

Conduction, convection, thermal radiation, and latent-heat transfer may all be prominent in the emplacement drifts. Only conduction and convection were incorporated into the computational fluid dynamics model. Thermal radiation is expected to decrease in significance as the thermal pulse dissipates (i.e., both the absolute temperature and the temperature difference across air spaces will decrease). In the small-scale laboratory model, a conservative (high) estimate of the radiative heat transfer was 5 percent of the power input.

For simplicity, latent-heat transfer was assumed negligible until evidence arose to suggest otherwise. To simulate latent-heat transfer using commercially-available computational fluid dynamics codes, algorithm development and incorporation into the software would be required. Incorporating evaporation and transport would be straightforward. The process of condensation, however, is more difficult. The technical problem of successfully incorporating condensation into a computational fluid dynamics code is that when moist air cools by convection or conduction to below the dewpoint temperature, the water vapor condenses to keep the gas mixture in equilibrium. Unlike evaporation, in which the liquid evaporates from a known location, the dewpoint temperature may occur anywhere in the air mass, not just at a solid/air interface. Difficulties in matching measured data, as presented in Section 3, indicate that latent-heat transfer may not be negligible.

Since FLOW-3D® (Flow Science, Inc., 2003) does not have the capabilities to readily model the evaporation and condensation processes present in the experiment or full-scale drift, an alternative approach was developed. To evaluate these key processes, the computational fluid dynamics model was used to determine flow and temperature distributions in the drift, assuming that the gas in the drift was composed of dry air. The moisture transport was then estimated from the results of the computational fluid dynamics simulations as described in the next section.

2.3 Water Transport and Condensation Estimates Using Numerical Model Results

A simple model was used to estimate the condensation rate when using the analytical solution for heat transfer and airflow described in Section 2.1. That approach relied only on knowledge of the temperature at both ends of the drift, the airflow rate in the upper portion of the drift, and the mass of water in air near the hot end when the relative humidity was at 100 percent. A more sophisticated approach was implemented when computational fluid dynamics modeling was used.

The computational fluid dynamics analysis used here does not directly compute the transport of water vapor in the drift. Rather, the computational fluid dynamics analysis predicts the heat and mass transport of air alone due to buoyancy effects. The dry-air computational fluid dynamics estimates are then used to estimate the transport of water vapor using the method described here. The assumptions underlying this approach include

- The computational fluid dynamics velocity and thermal predictions for dry air are representative of those for moist air
- The air in the drift is saturated at the local air temperature
- The vapor diffusion velocity is much greater than the advection velocity
- The thermal effect of evaporation is negligible compared to the dry-air heat transfer rates
- Water vapor and air both act as ideal gases

Consider the control volume inside the drift as shown in Figure 2-4. The net mass flow of water vapor into the control volume, m_v, is mathematically represented by

$$m_v = \int_{A_x} c_v \rho u dA \qquad (2\text{-}10)$$

where

c_v — mass concentration of water vapor
ρ — local density

The integration is carried out over the face of the control volume at the axial location x.

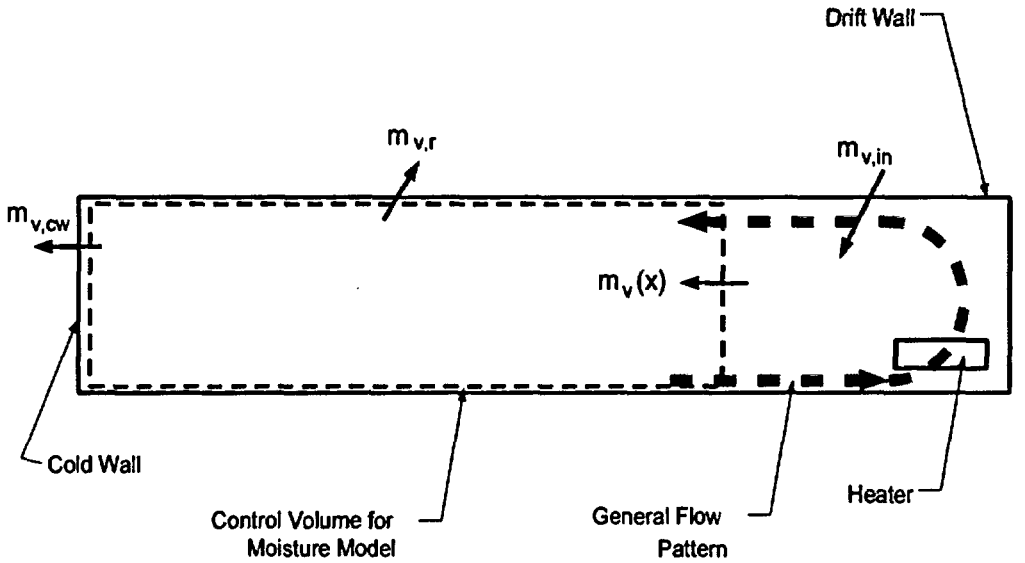

Figure 2-4. Control Volume for Moisture Transport Analysis Using the Cold-Trap Experiment Computational Fluid Dynamics Simulation

Following the ideal gas assumption, the mass concentration of water vapor can be expressed as

$$c_v = \left[\left(\frac{P_{v,sat}}{P} \right) \frac{M_a}{M_v} + 1 \right]^{-1} \tag{2-11}$$

where

M_a = 28.96 g/mol and
M_v = 18.02 g/mol — molecular weights of air and water vapor
P — total pressure
$P_{v,sat}$ — saturation pressure of water vapor at the local temperature.

The saturation pressure of water vapor was approximated by the Keenan, Keyes, Hill, and Moore formula (American Society of Heating Refrigeration and Air Conditioning Engineers, Inc., 1977),

$$\ln\left(\frac{P_{v,sat}}{217.99} \right) = \frac{0.01}{T}(374.136 - t)\left[-741.9242 + \sum_{i=1}^{7} F_i (0.65 - 0.01\,t)^i \right] \tag{2-12}$$

where

F_1 = −29.72100 F_2 = −11.55286 F_3 = −0.8685635

F_4 = +0.1094098 F_5 = +0.439993 F_6 = +0.2520658

F_7 = +0.05218684

and

T — temperature expressed in K
t — temperature expressed in °C
$P_{v,sat}$ — saturated vapor pressure expressed in atmospheres

Because the computational fluid dynamics analysis uses finite volumes and areas for the discrete analysis, the integral in Eq. (2-10) is approximated as

$$m_v(x_i) = \sum_{k=1}^{N_k} \sum_{j=1}^{N_j} c_v\left(T_{i,j,k}\right) \rho\left(T_{i,j,k}\right) u_{i,j,k} f_{x,i,j,k} \Delta A_{x,i,j,k} \quad (2\text{-}13)$$

where

f_x — fraction of the computational cell face in the axial direction that is open to flow
ΔA_x — computational cell face area
N_j — number of cells in the transverse (y) direction
N_k — number of cells in the vertical (z) direction

Because the computational cells are aligned in a cartesian coordinate system, some of the elemental volumes include both the drift wall and air space. The parameter f_x describes the flow blockage effect that enables a cartesian coordinate-based grid to simulate irregular boundaries, such as a cylindrical heater cartridge or drift. As indicated, the summations were carried out over all the cells in a particular axial plane at $x = x_i$.

Equation (2-13) was used as an expression of the net mass flow of vapor into the control volume. Part of this mass flow was condensed and returned to the drift inner wall ($m_{v,r}$ in Figure 2-4) and the remainder was condensed at the cold wall ($m_{v,cw}$ in Figure 2-4). The amount of water vapor condensed at the cold wall was estimated by computing m_v at each axial station along the drift and extrapolating the resulting curve to the x-position at the cold wall.

2.4 Scaling Issues

Subscale laboratory models can be an efficient way to help in understanding the cold-trap process and its effect on environmental conditions in heated drifts. Experiments can be used to investigate natural convection heat transfer, temperature distributions, and airflow in several reduced-scale models of a representative drift at Yucca Mountain under post-closure (nonventilated) conditions. However, uncertainties in the direct scaling of results from small-scale models to the large-scale conditions in drifts at Yucca Mountain warrant careful attention. This section describes (i) a conceptual approach for using subscale models to estimate actual scale conditions, (ii) the uncertainty in scaling results from subscale models to large-scale conditions, and (iii) the approximate scaling approach to use for design of subscale experiments.

2.4.1 Generic Scaling Approach

A general approach for addressing the uncertainty involved with using small-scale models to estimate conditions in the drifts at Yucca Mountain would be to calibrate a numerical model to the results from a laboratory model at one scale (e.g., 25-percent scale), predict the results for another model at a different scale (e.g., 50-percent scale), and then confirm the numerical results with measurements made on the larger scale model. Successful estimation of conditions in the second scaled model lends confidence to the scaling approach. This overall approach is depicted in Figure 2-5. The shape of the dashed line in Figure 2-5 is not known. Confidence in estimating conditions for the emplacement drifts is increased by using large-scale, rather than small-scale, laboratory models. It is hoped that the changes in processes are small between the largest-scaled laboratory models and the emplacement drifts. The remainder of this section describes the underlying bases for the uncertainty in the scaling process, thereby providing the basis for caution when using subscale models to estimate conditions in actual geometries and heat load conditions.

2.4.2 Uncertainty in Scaling Heated Drifts

The design of an experiment that uses subscale models to investigate behavior in a full-scale prototype should be based on the requirements of similitude. These requirements state that all important dimensionless parameters must be the same for the model and the prototype. Analytically, the similitude requirements are comparable to formulating the problem as a set of differential equations, initial conditions, and boundary conditions in dimensionless form so as to make the analytical solution independent of the geometric dimensions and fluid physical properties of the problem. For a natural convection problem, similitude requires that not only must the geometric configuration be preserved between the model and the prototype but also the dimensionless parameters that govern the flow and the heat transfer must be preserved. These additional parameters include the Grashof number, *Gr*, and the Prandtl number, *Pr*, defined as

$$Gr = \frac{g\beta\Lambda^3}{\gamma^2}\Delta T_{ref} \quad \text{and} \quad Pr = \frac{\rho\gamma C_p}{k} \tag{2-14}$$

where

β — thermal expansion coefficient of the fluid (e.g., air)
Λ — characteristic length (e.g., drift diameter)
γ — kinematic viscosity of the fluid
C_p — specific heat of the fluid

k — thermal conductivity of the fluid
ΔT_{ref} — a reference temperature difference (e.g., temperature difference between a heater surface, T_s, and a wall boundary, T_w)

As an alternative to the Grashof number, some investigators use the Rayleigh number. The Rayleigh number is the product of the Grashof number and the Prandtl number.

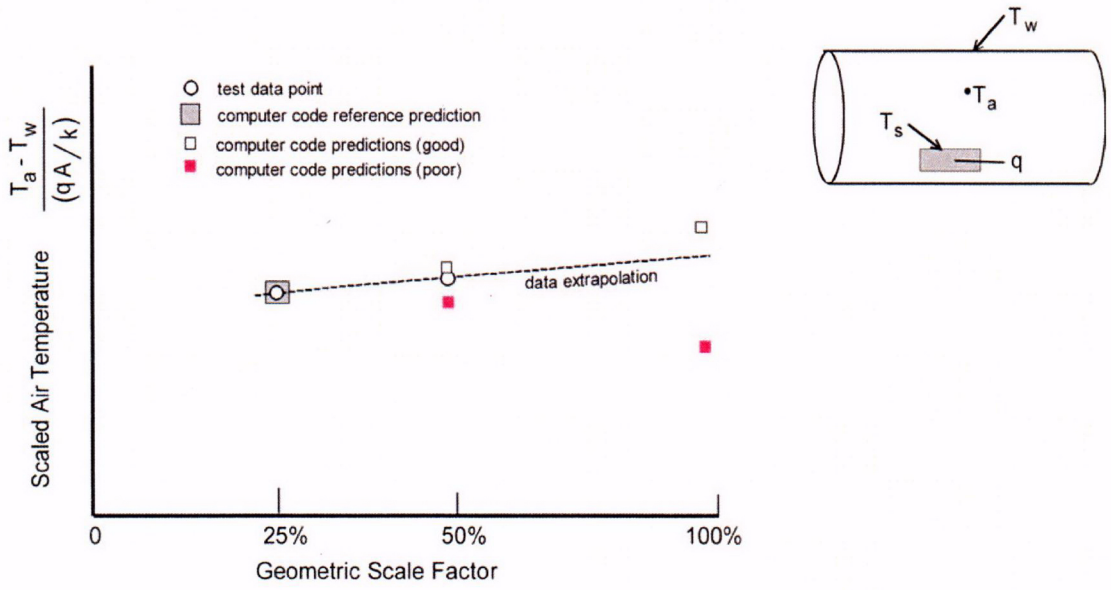

Figure 2-5. Conceptual Approach for Using Subscale Models to Estimate Conditions at Full Scale. T Is the Temperature; q Is the Heat Generated by the Heater; A Is the Area of Heater; and k Is the Thermal Conductivity.

The requirements for scale-model tests are determined by equating the model values of the Grashof and Prandtl number to the full-scale values. This equality will, for example, determine the required value of ΔT_{ref} for the model in terms of the value of ΔT_{ref} of the prototype, the geometric scale factor λ (ratio of the characteristic dimension of the model to the full-scale characteristic dimension), and the model and full-scale fluid properties. A similar procedure would determine the required heat addition rate of the model heaters.

This kind of similitude is impractical to use because the ΔT_{ref} for a reduced geometric scale model would have to be equal to the full scale ΔT_{ref} divided by λ^3. This gives a value, for example, for the heater wall temperature T_s that is considerably too large to be practical. Another option would be to use a fluid for the model tests that has a much smaller value for kinematic viscosity than air to lower the value of T_s, but this is also not likely to be reasonable.

Alternatively, tests could be scaled on the heat flux or heat transfer. To illustrate that this approach is also problematic, scaling based on the heat-transfer coefficient is developed below. The form of the heat-transfer coefficient for *unconfined* natural convection can be derived form well-established experiments in the literature (e.g., Raithby and Hollands, 1975; Incropera and DeWitt, 2002; and Kreith and Bohn, 2001) as

$$h = \frac{k}{\Lambda} B\,(Gr)^n (Pr)^m \qquad (2\text{-}15)$$

where

B — a numerical coefficient (dimensionless)

n, m — exponents (dimensionless)

C-02

For many unconfined natural convection situations in which the flow is turbulent, the exponent n is approximately one third. When this is the case, the characteristic length Λ of the problem cancels out of the right side of Eq. (2-15) to give a heat-transfer coefficient that is independent of the characteristic length

$$h = Bk(Pr)^m \left(\frac{g\beta}{\gamma^2}\right)^{1/3} (\Delta T_{ref})^{1/3} \qquad (2\text{-}16)$$

This relation can be used to show that the rate of heat generation by the heater should be reduced in proportion to the reduction in heater surface area, or in effect by λ^2 for subscale tests. This conclusion follows from the fact that the heat generation rate is numerically equal to the heat transfer rate $q = hA(T_s - T_a)$ from the heater to the air, where T_a is the average or bulk temperature of the fluid far from the heater. It is also noted that h from Eq. (2-16) is equal to the full-scale heat-transfer coefficient and that the surface area A of the heater is reduced in proportion to λ^2. It should be noted that these relations apply strictly to unconfined natural convection where T_a is independent of either the surface temperature of the heater or the heating rate. In practice, T_a could be taken to be the drift-wall temperature T_w, which would be assumed held at a known constant value (i.e., known ambient rock temperature). This scaling method, however, is overdefined since more parameters are assumed to be fixed (h, T_s, and T_w) than is possible to hold constant.

Since the model tests cannot be conducted strictly in accordance with the requirements of similitude, the tests would lead to distorted results, and the conclusions based on the conditions expressed in Eqs. (2-15) and (2-16), would not apply to the emplacement (full-scale) drifts in a straight-forward manner. For example, flow fields in the model tests and in a full-scale prototype would not yield identical values of the scaled (dimensionless) air velocities because the Grashof number would be too small in the model tests by a factor equal to the geometric scale factor cubed. This flow-field distortion could significantly influence temperature distributions and heat-transfer rates.

To estimate the magnitude of heat-transfer distortions, an analogous problem was investigated by the analytical model described in Section 2.1, assuming the height of the full-scale drift was 5 m [16 ft] and the length was 40 m [130 ft]. The temperature difference ΔT between the hot wall and the cold wall was assumed to be 30 °C [54 °F]. The Rayleigh number for this situation is 2.786×10^{11}. The heat flux q from the hot wall to the cold wall was calculated to be 13.53 W/m^2 [4.289 BTU/h-ft^2]. Thus, the heat-transfer coefficient, h, had a value of 0.451 W/m^2 - °C [0.0794 BTU/h-ft^2 - °C].

For the example using the 25-percent scale model, the scaled drift height was 1.375 m [4.51 ft] and the length was reduced in proportion. If the model had the same ΔT = 30 °C [54 °F] as the prototype, the Rayleigh number was 4.353×10^9. The heat flux from the hot wall to the cold wall was computed to be 23.53 W/m^2 [7.459 BTU/h-ft^2]. Hence, the heat-transfer coefficient was 0.784 W/m^2 - °C [0.138 BTU/h-ft^2 - °C], which is 74 percent larger than the full-scale value. If, instead, the heat flux was maintained at the full-scale value of 13.53 W/m^2 [4.29 BTU/h-ft^2], the required value of ΔT would be 19 °C [34 °F], and the heat-transfer coefficient would be 0.711 W/m^2 - °C [0.125 BTU/h-ft^2 - °C], which is 57 percent larger than the full-scale value. The Rayleigh number for this case was 1.857×10^{10}. To make the heat-transfer coefficient equal to

its full-scale value of 0.451 W/m^2 - °C [0.0794 BTU/h-ft^2 - °C], ΔT has to be reduced to about 2 °C [3.6 °F], and the heat flux would then be only 0.9 W/m^2 [0.29 BTU/h-ft^2] instead of the full scale value of 13.53 W/m^2 [4.29 BTU/h-ft^2]. It is apparent that the full-scale values of heat flux, temperature difference, and heat-transfer coefficient cannot all be maintained at the full-scale values if it is not possible to follow strict similitude laws.

These results from the analytical model for a confined natural convection problem indicate that the heat-transfer coefficient increases, instead of remaining constant, with a decrease in the geometric-scale factor. This relationship is in agreement with published literature [e.g., Kuehn and Goldstein (1978)]. The value of the heat-transfer coefficients inferred from laboratory tests may be too small, perhaps by a considerable percentage, if identical values of the heat flux are maintained for subscale and full-scale models. Laboratory and field subscale test results, however, still could be used to validate computer simulations as described in the next section. For this purpose the temperature measurements from two different geometric scales would be extremely valuable.

2.4.3 Thermal Scaling Methods for a Large-Scale Cold-Trap Experiment

The generic scaling approach previously described to address uncertainty in thermal scaling indicates that subscale models at two scales could be used in conjunction with numerical modeling to lend confidence to estimates for full-scale conditions. Results from a desktop-scale (1-percent scale) laboratory model are described in Section 3. A larger laboratory (or field) subscale model has not yet been completed. The thermal scaling approach will be important for the proposed laboratory model currently being designed at approximately 25-percent scale.

The proposed large-scale cold-trap experiment should have a geometric scale factor (ratio of model-drift dimensions to corresponding full-scale dimensions) in the range of one-fourth of full-scale. The proposed experiment will be considerably larger than the desktop scale cold-trap experiment. To design the large-scale experiment, it is necessary to know how to scale the heater power of the simulated waste packages. To make this determination, it is assumed that the scale-model tests are conducted in such a way that the temperature differences ΔT between various locations in the scale-model drift are equal to the full-scale values. It is also assumed that

- Simulated waste packages, waste package supports, and the invert are geometrically scaled (i.e., the same shape, but smaller) with respect to actual waste packages. When added to the large-scale laboratory model, the drip shield will also be geometrically scaled.

- Far-field temperatures (i.e., outer walls) of the scale-model drift are maintained equal to far-field temperatures of the actual drifts.

- Relative humidity of the air in the scale-model drift, either at the cold end or fro the entire drift, is maintained at 100 percent by a water source within the drift.

The third assumption is not actually required for thermal scaling, but is needed to demonstrate the desired cold-trap phenomenon (transport and condensation of moisture). In the following discussion, the geometric scale factor is denoted by λ (e.g., one-fourth).

The heat added to the drift air by waste packages is eventually transmitted to the surrounding rock (except for the small fraction needed to vaporize any liquid water within the drift). Excluding latent-heat transfer, the energy balance between the heat q generated by a waste package and the heat transferred to the air is expressed as

$$q = hA_s\Delta T \tag{2-17}$$

where

ΔT — temperature difference between the outer surface of the waste package and the inner surface of the drift

As mentioned previously, it is desired to conduct the scale-model tests such that the ΔT values measured in the subscale model tests can be interpreted as full-scale temperature differences and the heat-transfer coefficients can also be scaled up. The scale-model surface areas are λ^2 times the full-scale areas. If the scale factor for the heat-transfer coefficient is denoted as λ_h and the scale factor for the scale model heater powers is denoted by λ_q, then from Eq. (2-17)

$$\lambda_q = \lambda_h\lambda^2 \tag{2-18}$$

Thermal scaling of the waste packages thus reduces to the question of how the heat-transfer coefficient h is scaled. The two-dimensional analysis of the cold-trap model problem using the analytical solution presented in Section 2.1 indicates that the heat-transfer coefficient increased as the geometric scale factor decreases. The experiments and analyses of Kuehn and Goldstein (1976) for a similar geometry demonstrates that the heat-transfer coefficient increases as the scale factor decreases according to the following relation

$$\lambda_h = \lambda^{-n} = \lambda^{-0.25} \tag{2-19}$$

If Eq. (2-19) holds for the cold-trap model geometry, the heater power of the geometrically similar heater has to be reduced in proportion to

$$\lambda_q = \lambda^{1.75} \tag{2-20}$$

That is, the heater power is reduced less than is the heater-surface area for a subscale model.

Because of the uncertainty in the exact value of n in Eq. (2-19) for the cold-trap experiment, the experiment needs to be numerically simulated in advance. The simulations could be conducted for several values of the geometric scale factor λ, in which the exponent n be varied until a value of n is obtained that results in the equal values of ΔT at similar scaled locations for various heater power settings.

It is noted that scaling the heater power by the method described herein will not necessarily result in air velocities in the drift that can be easily interpreted in terms of full-scale values. Numerical simulations combined with measurements from large-scale experiments will shed light

on the velocity scaling. Air velocity primarily determines the overall rate at which moisture is transported and condensed within the drift. The lack of a definite velocity scaling does not limit the validity of the experiments to demonstrate the cold-trap phenomenon nor will it compromise the ability to scale up the heat-transfer results and the heat-transfer coefficients to full scale as discussed in the next section.

2.4.4 Scaling To Repository Conditions

The fluid mechanics and heat-transfer phenomena occurring in the drift depend on many interrelated parameters, but the primary dimensionless parameters that govern the drift response are the geometrical shapes of the drift and the waste packages and the Rayleigh Number, which governs the natural convection flows set up by the heat released by the waste packages. Since Ra is a function of Λ^3, it is not possible to have exactly the same value of Ra for a reduced-scale model of the drift as for the repository (unless ΔT is increased substantially or a fluid rather than air is used to fill the model drift).

Consequently, model tests must be conducted at different geometric scales or with different ΔT values, or empirical relations must be found in the literature. Otherwise, empirical relations must be developed in combination with numerical simulations and measurements to scale up the model experiments to repository conditions. Even with these restrictions, scale-model tests can be conducted in such a way that the heat-transfer coefficients that apply between waste packages and drift fluid can be determined from the tests and scaled to repository conditions

$$h_{\text{repository}} = h_{\text{model}} \left(\frac{\Lambda_{\text{model}}}{\Lambda_{\text{repository}}} \right) \left(\frac{Ra_{\text{repository}}}{Ra_{\text{model}}} \right)^{n} \qquad (2\text{-}21)$$

where $n \approx 0.25$. To accomplish this scaling, the heat output of the simulated waste packages has to be adjusted appropriately, as previously discussed. Similarly, the airflow velocities and moisture transport can be interpreted (but not scaled up directly) to predict repository conditions.

To lessen uncertainty in velocity scaling, large-scale experiments are needed to support numerical models. The small-scale experiment described in Section 3 was 1-percent scale of the emplacement drifts. The processes acting in the small-scale laboratory experiment and in the emplacement drift are generally expected to be the same, though the relative magnitudes of each component's effect may change. The prominent process not expected in the small-scale laboratory model that will be present in the large-scale experiments or the emplacement drift is turbulent flow. Turbulent flow can readily be incorporated into the numerical models used to estimate airflow rates, however, the choice of an appropriate turbulence model should be based on measured data or relevant studies in the literature. Two-equation turbulence models are generally applicable to drifts, but different turbulence models may be appropriate for different portions or aspects of airflow in the drift. To lessen the effect caused by not strictly following similitude, measured data from larger-scale laboratory or field experiments should be incorporated into the numerical models. A 25-percent scale model is in development. Furthermore, data from the U.S. Department of Energy 44-percent scale natural convection test can be used to develop confidence in the numerical models.

2.5 Summary

This chapter summarized a two-dimensional analytical solution for a differentially heated drift, the computational fluid dynamics numerical code to solve geometrically-complex problems, and the uncertainties involved with using results from subscale laboratory models to estimate conditions at field scale (emplacement drifts). Heat-transfer processes of conduction and convection were incorporated into the models. Thermal radiation and latent-heat transfer were assumed negligible, though experimental results presented in the next section cast doubt on the validity of the latter assumption.

Geometry, dimensionality, and boundary conditions were simplified to develop the analytical solution. Results from the numerical model can be used to support the more efficient and easy-to-use analytical solution. The use of a computational fluid dynamics numerical model does not rely on the simplifications used for the analytical solution, but still may not capture all the important processes expected in the emplacement drifts. Since similitude cannot be strictly applied to thermal scaling, a combination of subscale experiments and numerical modeling is needed to better estimate heat transfer and moisture movement along the drifts at Yucca Mountain. The next section presents the measurements and modeling results from a single, small-scale laboratory cold-trap model, referred to as the desktop model. A second subscale model, larger than the desktop model, is being developed and will be described in future reports.

3 COLD-TRAP LABORATORY EXPERIMENT

A laboratory-scale experiment was designed, assembled, and conducted to investigate vapor driven air movement and condensate formation induced by the cold-trap effect in a simulated emplacement drift. Three test phases of a small-scale laboratory, cold-trap experiment are discussed in this section, including the associated analytical and numerical modeling.

Interpretations of temperature profiles from the laboratory model shed light on the important heat-transfer processes, airflow rates induced by temperature gradients, and inferred condensation rates from moist masses of air moving along the drift. Conductive, convective, thermal radiative, and latent-heat transfer may all occur in the emplacement drifts of Yucca Mountain. Conduction is important in the solid portions of the engineered barriers and in the wallrock. Convection of air above and below the drip shield will lead to cross-sectional and axial airflow patterns that will enhance heat transfer away from waste packages. The U.S. Department of Energy (DOE) currently incorporates the effects of conductive and convective heat transfer in their total system performance assessment models through the use of an effective thermal conductivity in porous media models. The convective heat transfer, however, is only incorporated in a cross-sectional sense—no axial heat transfer is incorporated.

Latent-heat transfer from evaporation at hot locations and condensation at cool locations further enhances heat transfer away from hotter wallrock and invert locations to cooler locations, either locally or along the drifts. For simplicity, latent-heat transfer is assumed negligible for this laboratory experiment and modeling—an assumption that may require further analysis based on results of the numerical modeling presented in Section 3.4. Heat transfer by thermal radiation drops off quickly as a function of absolute temperature and temperature differences across air spaces. Either or both of these conditions may prevail in the emplacement drifts at times when the effect of the cold-trap is important for corrosion. Because of the low absolute temperatures in the desktop laboratory cold-trap experiment, heat transfer by radiation is assumed negligible. The wallrock will also influence temperature distribution in the drift. When viewed as a boundary condition for the drift, the heat flux perpendicular to the wall is a function of the distance from the heat source.

Airflow rates and directions are directly influenced by temperature gradients, thus making temperature a useful and practical surrogate measurement in laboratory experiments to compensate for the difficulties in measuring airflow rates directly. Condensation rates can be inferred from airflow rates if the diffusion rate of water through the air is assumed fast enough to offset convective movement rates, particularly for diffusion through the boundary layer between the air and solid materials where condensation occurs. Differences between measured and simulated condensation rates presented in Section 3.4 suggest that the boundary layer resistance may require further analysis.

Qualitative conclusions from the desktop laboratory cold-trap model will be useful to guide the research direction for estimating the effect of cold-trap processes on local environmental conditions in the drift. Quantitative inferences on large-scale behavior are not given because of the large scale difference between the laboratory and drift-scale settings and because the small laboratory model does not include the elements of the engineered barrier (e.g., drip shield, invert) that would affect airflow and heat transfer. The laboratory experiment is referred to as the desktop model to distinguish it from the larger-scale laboratory model under development. The desktop experiment is a 1-percent scale model of the proposed emplacement drifts at Yucca

Mountain, whereas the larger-scale laboratory experiment will be about 25-percent scale. As discussed in Section 2.3, results from the desktop model scaled to conditions in the repository drifts would lead to large uncertainties. The specific goals of the desktop laboratory experiment were to demonstrate that the cold-trap process occurs and to simulate the process as it occurs in the laboratory model.

3.1 Description of Cold-Trap Laboratory Model

3.1.1 Design

A schematic drawing of the desktop experimental assembly is shown in Figure 3-1. The simulated drift consisted of a 61-cm [24-in] long porous ceramic cylinder horizontally emplaced in a 25 cm × 30.5 cm × 61 cm [10 in × 12 in × 24 in] test cell. The porous cylinder had a 5.0-cm [2.0-in] inner diameter, a 6.35-cm [2.5-in] outer diameter, and was constructed of Kellundite®, a ceramically bonded alumina made by Filtros Ceramic Products of East Rochester, New York. Material properties of the cylinder included a maximum pore diameter of 100 μm [0.004 in], 30–40 percent porosity, and permeability of 2.58×10^{-9} m^2 to 4.14×10^{-9} m^2 [2.8×10^{-8} ft^2 to 4.5×10^{-8} ft^2].

The test cell was constructed of lexan, which was selected for its heat resistance (better than plexiglass) and insulating properties. The test cell was assembled by connecting and sealing precut pieces of lexan using 3.8-cm [1.5-in] long, 0.63-cm [0.25-in] diameter threaded steel bolts and silicone sealant. The porous ceramic cylinder was approximately centered in the test cell {e.g., the midpoint of the cylinder was 12.25 cm [4.8 in] from the floor and 15.25 cm [6.0 in] from the side boundaries of the test cell}. The ends of the cylinder abutted the lexan plastic forming the endwalls of the test cell, which allowed viewing of the cylinder interior during assembly and testing.

The test cell was filled to a height of about 24.5 cm [9.6 in] with a fine-grained quartz sand (OK #1) from T&S Materials Incorporated of Gainesville, Texas. Water was added to the sand to act as a supply of water to the ceramic cylinder and thus to the air in the drift. Deionized water was added to the test cell until the sand at the base of the ceramic cylinder was 100-percent saturated. Because the thermal properties of the sand had a marked effect on temperatures in the drift, the material and thermal properties of sand are described in more detail in Section 3.1.2.

A temperature gradient was established inside the drift by placing a 7.62-cm [3.0-in] long, 0.95-cm [0.375-in] diameter Chromalux® electric cartridge heater made by OMEGA Engineering Incorporated of Stamford, Connecticut, at one end of the simulated drift and placing a heat-sink assembly at the opposite end of the drift (Figure 3-1). Power to the cartridge heater was supplied by a Staco variable autotransformer made by Staco Energy Products Company of Dayton, Ohio. The power output of the heater element in watts at a given setting was determined from measurements of the voltage and current supplied to the heater element at various transformer settings. The heat-sink assembly consisted of copper tubing {0.63-cm [0.25-in] outer diameter} mounted in a 30.5-cm × 30.5-cm × 3.8-cm [12.0-in × 12.0-in × 1.5-in] lexan enclosure that was filled with water. Cooling of the water in the assembly was accomplished by passing the ends of the copper tubing through the top of the lexan

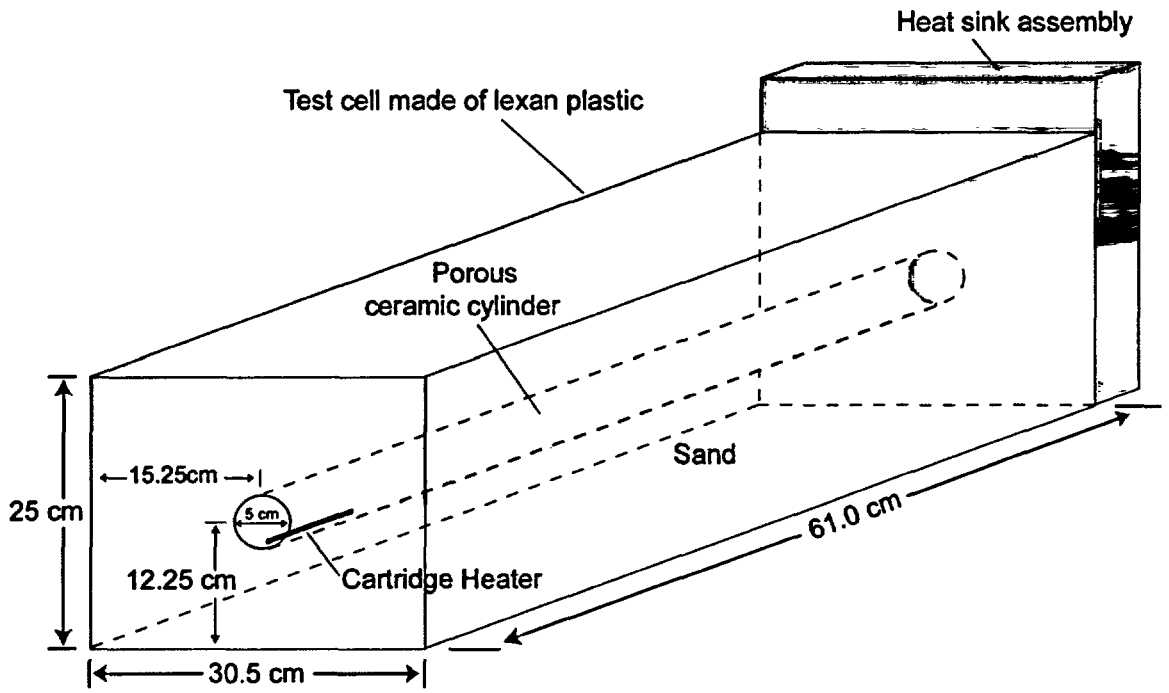

Figure 3-1. Experimental Assembly [2.54 cm = 1 in]

enclosure and connection via plastic tubing to a Coolflow Model CFT–33 refrigerated recirculator made by Neslab Instruments Incorporated of Newington, New Hampshire.

3.1.2 Sand Properties

Variably saturated sand surrounding the ceramic cylinder was used to supply water to keep the ceramic cylinder from drying out during a test. A fine sand was chosen so that the saturation level in the sand would remain high in the area surrounding the cylinder when the sand was completely saturated immediately below the cylinder. The variably saturated sand ensured that the ceramic cylinder remained fully saturated, a consequence of capillarity and the manufactured small pore sizes in the ceramic. The saturated water level in the sand needed to remain below the cylinder to avoid positive pressure heads forcing water into the cylinder. While the water retention characteristics of the sand were important for the supply of water to the drift air, the variably saturated sand made identification of the sand thermal properties more difficult. Informal estimates of the saturation immediately above the ceramic cylinder made using a time-domain reflectrometry probe during the early test phases indicated that the ceramic remained saturated

Water-retention characteristics of the sand were measured using an informal profile-sampling laboratory approach. Water-retention characteristics were also estimated using the physical properties of the sand and a pedotransfer function. The measurements suggested that liquid saturation in the sand surrounding the horizontally placed ceramic cylinder {i.e., 5.0 cm [2.0 in]} would be >90 percent due to capillary rise. These measurements were obtained by sampling a 20-cm [7.8-in] tall column of wetted sand. Measurements using a time-domain reflectrometry probe qualitatively supported the >90 percent saturation level at the top of the cylinder. The

material properties of the sand included an uncompacted bulk density of 1.6 g/cm^3 [100 lbs/ft^3], a measured porosity of 35 percent, and a base permeability of 4.5×10^{-11} m^2 [4.8×10^{-8} ft^2]. Based on grain-size distribution data obtained from the supplier, T & S Materials, Inc., 9 percent of the sand was very fine sand and 87 percent was fine sand using the U.S. Department of Agriculture classification scheme; 93 percent of the particles were between 0.075 and 0.3 mm [0.003 and 0.012 in]. Using these numbers for particle-size distribution and bulk density, two different pedotransfer functions were used to estimate van Genuchten parameters for the sand, and subsequently, saturations at specified heights above the ceramic cylinder. Based on the estimates using the pedotransfer functions in Rosetta Version 1.2 developed by U.S. Department of Agriculture, the saturation of the sand would be >99 percent at the top of the ceramic cylinder, >97 percent at 5 cm [2.0 in] above the ceramic cylinder, and >90 percent at 10.5 cm [4.0 in] above the ceramic cylinder. It should be noted that pedotransfer functions rely on the statistics from large data sets, thus, they may lead to errors when applied to specific porous media. All estimates assume the zero-water pressure (water-table) plane is at the bottom of the ceramic cylinder. Since there are large uncertainties in these estimates, laboratory measurements of the water retention curve for the sand have been initiated using an outflow cell and will be reported at a later date.

The importance of the thermal conductivity of the sand to modeling the cold-trap process is addressed in Section 3.4. Difficulties in matching the temperature profiles in the sand and the apparent underestimate of heat transfer through the sand led to the hypothesis that thermal convection might be occurring in the partially saturated sand. Estimates for dry sand thermal conductivity from standard heat transfer and soil science textbooks (Incropera and DeWitt, 2002; Kreith and Bohn, 2001; Jury, et al., 1991) range from 0.14 to 0.582 W/m - K [1.9 to 8.1 BTU/h-ft - °F] and for wet sand from 1.1 to 2.7 W/m - K [15 to 37 BTU/h-ft - °F]. A similar range was presented by Somerton (1992), who noted that dry thermal conductivity was a function of porosity. Using one-dimensional heat-transfer estimates across the lexan and insulation from measured temperature data, estimates of effective thermal conductivity were estimated to be in the range of 0.12 through 1.2 W/m - K [1.7 to 17.0 BTU/h-ft - °F]. Dimensionality (one-dimensional approach for a three-dimensional problem), uneven insulation, position along the length of the drift, and possible convection in partially saturated sand may all have contributed to the wide range of estimated effective thermal conductivity values.

To help support published values and calibrated estimates of effective thermal conductivity, measurements of thermal conductivity were made by D. Blackwell of Southern Methodist University on small cylindrical samples of dry (air-saturated) and wet sand. The method used was a modification of the divided-bar approach described in Sass, et al. (1971). Values of 2.13 and 2.26 W/m - °C [29.5 and 31.3 BTU/h-ft - °F] were measured for the saturated thermal conductivity and 0.33 and 0.34 W/m - °C [4.6 and 4.7 BTU/h-ft - °F] were measured for the dry thermal conductivity.

The measured values of dry and wet thermal conductivity, while considered reliable, do not account for the partially saturated sand above the cylinder in the desktop experiment. The sand in the desktop experiment varied from saturated below the ceramic cylinder to partially saturated at the top of the box. Except for immediately above the cylinder, the degree of desaturation of sand is uncertain. Estimates of effective thermal conductivity for a range of saturations provided a bounding range for calibration in the computational fluid dynamics model. An expression commonly used for thermal conductivity as a function of saturation is

$$k_{eff} = k_{dry} + \sqrt{S_l}\left(k_{sat} - k_{dry}\right) \quad (3\text{-}1)$$

(Somerton, et al., 1974) where k_{eff} is the effective thermal conductivity for a partially saturated sand, k_{dry} is the dry thermal conductivity, k_{sat} is the saturated thermal conductivity, and S_l is the saturation level. Using a saturation of 90 percent, the effective thermal conductivity would be 2.10 W/m - °C [29.1 BTU/h-ft - °F]; using a value of 50-percent saturation, the effective thermal conductivity would be 1.65 W/m - °C [22.9 BTU/h-ft - °F]. The homogeneous value determined from manual calibration of the computational fluid dynamics simulations described in Section 3.4 was 1.76 W/m - °C [24.4 BTU/h-ft - °F], which falls in the range bounded by Eq. (3-1).

3.1.3 Instrumentation

Temperatures inside the drift were monitored using OMEGA® precision thin-wire thermocouples made by OMEGA Engineering Incorporated of Stamford, Connecticut. The thermocouples were placed in vertical cross-sectional arrays at various locations along the length of the drift. This arrangement allowed evaluation and mapping of both vertical and horizontal temperature distribution within the drift. Schematics of the locations of thermocouple arrays along the length of the drift and the positions of thermocouples in two sample arrays are shown in Figure 3-2. At the heated end of the drift, thermocouples were also vertically placed in the sand media above and below the drift at 1.27-cm [0.5-in] intervals. Locations of these thermocouples are also shown in Figure 3-2. Besides supporting estimates of effective thermal conductivity for the sand, monitoring of temperatures in the sand media allowed evaluation of potential dry out and air movement in the sand due to heating. Thermocouples were attached to a Hewlett Packard 34970A data acquisition/switch unit controlled by Hewlett Packard DataLogger Version 1.1 software, which allowed real-time monitoring and automated capture of temperature data.

Initial tests were conducted to evaluate air movement in the drift. Relative humidity in the air space of the drift was measured in the initial tests using Vaisala Model HMP–235 temperature/humidity probes made by Vaisala, Incorporated of Woburn, Massuchusetts. The 20.3-cm [8.0-in] long, 0.5-cm [0.20-in] diameter probes were horizontally placed in the center of the drift about 11.4 cm [4.5 in] from each end (Figure 3-1). The accuracy of the relative humidity probes in the range from 90 through 100 percent was measured at +/- 2 percent. Results of these tests indicated that relative humidity of the drift air varied with temperature. At temperatures ranging from about 23 to 70 °C [75 to 158 °F], measured about 1.25 cm [0.5 in] above the heater cartridge, relative humidity ranged from about 98.5 to 94.0 percent, respectively. On the other hand, due to lower and relatively constant temperatures imposed by the heat-sink assembly {e.g., temperature ranging from about 21.0 to 23.0 °C [70 to 73 °F]}, relative humidity at the cooled end of the drift remained relatively constant at between 99 and 100 percent. The lower relative-humidity values near the heater are consistent with the theoretical depression of humidity in the presence of a thermal gradient in a subterranean cavity with a saturated wallrock. The high saturations at the cool end indicate possible condensation. After the initial tests, the temperature/humidity probes were removed from the test cell to avoid perturbing air movement inside the drift.

To control heat loss and the effects of diurnal temperature variations in the laboratory room on temperature measured in the drift, the entire test-cell assembly was insulated. The test cell rested on a 5.0-cm [2.0-in] thick layer of styrofoam insulation. The heat-sink assembly was encapsulated in a 2.5-cm [1.0-in] thick layer of styrofoam insulation, while the rest of the test

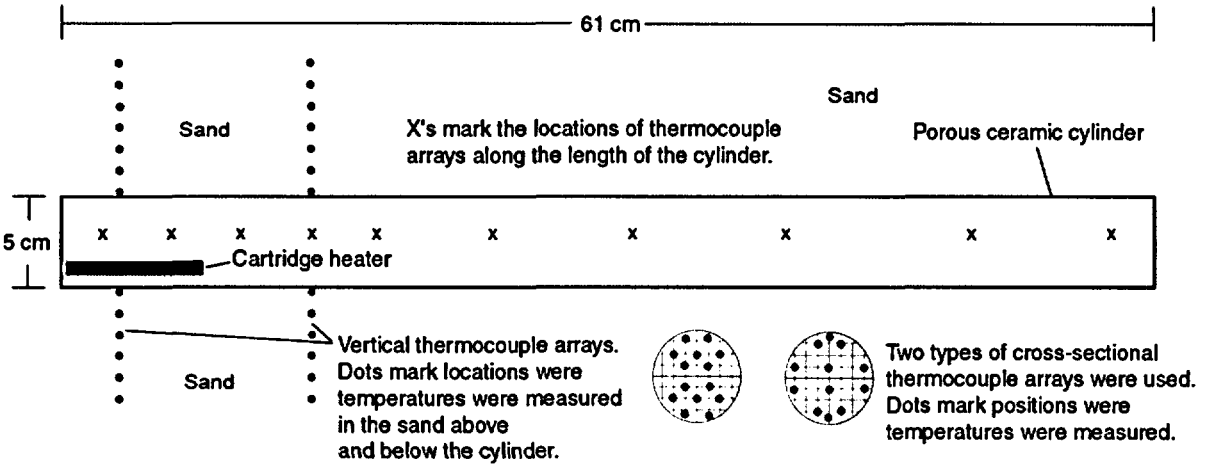

Figure 3-2. Locations of Vertically Positioned Thermocouple Arrays Along the Length of the Simulated Drift for the Test Phases. Sample Thermocouple Arrays and the Location of Thermocouples Placed in the Sand Above and Below the Drift Are Also Shown. [2.54 cm = 1 in]

cell was covered in a 2.5-cm [1.0-in] thick layer of fiberglass insulation. Heat loss and diurnal temperature variations were monitored by placement of Omega® Type T temperature probes (15.2-cm [6.0-in] long, 0.31-cm [0.2-in] diameter sheath) at various locations outside the test cell. Note that these externally-placed thermocouples differed from those used inside the test box. The temperature probes located outside the test box were attached to a Fluke Hydra DataLogger controlled by Fluke Hydra Starter Version 3.0 software for real time monitoring and automated capture of temperature data.

After initial exploratory tests, a condensate collection system was installed in the test cell. The collection system consisted of a 0.5-cm [0.2-in] diameter hole or sump drilled into the base of the drift immediately adjacent to the heat-sink-cooled drift endwall. The sump was constructed so that condensate forming on the cooled face of the lexan plastic at the end of the drift would drip down and collect in the depression. A plastic tube connected to the base of the sump allowed condensate to exit the test cell. Condensate exiting the test cell was collected in a sample container and its mass was determined over time by gravimetric measurements.

3.2 Data and Observations from Test Phases

This section presents the data measured during the three test phases discussed in this report. The data are presented in graphical format. Appendix C contains a listing of the thermocouple locations and steady-state temperature measurements taken for each test. Figures in this section and tables in Appendix C use the coordinate system shown in Figure B–1 where the origin is in the center of the drift. The x-direction is positive toward the hot end and negative toward the cold end of the drift. Early test phases were qualitatively used to assess the model system behavior. The first test phase, Test #11, measured the temperature distribution in

response to three different power input settings. During the second test phase, Test #14, condensation was collected from the heat sink wall at three applied heater power levels. Test #14 included fewer thermocouples than Test #11. Difficulties in matching computational fluid dynamics model results with the measured data led to the hypothesis that convective heat transfer was possibly occurring in the variably saturated sand above the ceramic drift. To help assess this hypothesis, the third test phase, Test #16, was used to assess the thermal conductivity of the sand when there was no water present in the sand or drift. The sand was oven-dried prior to assembly of Test #16.

3.2.1 Calibration Data

The calibration of temperatures estimated from thermocouples and wattage supplied to the heater cartridge is considered important to interpretation of the data. Other measurements followed standard quality assurance standards, but that information does not warrant discussion here.

Thermocouple calibrations were checked after Test #11 and Test #14 to assess the level of temperature measurement accuracy that could be relied on for interpreting thermal results. The thermocouples were placed in a heated bath at different temperatures covering the range expected in the cold-trap test. A calibrated thermometer was used to determine the temperature of the water bath. Calibrations were performed prior to test phases to determine or recheck the regression relations used to estimate temperatures from the electrical signals.

Post-test calibration checks were performed twice to assess the reliability of the measured data. Post-test accuracy checks generally indicate that there was a temperature measurement uncertainty of +/- 0.2 for Test #11 and +/- 0.5 for Test #14 (Table 3-1).

Power input to the drift was estimated based on calibrations of the transformer settings to the wattage supplied. In addition, power supplied to the heater cartridge was periodically checked using a calibrated WAVETEK 27XT and a Fluke 87 to measure voltage and amperage at numerous transformer settings when the transformer was cold and when it was hot. Values of power supplied to the heater cartridge are included in Appendix C for each steady-state data set for each of the three tests.

3.2.2 Measured Temperature Data

This section graphically presents the measured temperature data. Appendix C contains the thermocouple locations and steady-state temperature profiles used for analyses in Section 3.4. Three test phases are presented in this report.

- Test #11 included water in the sand and had 112 thermocouple locations to help indirectly define the flow field.
- Test #14 also included water in the sand, but used fewer thermocouples and had a collection system to continuously collect condensate from the cold endwall of the drift.
- Test #16 focused on heat transfer in the dry sand by obtaining more temperature profiles in the sand, including several thermocouples placed off-center of the drift.

Table 3-1. Statistical Data From Calibration Checks of the Thermocouples. Minimum, Maximum, Average, and Standard Deviation Are From the Thermocouple Estimates of Temperature. [(1.8 × T°C) + 32 = °F]						
Test # 11						
Known Temperature, °C	23.80	30.85	38.00	44.90	51.00	57.90
Minimum Error	-0.24	-0.20	-0.22	-0.18	-0.18	-0.32
Maximum Error	0.16	0.24	0.16	0.16	0.26	0.23
Average Error	-0.08	-0.04	-0.06	-0.06	-0.02	-0.01
Standard Deviation	0.093	0.084	0.073	0.074	0.092	0.116
Test #14						
Known Temperature, °C	23.35	29.75	36.05	43.65	49.95	56.20
Minimum Error	-0.39	-0.28	-0.22	-0.28	-0.45	-0.32
Maximum Error	1.27	0.44	0.33	0.33	0.42	0.50
Average Error	-0.06	0.01	0.01	0.00	-0.10	0.10
Standard Deviation	0.292	0.243	0.172	0.134	0.131	0.129

Test phases were allowed to run until steady-state conditions at each power setting were approached. Profiles of temperature over time for Test #11 and Test #14 are presented in Figures 3-3 and 3-4 for selected cross-sectional arrays of thermocouples. External thermocouple locations include positions between the lexan and the insulation and outside the insulation on top of the experiment box. Water bath temperatures represent heat-sink temperatures. Measurements in the sand include vertical profiles above and below the cylinder at two axial locations.

Generally, the cold-trap system reached steady conditions within a couple of days after changes to power supplied to the heater cartridge. To avoid dryout, overdriving the system to reach steady state more quickly was avoided. Overdriving the system means initially increasing the power setting to a point above the level desired for the test phase, then reducing the power setting to the desired level.

Trends and shifts in external, or ambient, conditions around the laboratory test cell are reflected throughout the model system. Marked diurnal cycles are prominent in the ambient air temperature readings and are dampened progressively by the insulation, lexan, and sand. Prominent differences in temperature within a cross-sectional location illustrate the variance caused by convection in the top and bottom half of the drift, and, to a lesser degree, illustrate the lateral variations in temperature within an array.

Differences between temperatures recorded during Test #11 and Test #14 for similar power settings were noted. Test #11 results were lower by nearly 5 °C (9 °F), though some of the difference may be explained by slightly different thermocouple placement during installation. Power leaking out of the system (e.g., along lead wire to heater cartridge) and a slightly different effective thermal conductivity in the sand and insulation may account for much of the difference. These differences are discussed further in Section 3.4.

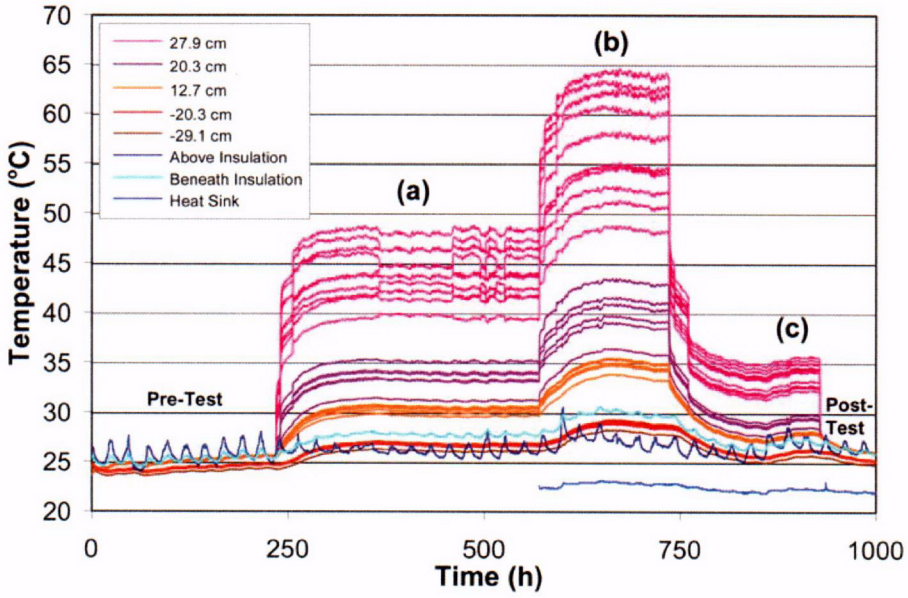

Figure 3-3. Plots of Time Profiles for Test #11 Using Selected Thermocouples in the Drift, Sand, and External Positions. Specified Locations Are the Axial Coordinates of the Drift. The Power Levels Were (a) 3.37 W [11.5 BTU/h], (b) 5.251 W [17.9 BTU/h] and (c) 1.246 W [4.25 BTU/h]. [(1.8 × T °C) + 32 = 1 °F; 2.54 cm = 1 in]

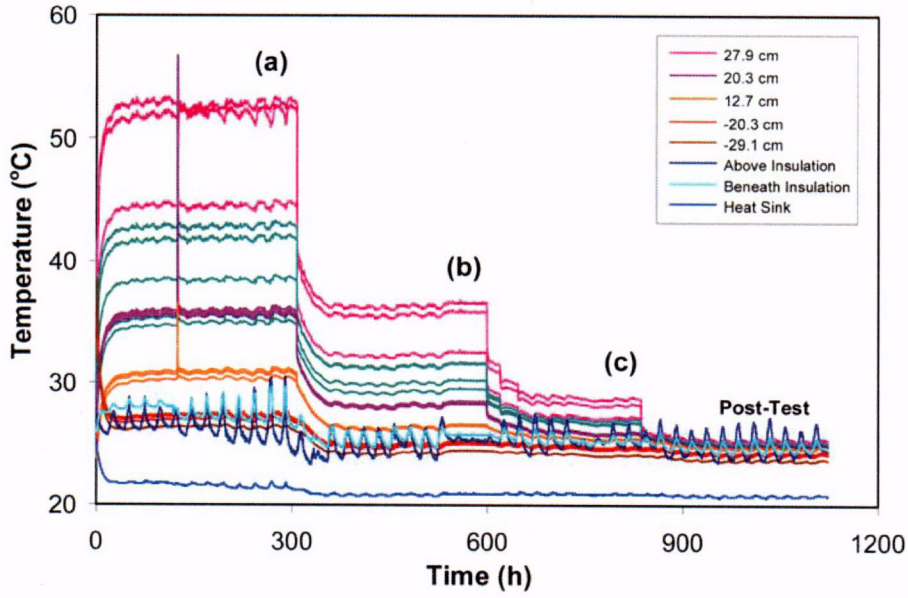

Figure 3-4. Plots of Time Profiles for Test #14 Using Selected Thermocouples in the Drift, Sand, and External Positions. Specified Locations Are the Axial Coordinates of the Drift. The Power Levels Were (a) 3.37 W [11.5 BTU/h], (b) 1.246 W [4.25 BTU/h] and (c) 0.343 W [1.17 BTU/h]. [(1.8 × T °C) + 32 = 1 °F; 2.54 cm = 1 in]

C-03

Figures 3-5 to 3-10 show the temperature variation at each cross-sectional array location. Cooler temperatures in the bottom half and hotter temperatures in the top half of the drift generally occur, except for locations immediately adjacent to the heater cartridge {i.e., arrays at x = 27.92 cm [11 in] and x = 24.11 cm [9.5 in]. A slight cooling of temperatures near the drift crown relative to the bulk air mass in the upper portion of the drift may reflect a boundary-layer effect. Symmetry about a vertical plane axially along the drift (x-z plane) was initially expected, but a nonsymmetrical and nonuniform pattern of temperatures apparently occurred. Temperatures above the heater in the array at x = 27.9 cm [11 in] suggest particular nonuniformity across a vertical axial plane, which may have been caused by the turbulence of the convective plume above the heater or by slight offsets in the actual heater setup. Given that the measurement uncertainty of the thermocouples was in the range of +/-0.2 °C for Test #11 and +/-0.5 °C for Test #14 [0.4 and 0.9 °F], nonuniformity of temperatures in arrays in the cooler half of the drift was suspect. Nonetheless, the air was generally hotter in the upper portion and cooler in the lower portion of the drift.

Figures 3-11, 3-12, and 3-13 display the temperature profiles along a vertical slice through the center of the drift and surrounding sand. Far from the heater (Figure 3-11), the temperature variation in the sand was less than the measurement sensitivity of the thermocouples, except for the highest power setting for Test #11. The temperature trends were consistent, however, with heat being conducted away from the drift. The temperature gradients in the sand near the heater (Figure 3-12) were more prominent. Comparison of the temperature profiles far and near the heater illustrate the wallrock effect on temperature gradients in the drift. Heat flux into the ceramic cylinder and sand decreases dramatically along the drift length, which violates the no-flux boundary condition in the analytical solution above and below the drift. Thus, it is important to include the cylinder and sand in computational fluid dynamics simulations.

The higher temperature gradient below the drift compared to above the drift near the heater in Test #11 (Figure 3-12) could have been caused by (i) a larger heat-transfer rate caused by convection in the partially saturated sand above the heater, (ii) conduction into axially along the ceramic cylinder and sand transferring heat directly from the heater cartridge and stand in contact with the drift floor, and (iii) preferential condensation on the drift floor and lower walls transferring latent heat to the drift floor and lower walls. Test #16, which was the dry test, exhibited the same trend of a higher temperature gradient below the drift than above the drift. Hence, latent-heat transfer was not dominating the heat transfer to the drift floor near the heater. This difference will be explored further in Section 3.4.

3.2.3 Condensation

Observations of axial air movement and measurement of 100-percent relative humidity in the drift indicated that a cold-trap process was occurring in the drift during early test phases. Direct and indirect observations of circulating air were also made. Anemometer probes were successful in registering flow rates in the lower (cool) half of the drift but not in the upper (hot) half. The flow rates were at or below rates considered to be measurement limits for the instrument {0.05 m/s [0.16 ft/s]}. All methods of locating the zones of higher flow rates in the upper half of the draft were unsuccessful, including dangling ribbons and positional adjustments of the anemometers.

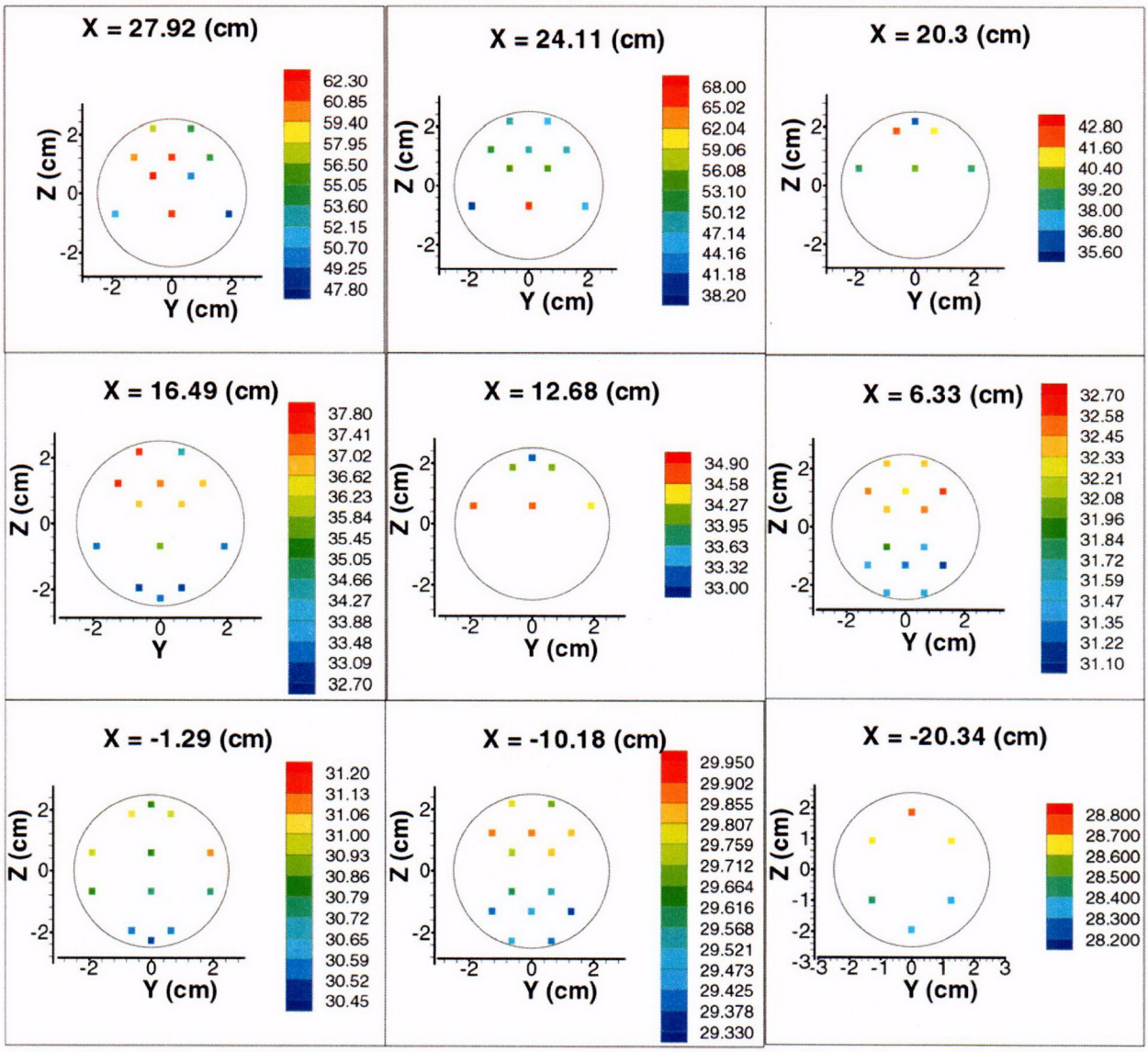

Figure 3-5. Plots of Cross-Sectional Data Inside the Drift for Test #11 Power Level at 5.251 W [17.9 BTU/h]. Specified Locations Are the Axial Coordinates of the Drift. [(1.8 × T °C) + 32 = 1 °F; 2.54 cm = 1 in]

C-04

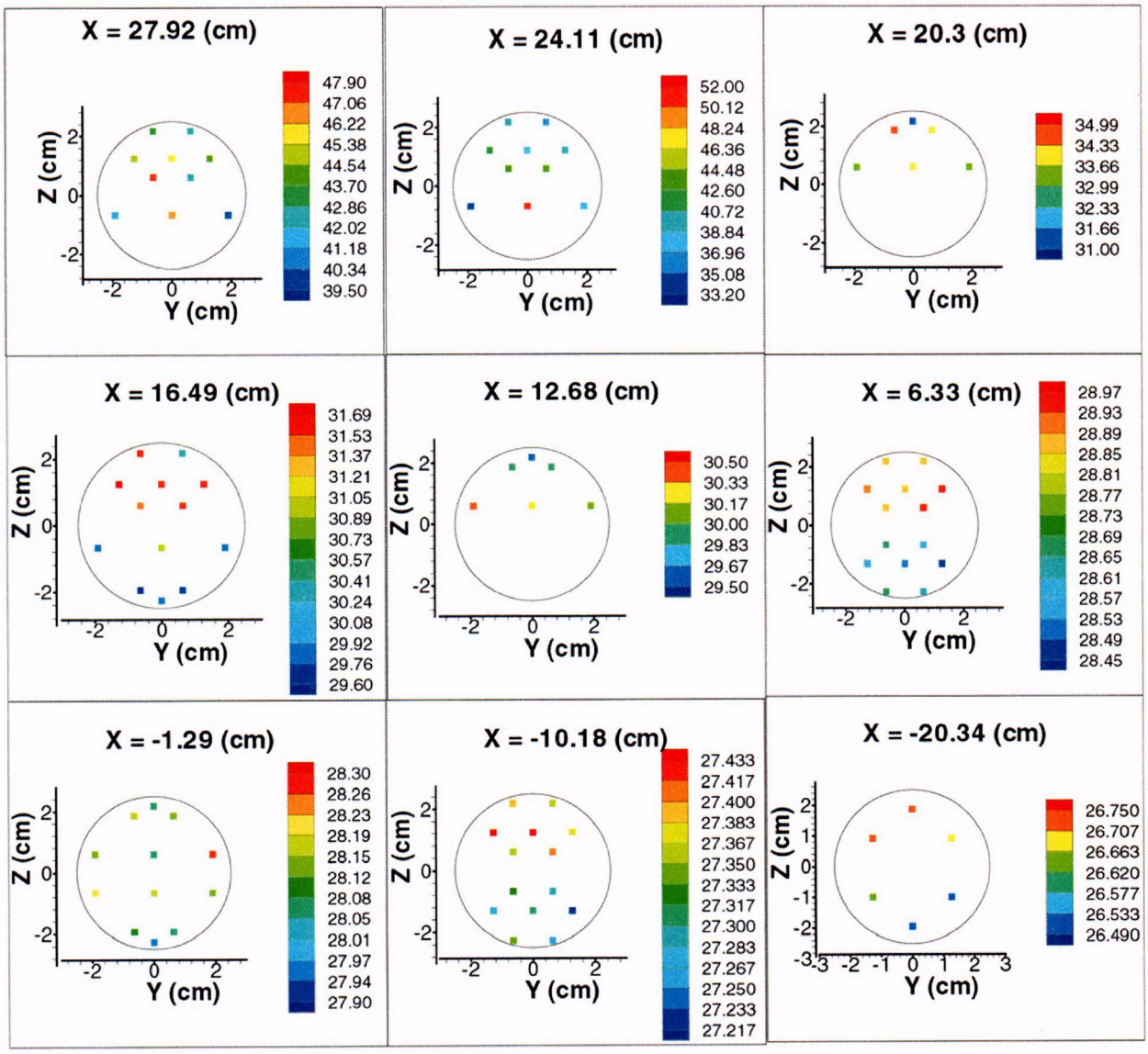

Figure 3-6. Plots of Cross-Sectional Data Inside the Drift for Test #11 Power Level at 3.37 W [11.5 BTU/h]. Specified Locations Are the Axial Coordinates of the Drift. [(1.8 × T °C) + 32 = 1 °F; 2.54 cm = 1 in]

C-05

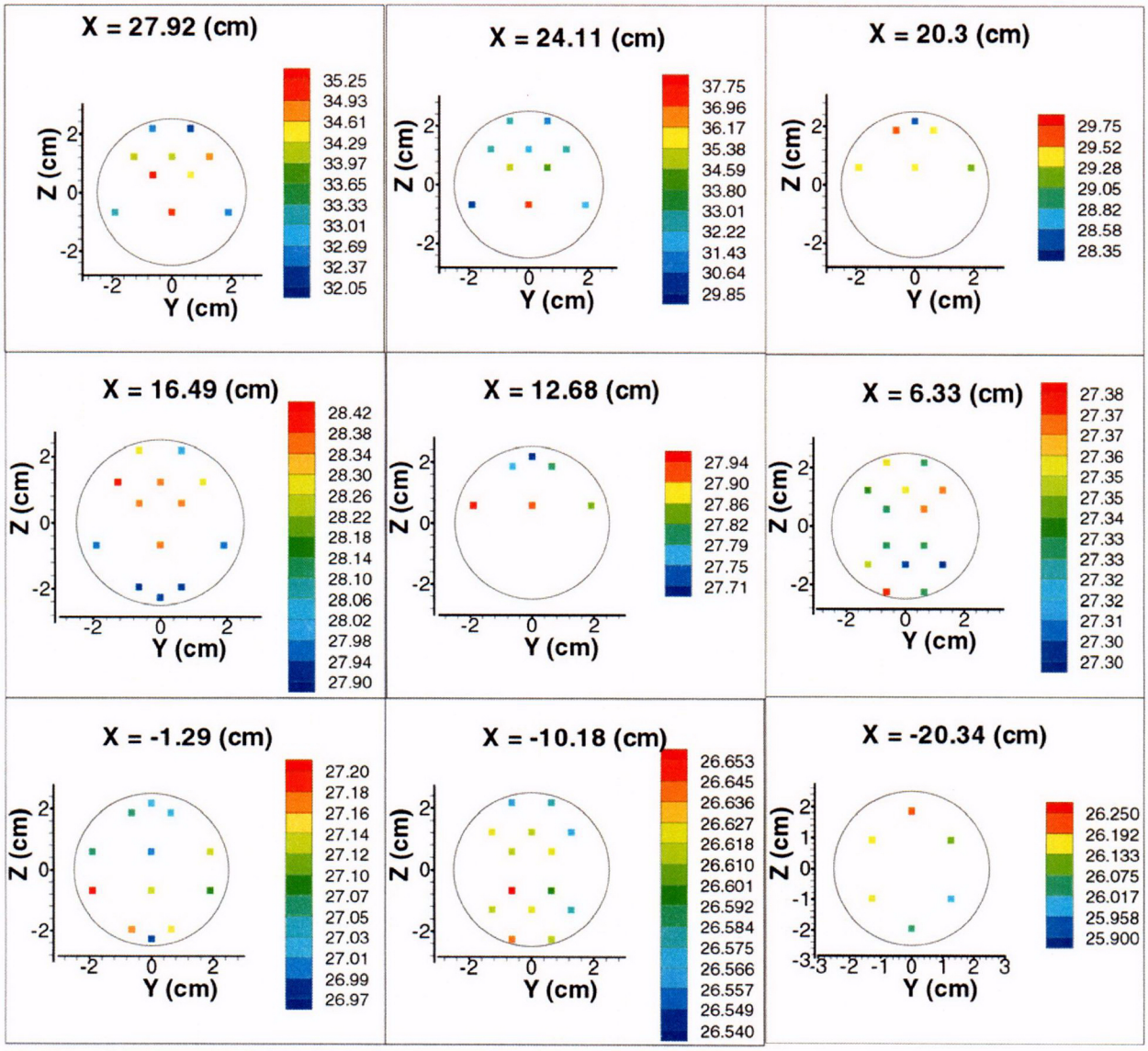

Figure 3-7. Plots of Cross-Sectional Data Inside the Drift for Test #11 Power Level at 1.246 W [4.25 BTU/h]. Specified Locations Are the Axial Coordinates of the Drift. [(1.8 × T °C) + 32 = 1 °F; 2.54 cm = 1 in]

C-06

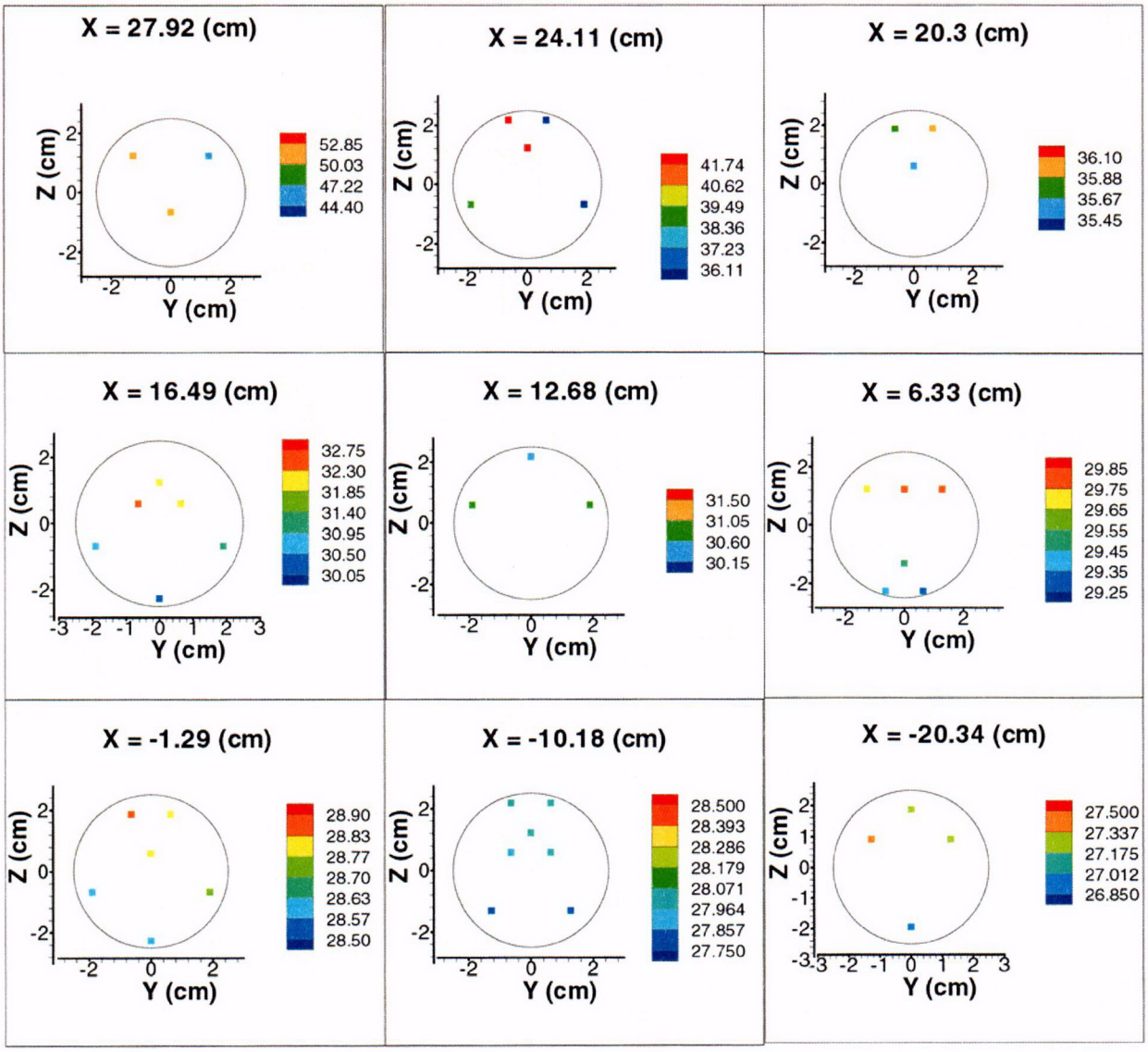

Figure 3-8. Plots of Cross-Sectional Data Inside the Drift for Test #14 Power Level at 3.37 W [11.5 BTU/h]. Specified Locations Are the Axial Coordinates of the Drift. [(1.8 × T °C) + 32 = 1 °F; 2.54 cm = 1 in]

C-07

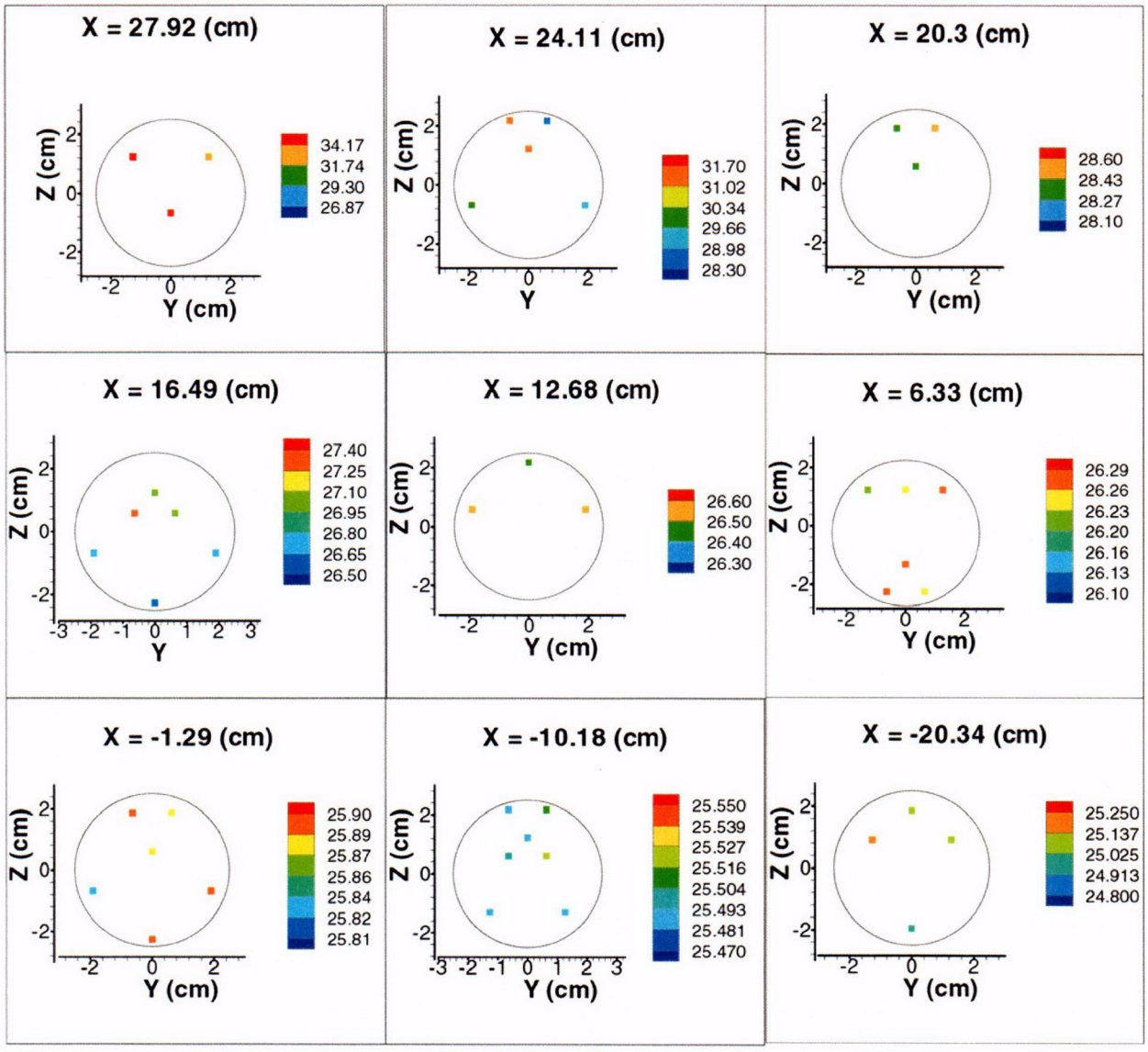

Figure 3-9. Plots of Cross-Sectional Data Inside the Drift for Test #14 Power Level at 1.246 W [4.25 BTU/h]. Specified Locations Are the Axial Coordinates of the Drift. [(1.8 × T °C) + 32 = 1 °F; 2.54 cm = 1 in]

C-08

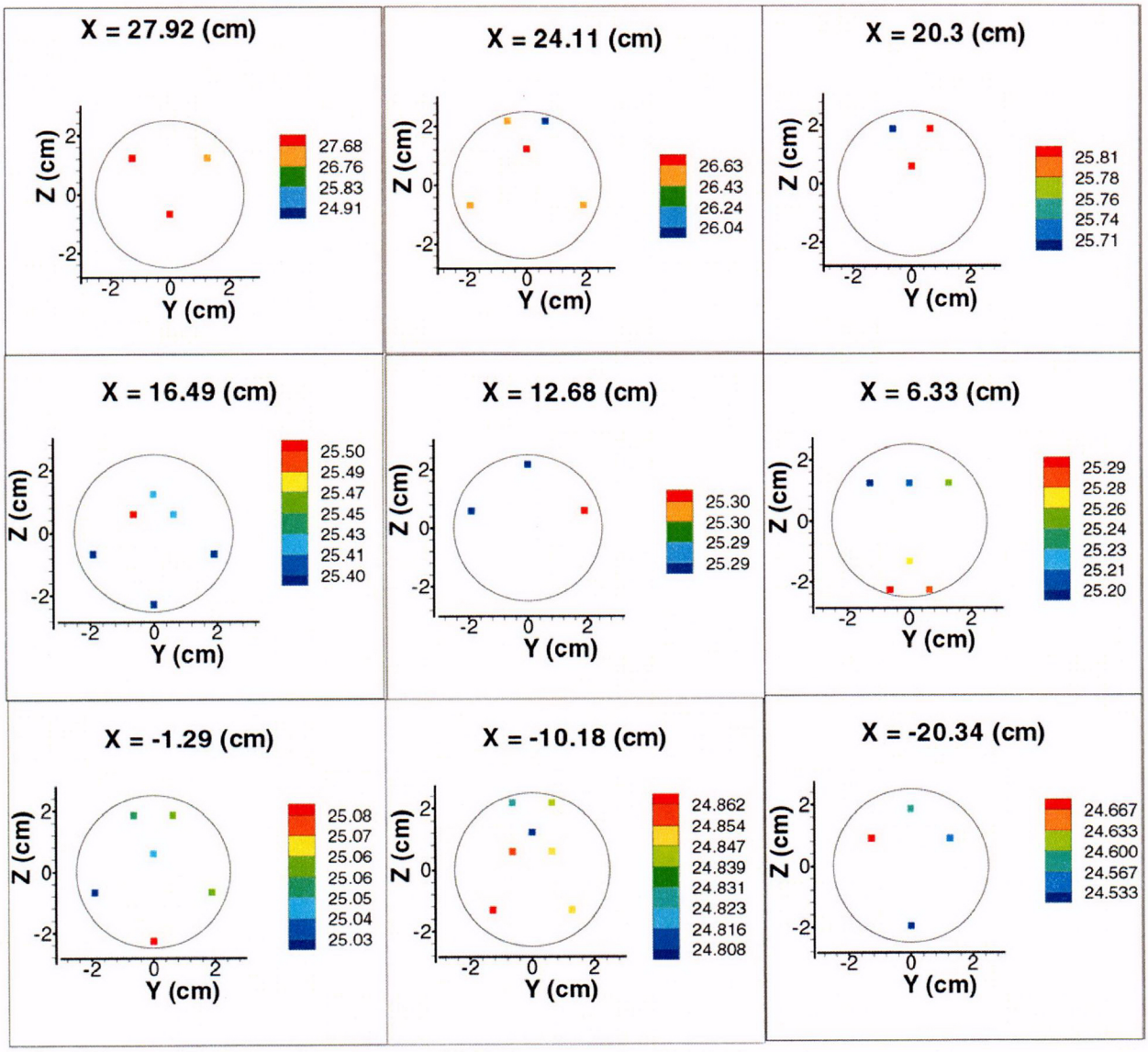

Figure 3-10. Plots of Cross-Sectional Data Inside the Drift for Test #14 Power Level at 0.343 W [1.17 BTU/h]. Specified Locations Are the Axial Coordinates of the Drift. [(1.8 × T °C) + 32 = 1 °F; 2.54 cm = 1 in]

C-09

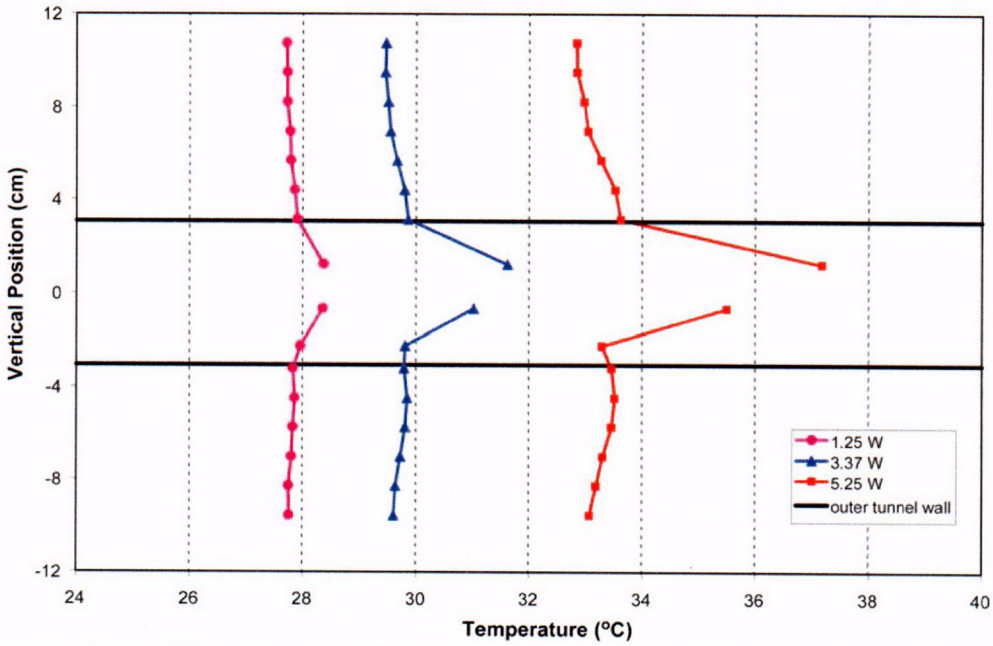

Figure 3-11. Plot of Temperature Profiles at the Axial Position of x = 16.5 cm [6.5 in] in the Sand for Test #11 for Three Power Levels [(1.8 × T °C) + 32 = 1 °F; 2.54 cm = 1 in; 1 W = 3.41 BTU/h]

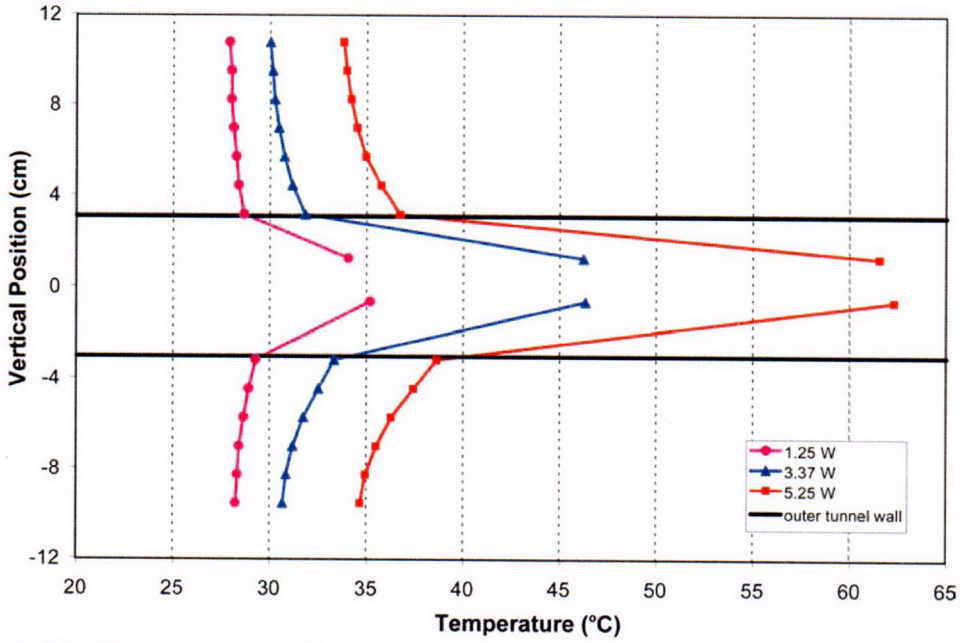

Figure 3-12. Plot of Temperature Profiles Near the Heater {at the Axial Position of x = 26.6 cm [6.5 in]} in the Sand for Test #11 for Three Power Levels [(1.8 × T °C) + 32 = 1 °F; 2.54 cm = 1 in; 1 W = 3.41 BTU/h]

C10

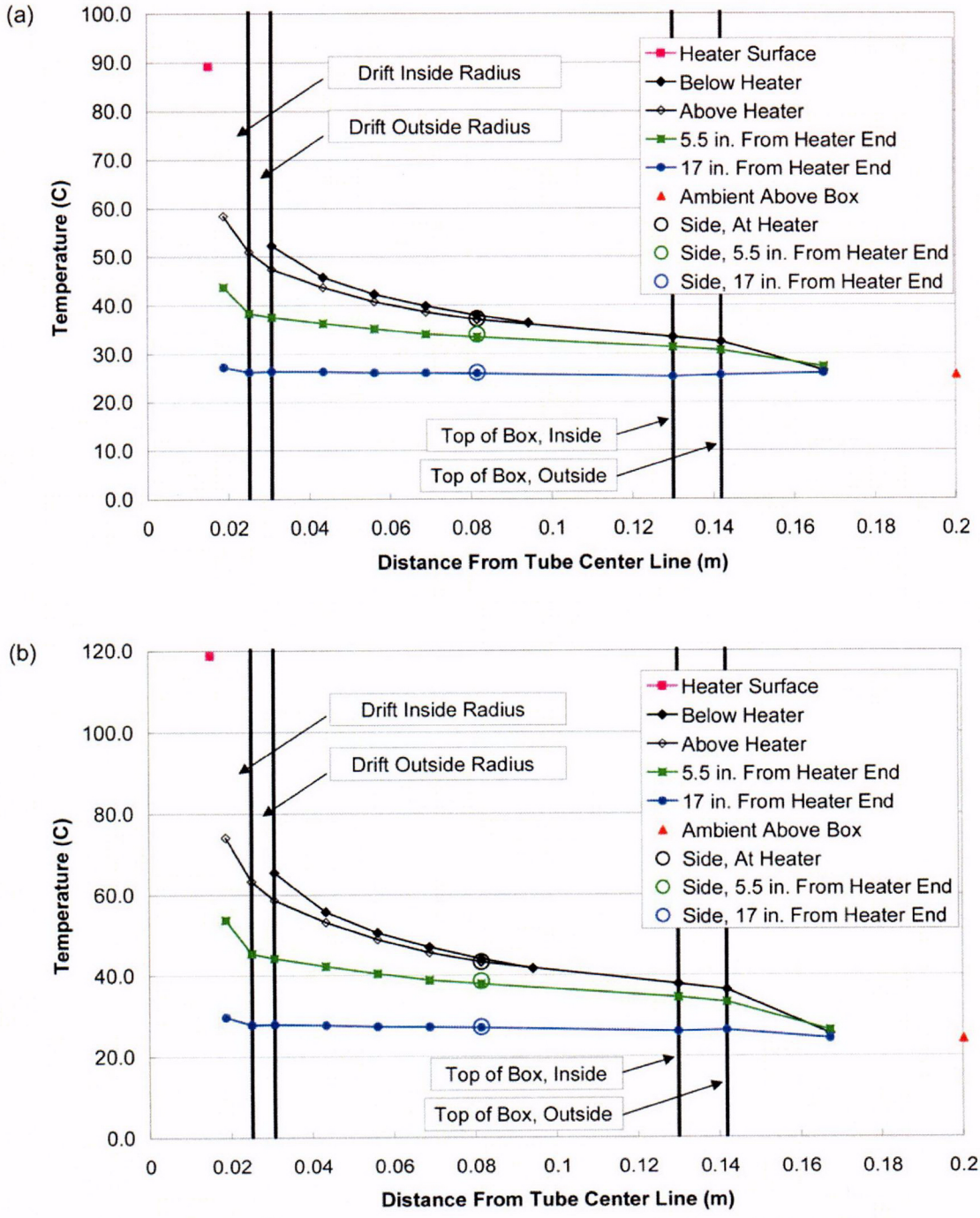

Figure 3-13. Plot of Temperature Profiles in the Sand for Test #16, (a) Phase 16d at a Power Level of 3.37 W [11.5 BTU/h] and (b) Phase 16e at a Power Level of 5.51 W [18.8 BTU/h]. [(1.8 × T °C) + 32 = 1 °F; 2.54 cm = 1 in]

C-11

Observations from early test phases indicated that 100-percent humidity was reached inside the cylinder and that the ceramic cylinder remained saturated. Relative humidity readings in the range of 94–98 percent near the heater would be expected because of the relative humidity decrease associated with an increase in temperature. The relative humidity would be essentially 100 percent at the inner wall of drift and there would be a temperature difference between the wall and an air-mass volume around the relative humidity probe. Condensation on and dripping from thermocouples, relative humidity probes, anemometers, and metal objects hung from the drift ceiling were also readily observed in early test phases. In addition, condensation on the interior heat-sink wall {maintained nominally at 22 °C [72 °F]} led to episodic rivulets of water cascading down to the base of the drift.

The observations of condensation in the drift led to a number of attempted approaches for collecting the condensate. The only method considered successful was the collection of water running off the heat-sink wall. Drops formed on the lexan wall eventually led to rivulets that were routed into a tube that remained saturated because of an inserted wick. Table 3-2 presents the steady rates of condensation measured flowing out of the tube that collected water from the heat-sink wall. Water was collected only during Test #14. The water collected off the heat-sink wall may just be a portion of the total condensed water in the drifts, hence models that could estimate the portion collected both on the endwall and along the drift were needed.

3.3 Observations Using Analytical Solution

The analytical airflow solution and condensation model were originally developed to support the design phase of the desktop cold-trap model and for preliminary interpretations of the cold-trap test. Once confirmed by comparisons with the numerical computational fluid dynamics simulations, the analytical solution could be used to quickly assess measured results from the desktop laboratory cold-trap model. Results from Section 3.4 confirmed that the analytical solution for airflow rates was reasonable. Figure 3-14 illustrates the variation in airflow rates for the upper or lower half of the drift estimated as a function of applied temperature difference between the hot and cold wall using the analytical solution. The associated total condensation rate for the entire length of the drift for the specified temperature difference is also shown in Figure 3-14.

Since the measured condensation was collected from the heat-sink wall, and not the entire drift, the model domain was discretized to obtain the condensation at cross-sectional locations along the drift. Nonuniform discretization allowed for refinement in zones of the large temperature gradients. Figure 3-15 illustrates the estimated cumulative condensation rate starting from the

Table 3-2. Measured Condensation Rate Collected from the Heat-Sink Wall During Test #14 for Different Temperature Gradients, ΔT [(1.8 × T °C) + 32 = 1 °F; 1.8 × ΔT °C = ΔT °F]

Approximate Temperature T °C	ΔT, °C	Water Rate, g/hr
53	32	0.038
36	15	0.022
29	8	0.020

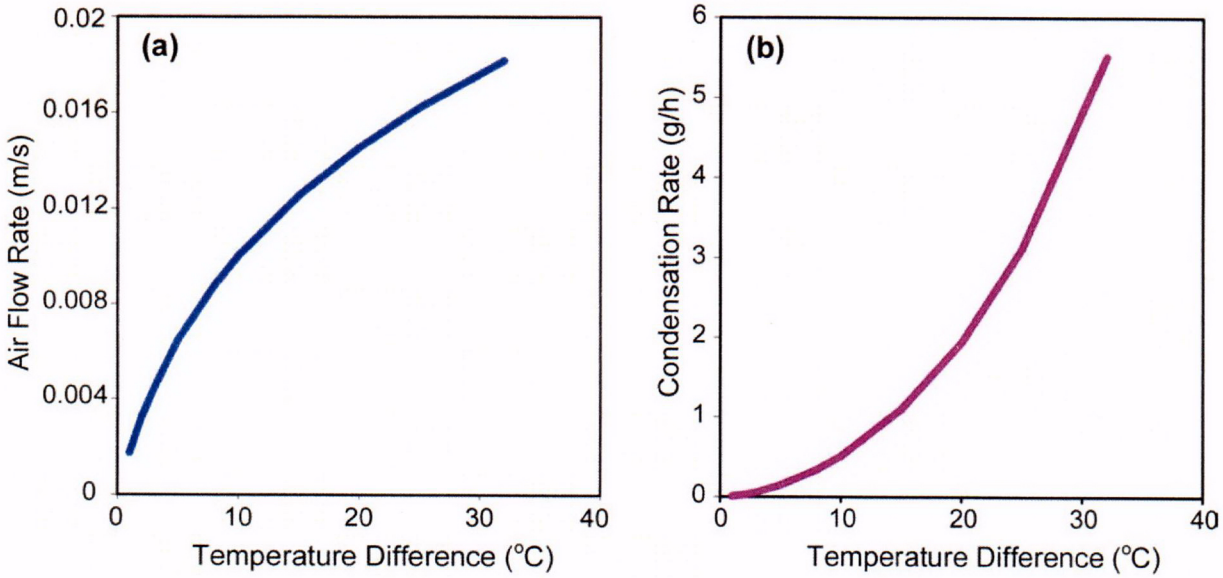

Figure 3-14. Airflow Rate (a) and Condensation Rate for the Entire Length of the Drift (b) as Functions of Temperature Difference Along the Drift Estimated Using the Analytical Solution [2.54 cm = 1 in; 1 °C = 1.8 °F]

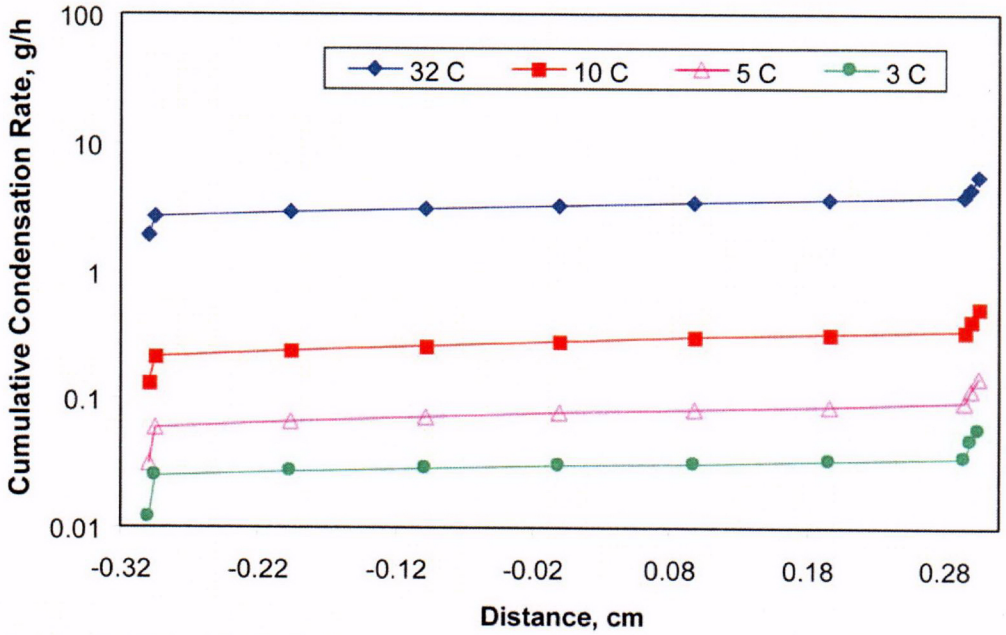

Figure 3-15. Cumulative Distribution of Condensation Along the Drift Estimated for the Desktop Laboratory Model Using the Analytical Solution Presented in Section 2.1. Four Different Temperature Gradients Are Presented. The Cumulative Distribution Is from the Cold Wall (x=0) to the Hot Wall {x = 61 cm [24 in]}. [2.54 cm = 1 in; 1 °C = 1.8 °F]

C-12

hot end and going to the cold wall. The central-drift region exhibits little condensation because the simulated temperature variation is much less than the gradients near the heater and the cold wall. For the analytical solution, most of the simulated condensation occurs near the heater and near the cold wall because this is where the temperature gradients are the largest.

A comparison of the measured and estimated condensation rates at the cold wall is shown in Figure 3-16. The small difference at low temperature differences was encouraging. But the order of magnitude difference in condensation at large temperature differences and the differences in the shapes of the curves for measured and analytical results are a function of temperature difference suggest that the model is not a good representation of actual physical processes. Henceforth, the usefulness of the analytical solution may be limited to being a design tool.

3.4 Computational Fluid Dynamics Modeling Results

The primary goal of the computational fluid dynamics modeling was to demonstrate that natural convection in the drift can transport moisture from the hot end to the cold end of the drift. As a secondary goal, the modeling of the laboratory-scale, cold-trap experiment was used to refine and verify the techniques for use in larger scale modeling by comparing the numerical and experimental results.

Simulations were conducted with power levels equal to those used in the laboratory experiment. Simulation results for each power level show basically the same results with variations only in the magnitudes of the temperature, velocities, and vapor transport rate; demonstrating that the vapor transport process was the same for each power level. For this report, only the results at a heater power level of 3.37 W [11.5 BTU/h] are discussed.

Because FLOW–3D® (Flow Science, Inc., 2003) is a transient simulator, the experiments were simulated until the model fluid and solid temperatures and velocities reached steady-state conditions. Effective heat capacities of the solid materials in the model were reduced to speed up the transient simulation time and reduce the required modeling duration. Even though the transient time was limited, it took on the order of 2 to 3 days of modeling time to reach steady-state conditions for each simulation.

3.4.1 General Flow Patterns

Delineation of detailed airflow patterns and magnitudes in the drift are the primary capabilities of the computational fluid dynamics modeling. Matching measured temperature values lends confidence to the estimates of airflow patterns and magnitudes. While there were some difficulties in matching the measured data, general airflow patterns would not likely change with a more refined model. These difficulties are discussed in Section 3.4.3.

Figures 3-17 and 3-18 show that natural convection in the drift causes hot air to move toward the cold end at the top of the drift, while cold air moves back toward the heater at the bottom of the drift. To distinguish this counterflow, positive values of x-velocity indicate flow that is moving from the cold end toward the hot end of the drift and negative values of x-velocity indicate that flow is moving from the heater end to the cold end. The conceptualization used by the analytical approach of one large convection cell with little axial variation in flow velocity is clearly not supported by the computational fluid dynamics modeling of the cold-trap laboratory

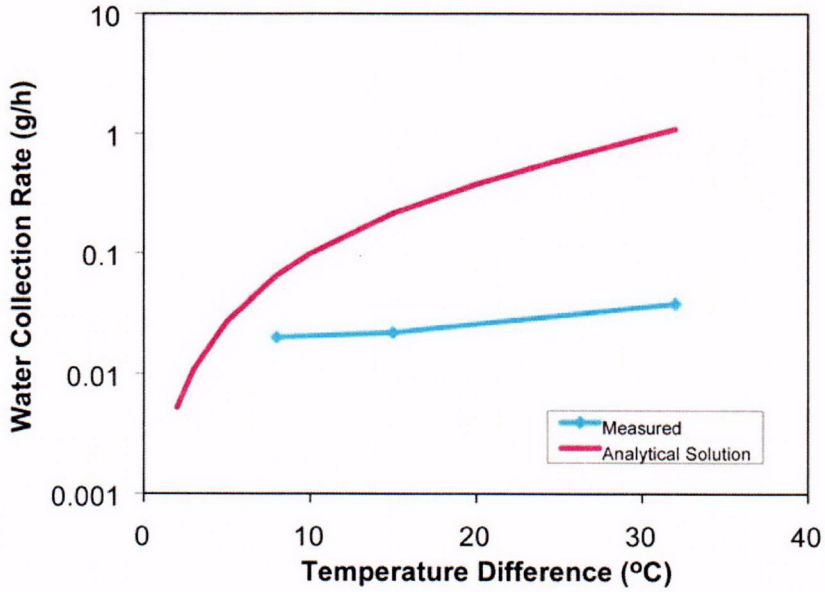

Figure 3-16. Comparison of Condensation Rates Measured on the Heat-Sink Wall During Test #14 with Those Estimated Using the Analytical Solution Presented in Section 2.1 [2.54 cm = 1 in; 1 °C = 1.8 °F]

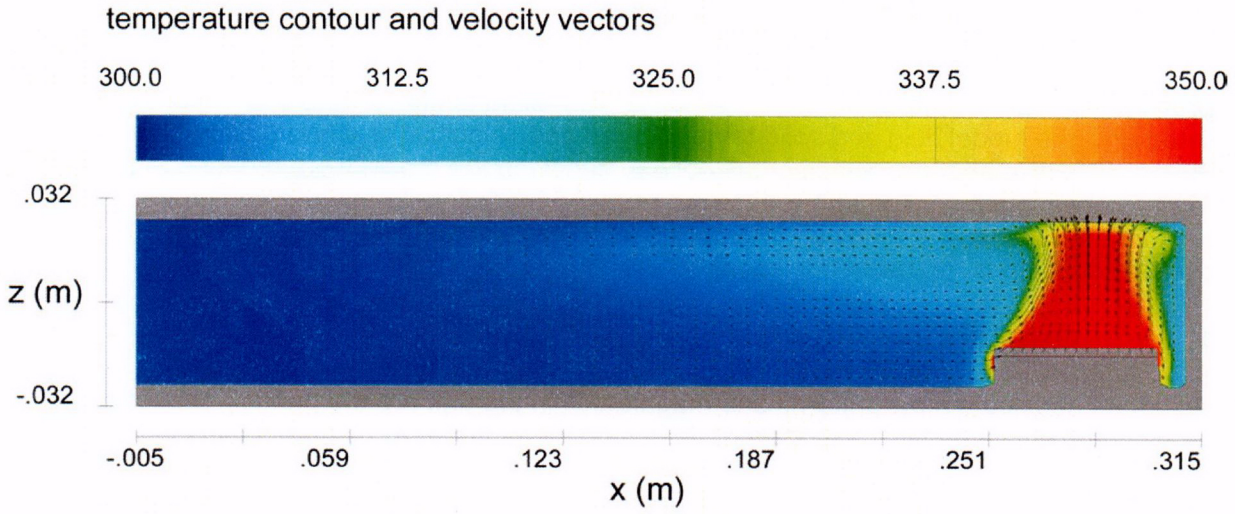

Figure 3-17. Simulated Temperature and Airflow Vector Data Plotted for Axial Cross Section of Hot Half of Drift Using Parameters for Test #11 and Power Level of 3.37 W [11.5 BTU/h]. Temperature Units Are K and Velocity Units Are m/s. [°F = 1.8 × T K – 459.67; 0.3048 m/s = 1 ft/s; 0.3048 m = 1 ft]

C-B

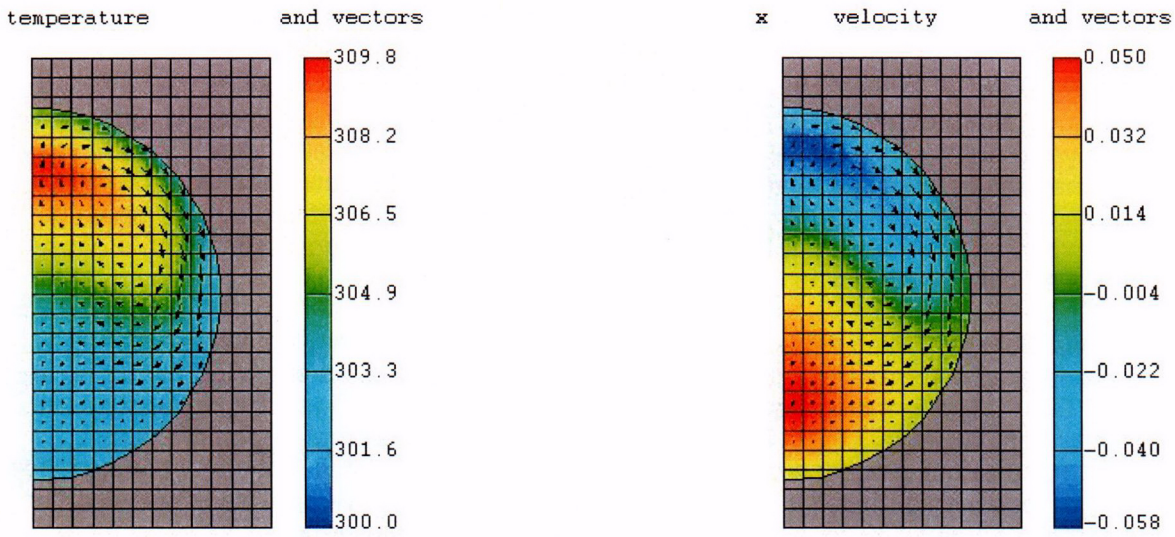

Figure 3-18. Contour and Vector Plots of the Computational Fluid Dynamics Results with a Heater Power of 3.37 W [11.5 BTU/h] for a Drift Cross Section at x = 0.202 m [0.663 ft]. The Left Plot Shows the Temperature Contour. The Right Plot Shows the x-Velocity (Along the Axis of the Tunnel) Contour. Both Plots Show the y-z Velocity Vectors of the Fluid Flow. Units Are Temperature in K and Velocity in m/s. [°F = 1.8 × T K - 459.67; 0.3048 m/s = 1 ft/s; 0.3048 m = 1 ft]

experiment. Figure 3-17, which displays the hotter half of the drift, better illustrates the behavior in the zone of the largest temperature gradients and shows the tailing off of flow magnitudes. In the cooler half of the drift, temperature gradients and airflow velocities drop off substantially. The short circuiting of airflow is illustrated by the reduction in the flow magnitude (vector symbols scaled to the velocity in the x-z plane) of Figure 3-17. Short-circuiting airflow in the upper part of the drift trails off vertically downward into the lower part of the drift and curls back towards the heater.

The short-circuiting has strong implications for condensation. Depending on the relative humidity at the hot locations, condensation would be distributed all along the convective cell but would dominantly occur nearer the hot location where the temperature gradients are the greatest. The sharp drop in the axial profile of temperatures near the heater cartridge (inferred by comparing cross sections for any steady-state case in Figures 3-5 to 3-10) suggests that this zone has the greatest condensation potential.

Small depressions in the relative humidity values above the heater cartridge due to the temperature difference between the drift wall and air mass above the cartridge would mean that condensation would occur further down gradient (temperature) than for higher values of relative humidity near the hot zone. The short circuiting of airflow, however, means that relative humidity would be more quickly elevated back up to the saturated air values than if no short circuiting occurred. The temperature of the hot-air mass leaving the heater cartridge area would be dropping quickly because of (i) evaporation from the drift wall and associated latent-heat transfer,

C-14

(ii) heat flux out of the drift through the walls, and (iii) vertical movement of the air mass and mixing with cool return air lower in the drift.

The small amount of water collected from the heat sink wall in Test #14 supports the short-circuiting pattern of airflow. It also supports the hypothesis that there is little or no boundary-layer resistance for condensation occurring on the drift endwall, though boundary-layer resistence may still be an issue near the heater where convection airflow rates would be much larger. Noting that results from the desktop cold-trap experiment cannot be directly translated to conditions expected at Yucca Mountain, the short-circuiting pattern suggests that future efforts should focus on zones proximal to hot zones along a drift.

Computational fluid dynamics modeling results support the expected asymmetrical cross-sectional flow patterns (Figure 3-18) near the heater cartridge, as predicted by Kuehn and Goldstein (1978). The resulting temperature distribution around the inner drift wall leads to a distribution of heat fluxes into the drift wall that varies around the circumference of the drift (Figure 3-18) and axially along the drift (Figure 3-17). The use of effective thermal conductances in the DOE porous media models neglects these aspects of convective heat transfer. Also, the more dispersed high-velocity zone in the upper portion of the drift in comparison to the more focused zone of return airflow in the lower portion of the drift appears to address difficulties in registering airflow using the anemometer during early phases of the cold-trap experiment.

3.4.2 Vapor Transport Estimates

Demonstration of vapor transport was accomplished by modeling the laboratory cold-trap experiment, extracting the fluid temperature and velocity information in the drift from the numerical results, and then performing the moisture transport calculations described in Section 2.3. Figure 3-18 shows temperature and x-velocity contour plots with the y-z flow velocity vectors of the fluid at one of the cross sections along the drift. This figure allows for a further explanation of the post-processing technique used to estimate vapor transport along the drift.

As described previously, the results obtained from the computational fluid dynamics models represent dry air in the drift. Vapor transport is estimated by first extracting from the computational fluid dynamics results the temperature, x-velocity, and y-z area of each cell in the drift at a particular cross section. The cell fluid temperature is used to estimate the mass of water in each cell with the assumption that the air is saturated. Combining this information with the x-velocity and area of each cell provides an estimate of the water transport rate for each cell. Water transport for all the cells at each cross section along the drift are then added to provide the total vapor transport in the drift.

The contour plots in Figure 3-18 show the key information used for this post-processing analysis. Because of the natural convection in the drift, the warmer air at the top of the drift moves from the heater end to the cold end of the drift; the cooler fluid moves along the bottom of the drift back toward the heater. The variation in simulated temperature and airflow rate along the drift automatically accounts for the short circuiting. At saturated conditions, the warmer air holds more water and therefore transports more water away from the heater than the cooler air transports back to the heater. In this case, where the relative humidity is high near the heater, the net transport rate is such that moisture moves down the drift away from the heater. Recall that in the computational fluid dynamics coordinate system the positive x-direction is axially along the drift from the cold end to the hot end, so this net flow rate, away from the heater, has a negative magnitude.

The results of these calculations for each cross-section along the drift are shown in Figure 3-19. The plot shows the net vapor flow rate and the negative component of the airflow rate flowing along the drift. Only the negative component of the airflow rate is shown because the net airflow rate is zero due to conservation of mass. The analysis shows that the vapor transport rate decays to zero near the mid-point of the drift (x = 0). The airflow rate decays in a similar manner, but it continues to flow down to the end of the drift at the cold wall. The reason that the net vapor rate does not continue with the airflow rate past the midpoint of the drift is because there is no temperature differential between the positive and negative airflow at these cross-sections. In other words, the air flowing in the negative direction (away from the heater end) is transporting the same amount of vapor as the air flowing in the positive direction (toward the heater) in this half of the drift.

An interesting feature illustrated in Figure 3-19 is the disturbance in both the airflow and vapor flow at the heater. This is due to the distinctive thermal plume rising from the heater caused by the convection above the heater surface. Figure 3-20 shows a temperature contour plot of the fluid around the heater in the x-z plane at the drift centerline. The velocity vectors to the left of the plume from x = 0.260 to 0.280 m [0.85 to 0.92 ft] and close to heater surface show a positive x component. This fluid is hotter than the fluid at the top of the drift, which has a negative x-component of the velocity vector. Therefore, the calculated net vapor transport rate is positive, which explains the positive values shown around the heater in Figure 3-19. These results are misleading, because the assumption that the fluid is at saturated conditions is most likely not valid in this region near the heater, where the air is heated quickly. It is also suspect whether enough water will be present and the diffusion rate will be adequate to keep the air at saturated conditions. Most likely the air will be well under the saturation point, making the analysis technique invalid in this region. However, this should not affect the estimated transport rate calculations in the remaining portions of the drift, since it is reasonable to assume that, in these regions, the air will be saturated and at equilibrium.

Two key assumptions were made in the computational fluid dynamics analysis of the laboratory-scale cold-trap experiment. The first assumption was that latent heat of vaporization was negligible compared to the overall heat transfer from the heater to the moist air. To simulate latent-heat transfer, evaporation and condensation modules would need to be developed for FLOW–3D® (Flow Science, Inc., 2003). Including the condensation process in a computational fluid dynamics code is not straightforward. Evidence negating the assumption of negligible latent-heat transfer was deemed necessary before embarking on the extensive effort to create a condensation algorithm for FLOW–3D® (Flow Science, Inc., 2003). To verify this assumption, the latent heat of fusion was calculated using the estimated moisture transport rate at the exit of the heater. This calculation showed that the estimated transport rate of 6 g/hr (near the heater) would require approximately 4 W [14 BTU/h] of latent heat. This was obviously impossible since the total heater power was only 3.37 W [11.5 BTU/h], indicating that this key assumption was invalid. In reality, since latent heat is significant, the temperatures and flow rates around the heater are much lower than the simulated values. The fact that this assumption was invalid limits the reliability of the magnitude of the estimated transport rate. The zone of high temperature gradients should correspond with the zone of highest potential condensation. While the magnitude of the simulated and measured temperature gradients differ in the high-gradient zone, the simulated temperatures in the remainder of the drift closely match the measure values. Thus, the computational fluid dynamics results are useful for identifying the zone of highest condensation potential, even though the assumption of negligible latent-heat transfer is apparently violated.

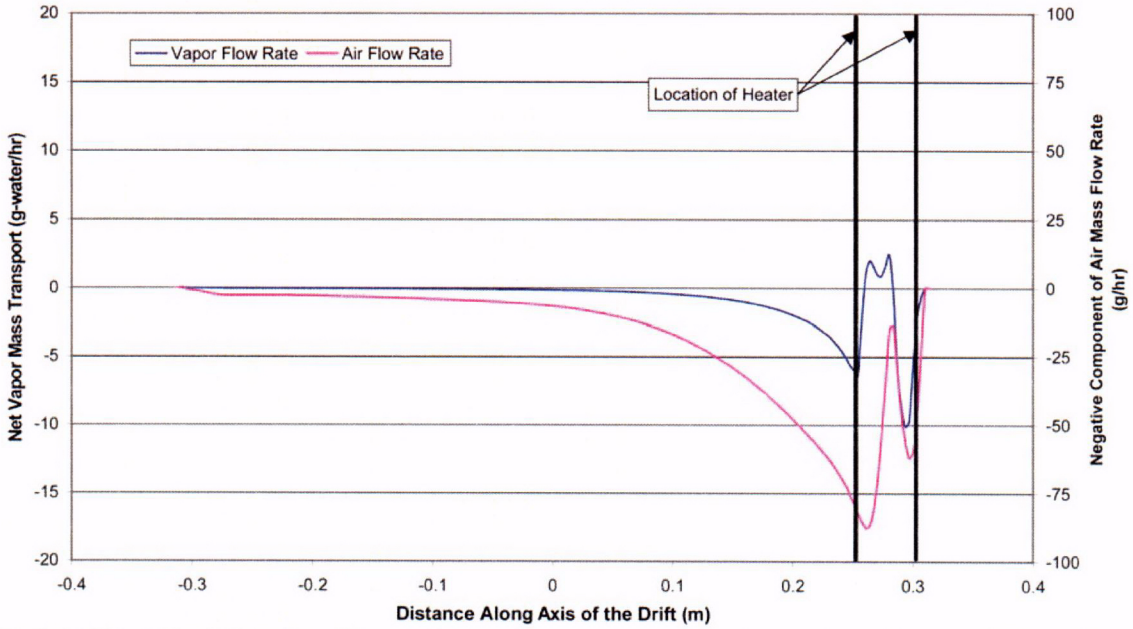

Figure 3-19. Plot Showing Numerical Analysis Results of the Flow Rate at Which Vapor and Air Are Transported Along the Drift Due to Natural Convection. The Case Shown Is With a Heater Power of 3.37 W [11.5 BTU/h].
[0.3048 m = 1 ft]

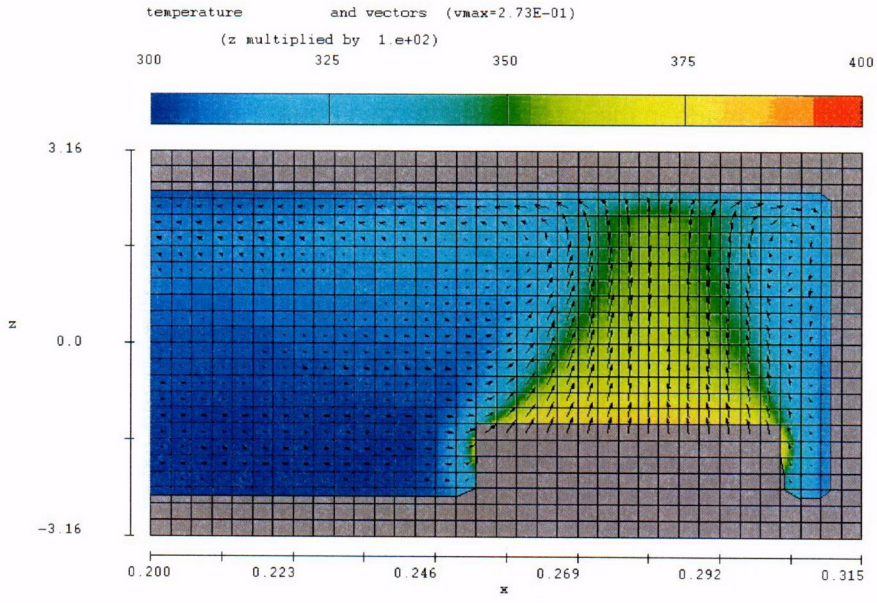

Figure 3-20. Temperature Contour and Velocity Vector Plot of the Computational Fluid Dynamics Results for a Vertical Axial Slice Along the Center of the Drift Illustrating Distinctive Thermal Plume Above Heater Cartridge. The Case Shown Is With a Heater Power of 3.37 W [11.5 BTU/h]. Units of Temperature in K and Velocity in m/s.
[°F = 1.8 × T K−459.67; 0.3048 m/s = 1 ft/s]

C-15

The second assumption was that the diffusion rate for evaporation from the inner drift walls was faster than the convection rate along the drift. Evidence that this assumption may be violated was that the estimated latent heat from condensation was larger than the power input to the heater cartridge. Since condensation should equal evaporation in a steady-state system, the evaporation may be over-predicted. Near the heater would be the most likely zone where the diffusion rate would be less than the convection rate. The assumptions regarding negligible latent-heat transfer and boundary-layer diffusion rate comparable to convection rates, will have to be addressed in a future report.

3.4.3 Comparison of the Computational Fluid Dynamics Results with Laboratory Results

The computational fluid dynamics results were compared to the measured results for steady-state conditions for three different test cases: two tests with wet sand (Tests #11 and #14) and one test with dry sand (Test #16d). The only change made to the computational fluid dynamics model for the dry and wet simulations was in the value for the thermal conductivity of the sand. The thermal conductivity used for wet sand was a uniform 1.76 W/m/K [24.4 BTU/h/ft/°F]; the conductivity used for dry sand was 0.22 W/m/K [3.1 BTU/h/ft/°F]. The wet sand tests were compared for heater powers levels of 1.25, 3.37, and 5.25 W [4.27, 11.5, 17.9 BTU/h]. The dry test was compared at 3.37 W [11.5 BTU/h]. Only the 3.37-W [11.5-BTU/h] results are discussed in this report. Similar conclusions can be drawn from the other two sets of data.

For convenience, the simulated temperatures were compared to thermocouple readings at locations in the apparatus where a series of thermocouples were placed at the drift center and arranged in a vertical line in the z-direction. Using these measurements for comparison allowed for more efficient data reduction and for a comparison of temperature gradients in the air and solid materials. Figure 3-21 shows a schematic of the test apparatus with the locations in the drift where the simulated and measured results were compared.

Figures 3-22, 3-23, and 3-24 show comparisons of the computational fluid dynamics and measured fluid temperatures at different locations along the drift for Tests #11 and #14 (wet tests). The data at x = 0.279m [0.915 ft] (Figure 3-22) shows the largest discrepancy between the measured data and the computational fluid dynamics results. The estimated fluid temperatures at this location are approximately 45 °C [81 °F] hotter than the measurements. The data at x = 0.165 m [0.541 ft] (Figure 3-23) show somewhat better comparisons with the computational fluid dynamics temperatures, deviating by approximately 2 °C [4 °F] from the measurements. The temperature gradient for the computational fluid dynamics results show the same trend as the measured data, with the hotter fluid at the top of the drift. The magnitudes of the temperature variation are slightly different though, with the computational fluid dynamics results showing a temperature distribution ranging from approximately 29 to 32.8 °C [84 to 91.0 °F] and the measured results ranging from approximately 29.6 to 31.8 °C [85.3 to 89.2 °F]. The data at x = 0.063 m [0.207 ft] (Figure 3-24) show a decent match {less than 0.5 °C [0.9 °F] difference} between the computational fluid dynamics results and the measured results of Test #11. An additional observation is that there appears to be a slight temperature discrepancy between Test #11 and #14 at this location in the drift.

Figures 3-25 and 3-26 show comparisons of the computational fluid dynamics results and the measured temperatures in the solid materials (drift tube, sand, lexan, and insulation) of

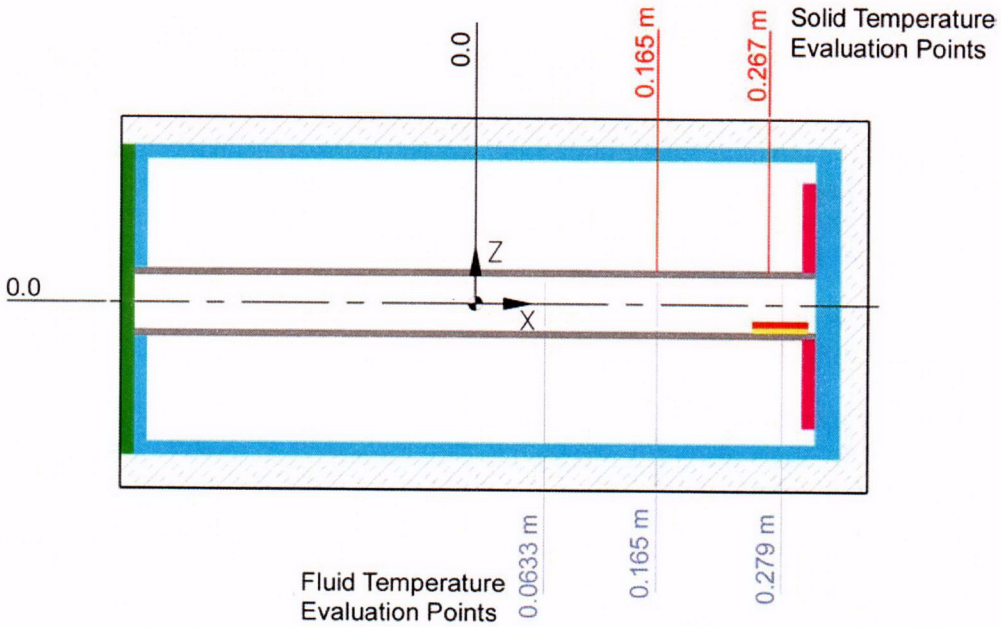

Figure 3-21. Computational Fluid Dynamics Model with Locations Along the Drift Where the Computational Fluid Dynamics Results Were Compared to the Test Results. A More Detailed Schematic of the Computational Fluid Dynamics Model Is Included in Appendix A. Units Are Meters [1 m = 0.3048 ft].

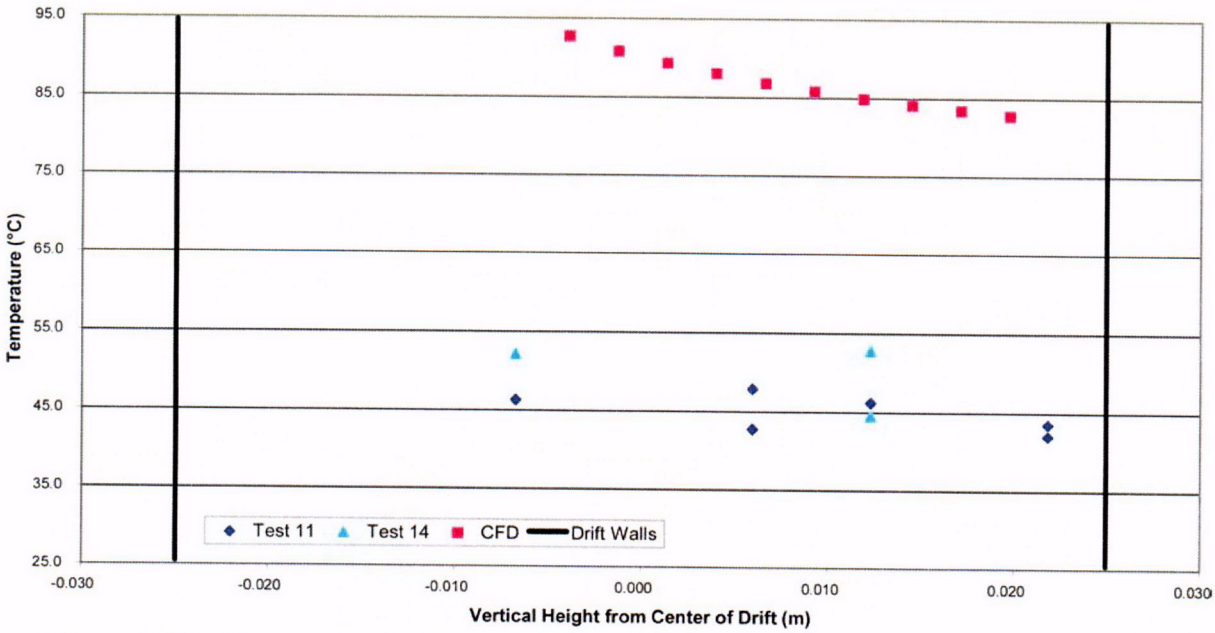

Figure 3-22. Comparison of Computational Fluid Dynamics Modeling Results and Measured Fluid Temperatures at x = 0.279 m [0.915 ft] (~ Center of Heater) [°F = 1.8 × T °C + 32; 0.3048 m = 1 ft]

C-16

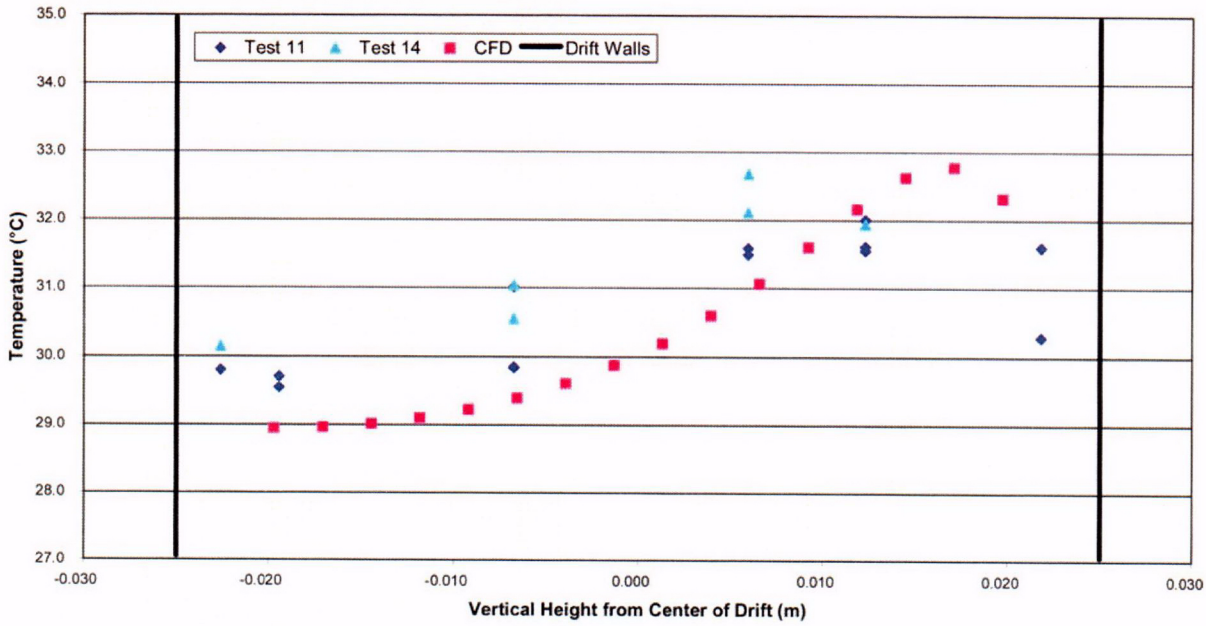

Figure 3-23. Comparison of Computational Fluid Dynamics (Shown as CFD in Figure) Modeling Results and Measured Fluid Temperatures at x = 0.165 m [0.541 ft] (Midway Between Heater and Mid-Plane of the Drift) for Test #11, Power Setting of 3.37 W [11.5 BTU/h] [°F = 1.8 × T °C + 32; 0.3048 m = 1 ft]

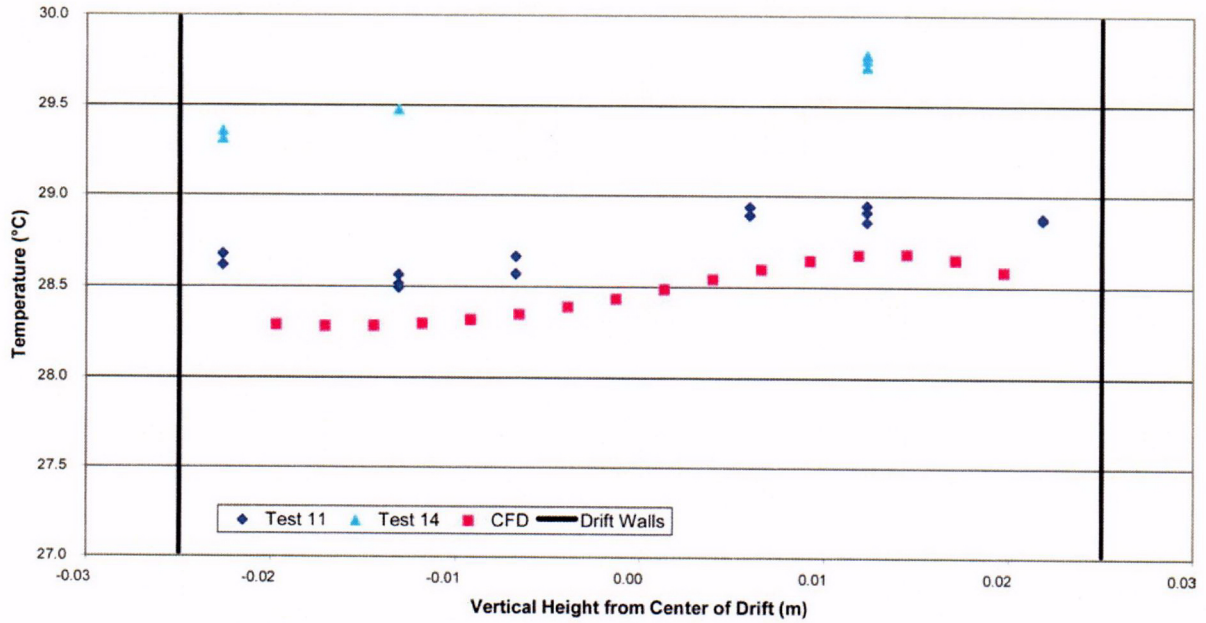

Figure 3-24. Comparison of Computational Fluid Dynamics (Shown as CFD in Figure) Modeling Results and Measured Fluid Temperatures at x = 0.063 m [0.207 ft] (Near Mid-Plane of Drift) [°F = 1.8 × T °C + 32; 0.3048 m = 1 ft]

C-17

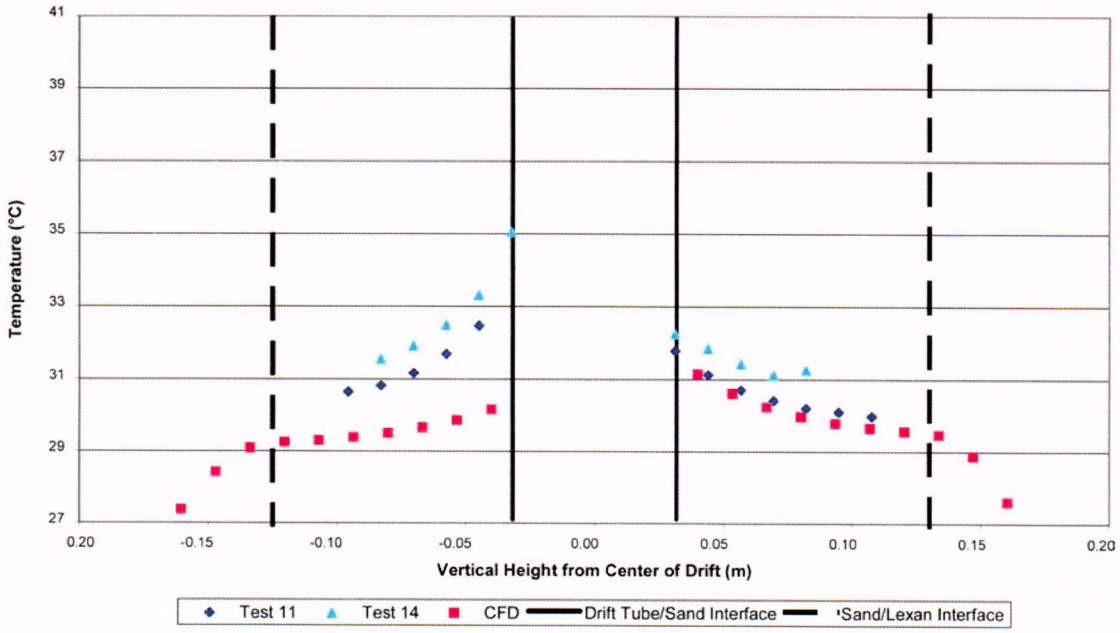

Figure 3-25. Comparison of the Measured and Computational Fluid Dynamics Temperatures in the Solid Materials of the Model. Data Shown is at x = 0.267 m [0.876 ft] (~ Heater Mid-Point) [°F = 1.8 × T °C + 32; 0.3048 m = 1 ft]

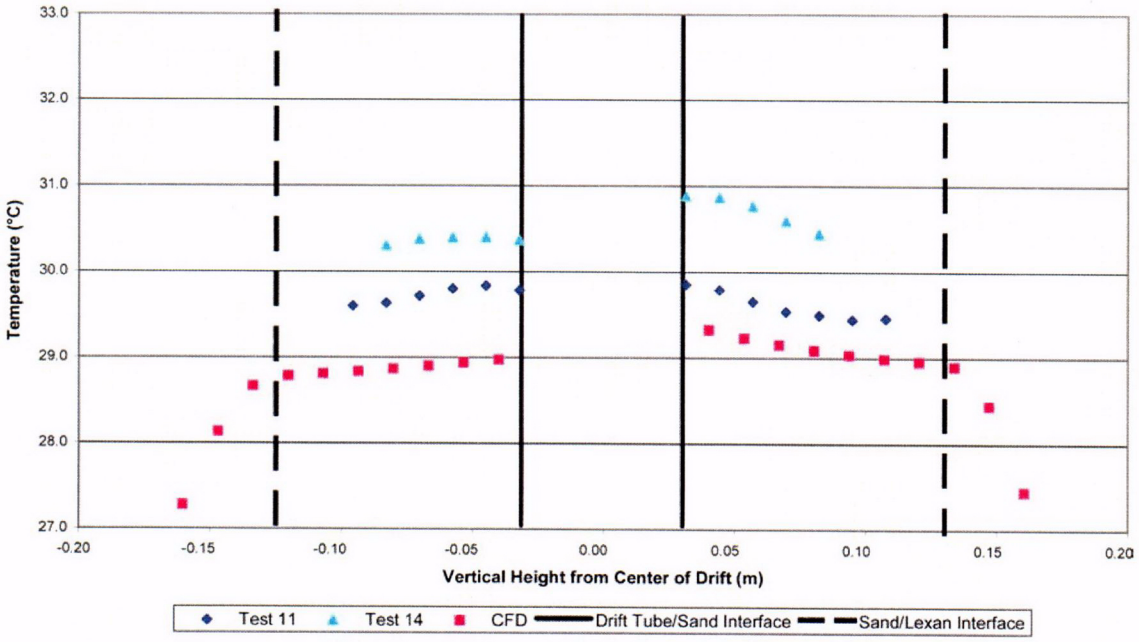

Figure 3-26. Comparison of the Measured Temperatures and Results From Computational Fluid Dynamics Simulations in the Solid Materials of the Model. Data Shown is at x = 0.165 m [0.541 ft] (~ Heater Mid-Point). [°F = 1.8 × T °C + 32; 0.3048 m = 1 ft]

C-18

Tests #11 and #14 (wet tests). The data in Figure 3-25 compares the temperatures in the sand above and below the heater and shows that the computational fluid dynamics results are 2–7 °C [4–13 °F] lower than the measurements for Tests #11 and #14. One observation regarding these data is that, for both test #11 and #14, the temperatures in the sand below the heater were higher than the temperatures in the sand above the heater. The computational fluid dynamics results showed the opposite trend–the temperatures below the heater were lower than those above. A second discrepancy to note is the temperature gradient in the sand. The gradient appears to match fairly closely for the sand above the heater, but below the heater, the measured gradient is much higher than the computational fluid dynamics results show. A third observation is that, like in Figure 3-24, there is a temperature discrepancy between the results for Tests #11 and #14 for the solid materials at this location. The data at x = 0.165 m [0.541 ft] (Figure 3-26) shows similar results to those shown in Figure 3-25. The computational fluid dynamics results matched fairly closely with measurements for Test #11 for the thermocouples above the drift. At this location there is no substantial difference in the gradients above or below the drift between the computational fluid dynamics results and measured results. A final observation is that discrepancy between the temperatures of Test #11 and #14 are also present at this location in the drift. Possible reasons for the discrepancies will be discussed later.

Figures 3-27 and 3-28 compare the computational fluid dynamics results with the measured air and solid temperatures for the dry test conducted at 3.37 W [11.5 BTU/h] (Test #16d). The results show similar trends to the data for Tests #11 and #14. At the heater (Figure 3-27), the estimated air temperature is significantly hotter. The solid temperatures above the heater do match fairly well, with the simulation results approximately 1.5 °C [2.7 °F] below the measured temperatures. The same trend in solid material temperatures above and below the heater is observed in both the wet-test and dry-test data. The measured data indicate that the solid material below the heater is hotter than the material above the heater. The simulated results show the opposite trend with the material below the heater cooler than the material above the heater. The data at x = 0.165m [0.541 ft] (Figure 3-28) shows a good comparison between both the air temperature and the solid temperatures above the drift. One interesting observation is that the simulated air temperature at this location is slightly lower than the measured air temperature. Recall that at the heater (Figure 3-27) the computational fluid dynamics air temperature was ~20 °C [36 °F] hotter than the measured results. Thermocouples were not placed below the drift at this location so these temperatures cannot be compared.

3.5 Summary of Observations From Computational Fluid Dynamics Simulations

Computational fluid dynamics modeling was used to show the general pattern of convection adjacent to a heated zone in a drift. The magnitude of flow and resultant estimates of condensation, however, are considered qualitative at this time. Further refinement of the numerical modeling is needed to better match the measured data in the desktop laboratory cold-trap experiment. Important differences between the numerical model and the measured data include the following items:

- The simulated air temperatures at the heater are significantly hotter than the measured results for both the wet and dry tests (see Figures 3-22 and 3-27). At locations further down the drift (away from the heater) the overall estimated air temperatures match fairly closely with the measured temperatures (see Figures 3-23, 3-24, and 3-28). Therefore,

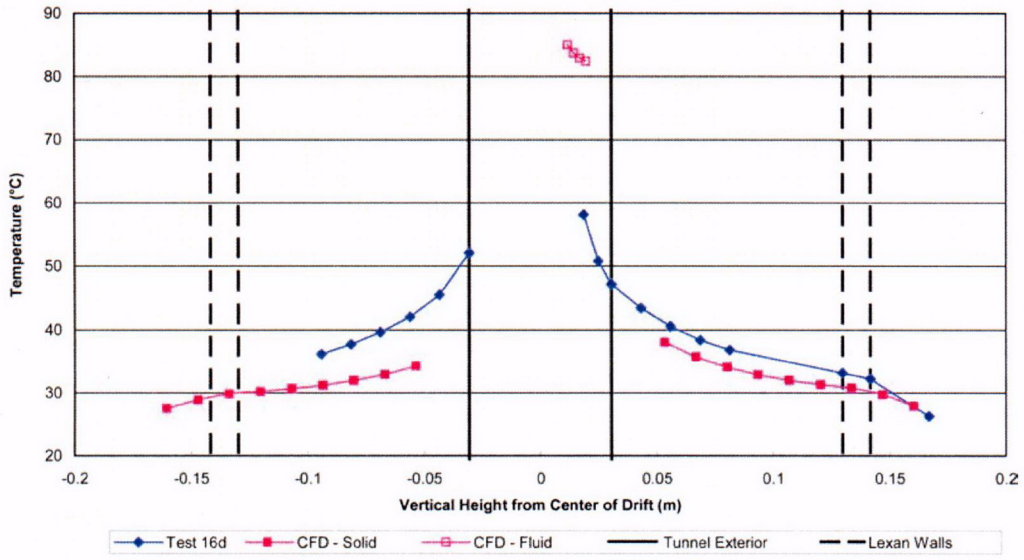

Figure 3-27. Comparison of the Computational Fluid Dynamics and Measured Temperatures of Test #16d at x-location of 0.267 m [0.876 ft] (~ Center of Heater). Heater Power was 3.37 W [11.5 BTU/h]. [°F = 1.8 × T °C + 32]

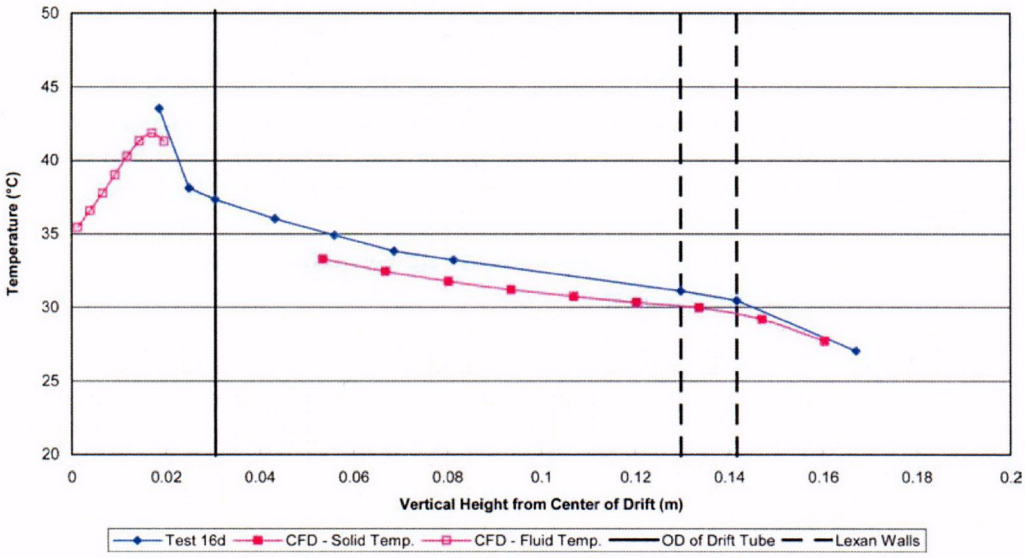

Figure 3-28. Comparison of the Computational Fluid Dynamics and Measured Temperatures of Test #16d at a Power Level of 3.37 W [11.5 BTU/h] and an x-location of 0.165 m [0.541 ft], Midway Between Heater and the Mid-Plane of the Drift. [°F = 1.8 × T °C + 32]

C-19

the temperature gradient of the air along the drift is significantly higher for the simulated than for the measured results.

- The computational fluid dynamics air temperatures at the two locations away from the heater for the wet tests (see Figures 3-23 and 3-24) show the same basic trend, with the hotter fluid at the top of the drift and the cooler fluid at the bottom of the drift.

- The temperatures in the solid materials surrounding the drift matched fairly well for both the wet and dry tests (See Figures 3-25 to 3-28). The most notable discrepancy was that the measured solid temperatures directly below the heater were hotter than those in the solid material above the drift, while the computational fluid dynamics results showed the opposite trend with the solid material below the heater cooler than the material above.

- There is a temperature discrepancy between results for Test #11 and #14 (see Figures 3-24, 3-25, and 3-26). Noting that the temperatures increased significantly for the dry test, it may be reasonable to assume that the discrepancy may be a result of slightly different water saturations in the sand.

Possible causes for differences between the computational fluid dynamics and measured results:

- Latent heat of vaporization assumption: For the wet tests, the lack of latent heat in the model helps explain the reason that the simulated air temperatures above the heater were so much greater than the measured values. This also may explain the higher simulated temperature gradient in the fluid along the drift. The heat transported along with the moisture in the drift caused the temperatures away from the heater to be higher, lowering the temperature gradient. This latent-heat effect does not explain, however, why the simulated temperatures in the dry test (with no latent heat) were much hotter above the heater than the measured results.

- Boundary Conditions: The boundary conditions in the computational fluid dynamics model were set at a constant temperature of 300 K (27 °C) for all six sides including the cold plate. The tests were conducted with a cold plate temperature of 20 °C [68 °F]. Also, the bottom of the experimental apparatus was set on a piece of Styrofoam insulation on a table in the laboratory. The extra insulation on the bottom of the experiment may account for the greater measured temperatures in the sand below the heater. The differences in the cold-wall temperatures may partially account for higher simulated air temperatures at the heater, but it does not explain why the air temperature gradient in the fluid along the drift is higher in the computational fluid dynamics model.

- Thermal conductivity of the solid materials: Accurate thermal conductivities for many of the materials in the model were difficult to obtain. In particular, the published values for dry sand and calculated values for saturated sand did not adequately match the thermal gradients in the computational fluid dynamics model. A uniform value for effective thermal conductivity of the sand was used in the simulations. The values of thermal conductivity for both dry and wet sand used in the computational fluid dynamics model were calibrated using the dry and wet test data to more closely match the computational fluid dynamics results. One possible cause for this discrepancy was that thermal buoyancy in the water created a convection effect that significantly raised the effective thermal conductivity. This effect was modeled by simply raising the thermal conductivity

of the sand throughout the model. In reality, the sand below the heater, with the heat being conducted from above, would not see this effect because it is thermally stable. If this convection hypothesis is true, sand below the heater should have a lower effective conductivity than sand above the drift. Possibly offsetting the effect of convection in the sand is the uncertainty of saturation level, especially near the top of the box. If the saturation levels of the sand were considered, the opposite effect to that caused by convection would be expected. The partially saturated sand above the drift should lead to a lower effective thermal conductivity than for the fully saturated sand below the drift. It is not clear, however, if this would offset the effect of convection in the partially saturated sand.

- Heater stand: In the experimental apparatus, the heater was held up off the bottom of the drift with a small piece of ceramic tube. The ceramic tube had a outside diameter smaller than the inside diameter of the drift and an inside diameter larger than the outside diameter of the heater. This geometry created line contacts and small air volumes that were difficult to model with the mesh resolution. The geometry was modeled with a solid material that was mated to both the heater and the drift wall. The line contacts were modeled with interface conductance parameters. It was difficult to estimate what value to use for these convection coefficients. This imprecise modeling of the heater stand had an effect on the predicted amount of heat conducted from the heater directly to the bottom of the drift tube. This may account for some of the discrepancies between the simulated and measured solid temperatures below the heater.

It is difficult to determine the exact cause of the discrepancies between the model and measured results. Further analysis would have to be conducted with a less complex model, with better-known material properties, to properly develop and refine this computational fluid dynamics modeling technique. The results do show that the computational fluid dynamics model does properly model some of the basic temperature trends in the model and should provide reasonable assessment of the cold-trap, vapor-transport process.

4 SUMMARY

Processes that lead to a change in water chemistry and an elevation of relative humidity in drifts when the waste packages are above 80 °C [176 °F] are important to repository performance. The cold-trap process has the potential to supply water to waste package surfaces, which could initiate or enhance localized corrosion and increase saturation in the invert and wallrock to facilitate transport of radionuclides away from the engineered barrier system.

The presence of dust on the waste packages, combined with elevated relative humidity, may lead to an increased potential for localized corrosion. If drip shields are used in the design, one pathway for moisture from the cold-trap process to enter a hot waste package environment is by condensation on the invert outside the drip shield, redistribution, and re-evaporation beneath the drip shield. Another moisture pathway is by axial convection beneath the drip shield bringing air from cooler zones where the wallrock has rewet, or where it was never dried out from the imposed heat load. The details of natural convection in drifts and its effect on moisture redistribution, however, have not been sufficiently studied to assess the effect of the cold-trap process on repository performance.

This report documents the results from a small-scale laboratory cold-trap model and the tools used to simulate the laboratory model. A laboratory model of a drift with a heat source at one end and a heat sink at the other end was used to induce convection and condensation associated with a cold-trap process. The small-scale laboratory model provides support that the cold-trap process will occur. Measurements of condensation along the drift were difficult to make; only measurements of condensate draining from the heat-sink wall were obtained. An analytical solution for airflow and temperature was developed and combined with a simple condensation model to estimate condensation rates along the drift. To address the complex geometry and to better represent the interchange of heat across the drift walls, a computational fluid dynamics model of the experiment was developed. The computational fluid dynamics simulations of temperature and airflow led to estimates of condensate distribution along the drift. A zone was identified where the highest potential condensation occurred based on measured and simulated temperature distribution.

Estimates of environmental conditions in the proposed emplacement drifts at Yucca Mountain were explicitly avoided. The small-scale laboratory model may not adequately represent conditions in emplacement drifts, primarily because of difficulties in thermal scaling. The uncertainty of thermal scaling was discussed extensively and an approach was recommended for using large-scale experiments and numerical models to estimate emplacement drift environmental conditions. The small-scale laboratory experiment was a prototype to assist in the development of a large-scale cold-trap experiment, though some general conclusions from the small-scale experiment are useful.

An important conclusion from the laboratory experiment and associated modeling was that much of the condensation would be expected to occur in the zone of high-temperature gradient near the heat source. Analysis of the fundamental processes suggests that, at some location near the heat source, the moist air will reach a relative humidity of 100 percent, after which condensation can occur. This zone is not expected to be at the end of the drift or in access tunnels, but may be in the vicinity of other waste packages. Difficulties in matching the measured temperatures everywhere in the subscale model mean that quantitative estimates may not be reliable. General patterns, however, are not expected to change if the numerical model is further refined to better

capture the measured distributions. The difficulties may be due to uncertainty of parameter input or due to the lack of inclusion of all important processes.

Three assumptions for the condensation model are worth noting. The first assumption was that air leaving the heater cartridge zone was at 100-percent relative humidity. Initial observations of condensation and dripping from thermocouples, anemometers, and objects dangling from the drift crown downgradient from the heater confirmed that the relative humidity had reached 100 percent. The exact location, however, was not quantitatively known. The further downgradient that the 100-percent relative humidity location occurs, the larger the error in the model used to estimate condensation rate.

The second assumption was that boundary-layer resistance would be negligible. There did not appear to be a boundary-layer resistance to condensation occurring on the heat-sink endwall. A mass balance of energy that accounts for latent-heat, however, suggests that less condensation occurred along the drift than was estimated by the condensation model. The implication is that less evaporation occurred from drift walls near the heater, thus, there is a possibility that boundary-layer resistance inhibited evaporation. Another way of stating this assumption is that the diffusion rate across the boundary layer adjacent to solid objects is less than the convection rate to the boundary layer. Given the dominant direction of airflow, objects protruding into the dominantly axial flow field or rough drift walls may exhibit little boundary-layer resistance to evaporation and condensation.

The third assumption that was made to simplify the model in this initial effort was that the latent heat of vaporization was negligible to the overall heat transfer from the heater to the moist air. The moisture transport analysis results show that this is, in fact, not the case. Including this effect in the work reported here might have resulted in better agreement with the experiment data; however, the conclusion that condensation varies along the drift would not change. It was decided that improving the fidelity of the heat transfer and moisture transport analysis for the laboratory-scale experiment simulation is not warranted at this time.

It is recommended that the effects of boundary-layer resistance and latent-heat transfer be included in future simulations of large-scale experiments and in estimates of the actual field conditions in the waste emplacement drifts. It should be noted that including these effects is not a trivial matter. Two computational fluid dynamics software vendors were approached about methods of modeling the evaporation, transport, and subsequent condensation of water in an enclosure. Modeling of the evaporation and water vapor transport phenomenon are relatively straightforward. Both vendors (FLUENT® and FLOW–3D®) reported that evaporation and transport are either currently handled by their respective codes or could be quickly added.

The condensation phenomenon, however, is not easy to simulate and would require considerable development effort to simulate this process in a robust and accurate way. The technical problem of successfully incorporating this into a general purpose computational fluid dynamics simulation is that when the moist air cools by convection or conduction to below the dewpoint temperature, the water vapor condenses to keep the gas mixture in equilibrium. Unlike evaporation, in which the liquid evaporates from a known location, the generation of liquid from the vapor phase takes place wherever the temperature is less than the dewpoint. The generalization of the mass and heat transfer of phase change and the subsequent transport of liquid through the gas phase and eventual impact with a solid surface will be a challenge. Using the knowledge gained from the desktop laboratory cold-trap experiment, a larger-scale laboratory

experiment is under development. The larger-scale experiment will shed light on thermal scaling issues and will allow for the inclusion of geometrically-scaled waste packages, waste package supports, drip shield, and the invert.

5 REFERENCES

American Society of Heating, Refrigeration, and Air Conditioning Engineers, Inc. "ASHRAE Handbook and Product Directory, 1977 Fundamentals." 3rd Printing. Chapter 5. New York City, New York: American Society of Heating, Refrigeration, and Air Conditioning Engineers, Inc. 1977.

Bechtel SAIC Company, LLC. "FY01 Supplemental Science and Performance Assessment." Vol. 1: Scientific Bases and Analyses. TDR–MGR–MD–000007. Rev. 00 ICN 01. Las Vegas, Nevada: Bechtel SAIC Company, LLC. 2001a.

Bechtel SAIC Company, LLC. "Technical Update Impact Letter Report." MIS–MGR–RL–000001. Rev. 00. Las Vegas, Nevada: Bechtel SAIC Company, LLC. 2001b.

Brossia, C.S., L. Browning, D.S. Dunn, O.C. Moghissi, O. Pensado, and L. Yang. "Effect of Environment on the Corrosion of Waste Package and Drip Shield Materials." CNWRA 2001-003. San Antonio, Texas: CNWRA. 2001

CRWMS M&O. "Multiscale Thermohydrologic Model." ANL–EBS–MD–000049. Rev. 00 ICN 02. Las Vegas, Nevada: CRWMS M&O. 2001

CRWMS M&O. "Near Field Environment Process Model Report." TDR–NBS–MD–000001. Rev. 00 ICN 03. Las Vegas, Nevada: CRWMS M&O. 2000a.

CRWMS M&O. "In-Drift Thermal-Hydrological-Chemical Models." ANL–EBS–MD–000026. Rev. 00 ICN01. Las Vegas, Nevada: CRWMS M&O. 2000b.

Flow Science, Inc. "FLOW–3D User's Manual." Version 8.1.1. Sante Fe, New Mexico: Flow Science, Inc. 2003.

Francis, N.D., S.W. Webb, M.T. Itamura, and D.L. James. "CFD Modeling of Natural Convection Heat Transfer and Fluid Flow in Yucca Mountain Project (YMP) Enclosures." SAND2002–4179. Albuquerque, New Mexico: Sandia National Laboratories. 2003a.

Francis, N.D., M.T. Itamura, S.W. Webb, and D.L. James. "In-Drift Natural Convection Sensitivity Studies for the LTOM Repository Design." Proceedings of the 10th High-Level Waste Management Conference, Las Vegas, Nevada, March 30–April 2, 2003. La Grange Park, Illinois: American Nuclear Society. pp. 691–698. 2003b.

Gute, G.D., G. Ofoegbu, F. Thomassy, S. Hsiung, G. Adams, A. Ghosh, B. Dasgupta, A. Chowdhury, and S. Mohanty. "MECHFAIL: A Total-System Performance Assessment Code Module for Evaluating Engineered Barrier Performance Under Mechanical Loading Conditions." CNWRA 2003-06. San Antonio, Texas: CNWRA. 2003.

Incropera, F.P. and D.P DeWitt. *Fundamentals of Heat and Mass Transfer.* New York City, New York: John Wiley and Sons. 2002.

Jury, W.A., W.R. Gardner, and W.H. Gardner. *Soil Physics.* 5th Edition. New York City, New York: John Wiley and Sons, Inc. 1991.

Kreith, F. and M.S. Bohn. *Principles of Heat Transfer.* 6th Edition. Pacific Grove, California: Brooks/Cole. 2001.

Kuehn, T.H. and R.J. Goldstein. "An Experimental Study of Natural Convection Heat Transfer in Concentric and Eccentric Horizontal Cylindrical Annuli." *Journal of Heat Transfer.* Vol. 100. pp. 635–640. 1978.

Kuehn, T.H. and R.J. Goldstein. "An Experimental and Theoretical Study of Natural Convection in the Annulus Between Horizontal Concentric Cylinders." *Journal of Fluid Mechanics.* Vol. 4, Part 4. pp. 695–719. 1976.

Manepally, C. and R.W. Fedors. "Edge-Cooling Effect on the Potential Thermohydrologic Conditions at Yucca Mountain." Proceedings of the 10th High-Level Waste Management Conference, Las Vegas, Nevada, March 30–April 2, 2003. La Grange Park, Illinois: American Nuclear Society. No page numbers. Published on CD ROM. 2003.

Mohanty, S., R. Codell, J.M. Menchaca, R. Janetzke, M. Smith, P. LaPlante, M. Rahimi, and A. Lozano. "System-Level Performance Assessment of the Proposed Repository at Yucca Mountain Using the TPA Version 4.1 Code." CNWRA 2002-05. San Antonio, Texas: CNWRA. 2002.

Raithby, G.D. and K.G.T. Hollands. "A General Method of Obtaining Approximate Solutions to Laminar and Turbulent Heat Transfer Problems." *Advances in Heat Transfer.* Vol. 11. T.F. Irvine and J.P. Hartnett, eds. New York City, New York: Academic Press. pp. 265–315. 1975.

Sass, J.H., A.H. Lachenbruch, and R.J. Munroe. "Thermal Conductivity of Rocks from Measurements on Fragments and its Application to Heat-Flow Determinations." *Journal of Geophysical Research.* Vol. 76, No. 14. pp. 3,391–3,401. 1971.

Somerton, W.H. "Thermal Properties and Temperature-Related Behavior of Rock Fluid Systems." Amsterdam, Holland: Elsevier. 1992.

Somerton, W.H., A.H. El-Shaarani, and S.M. Mobarak. "High-Temperature Behavior of Rocks Associated with Geothermal-Type Reservoirs." Proceedings of the 44th Annual California Regional Meeting of the Society of Petroleum Engineers. Paper SPE–4897. Richardson, Texas: Society of Petroleum Engineers. 1974.

Wilder, D.G., ed. "Near-Field and Altered Zone Environment Report." UCRL–LR–124998. Livermore, California: Lawrence Livermore National Laboratory. 1996.

APPENDIX A

DEVELOPMENT OF ANALYTICAL SOLUTION FOR AIRFLOW AND ESTIMATES OF CONDENSATION RATE

The development of an analytical solution for airflow was intended to assist in designing and interpreting the small desktop laboratory model cold-trap experiment. The actual cylindrical experiment drift was replaced with a two-dimensional drift. The model problem also replaces the heater cartridge with a uniform hot wall. The object of the analysis is to predict the magnitudes of the overall circulation in the tunnel and the rate at which moisture might be condensed.

The main assumptions used in the *flow* analysis are:

- two-dimensional x,y geometry
- heat Q added at the hot wall and removed at the cold wall
- walls at $y = 0$ and $y = H$ are insulated
- steady flow
- Boussinesq approximation is used to estimate buoyancy effects

Governing Differential Equations

Using the Boussinesq approximation, the governing equations are

$$\frac{\partial u}{\partial x} + \frac{\partial v}{\partial y} = 0$$

$$u\frac{\partial T}{\partial x} + v\frac{\partial T}{\partial y} = \alpha_o\left(\frac{\partial^2 T}{\partial x^2} + \frac{\partial^2 T}{\partial y^2}\right)$$

$$u\frac{\partial u}{\partial x} + v\frac{\partial u}{\partial y} = -\frac{g}{\rho_o}\frac{\partial p}{\partial x} + \nu_o\left(\frac{\partial^2 u}{\partial x^2} + \frac{\partial^2 u}{\partial y^2}\right)$$

$$u\frac{\partial v}{\partial x} + v\frac{\partial v}{\partial y} = -\frac{g}{\rho_o}\frac{\partial p}{\partial y} + \nu_o\left(\frac{\partial^2 v}{\partial x^2} + \frac{\partial^2 v}{\partial y^2}\right) - g\left[1 - \beta_o(T - T_o)\right]$$

where x and y are the horizontal and vertical coordinates, u and v are the horizontal and vertical components of the velocity at location (x,y), T is the temperature at location (x,y), T_o is the reference temperature, g is the gravitational constant, p is the pressure at location (x,y), ρ_o is the density at the reference temperature, ν_o is the kinematic viscosity of air at the reference temperature, β_o is the thermal expansion coefficient of air at the reference temperature, α_o is the thermal diffusivity of air at the reference temperature equal to $k_o/\rho_o C_{po}$, k_o is the thermal conductivity of air at the reference temperature, C_{po} is the specific heat of air at the reference temperature.

The pressure variable can be eliminated by taking the derivative of the derivative of y of the conservation of momentum for the x-direction, and the derivative of x of the conservation of momentum for the y-direction. Combining these two derivative equations leads to

$$\frac{\partial}{\partial x}\left(u\frac{\partial v}{\partial x}+v\frac{\partial v}{\partial y}\right)-\frac{\partial}{\partial y}\left(u\frac{\partial u}{\partial x}+v\frac{\partial u}{\partial y}\right)=\nu_o\left[\frac{\partial}{\partial x}\left(\frac{\partial^2 v}{\partial x^2}+\frac{\partial^2 v}{\partial y^2}\right)-\frac{\partial}{\partial y}\left(\frac{\partial^2 u}{\partial x^2}+\frac{\partial^2 u}{\partial y^2}\right)\right]+g\beta_o\frac{\partial T}{\partial x}$$

The equations of motion are made nondimensional using the following scheme:

$X = x/L$ and $Y = y/H$ nondimensional coordinates

$U = u\left(\nu_o L\right)\left(g\beta_o H^3 \Delta T_o\right)^{-1}$ nondimensional velocity in x-direction

$V = v\left(\nu_o L^2\right)\left(g\beta_o H^4 \Delta T_o\right)^{-1}$ nondimensional velocity in y-direction

$\theta = \left(T - T_c\right)/\Delta T_o$ nondimensional temperature

where H is the height of the drift, L is the length of the drift, ΔT_o is temperature difference between hot and cold walls, and T_c is the temperature of the cold wall (at $x = 0$).

Other symbols that will be used subsequently are defined as

Pr	=	Prandtl number, ν_o / α_o
Q	=	heat input at hot wall (per unit width of the drift)
Ra	=	Rayleigh number, $g\,\beta_o H^3 \Delta T_o / (\alpha_o \nu_o)$

With these definitions and nondimensional variables, we expect that the nondimensional variables will have a maximum value of one and a minimum of zero:

$0 <= x <= 1$ $0 <= y <= 1$ $0 <= |U| <= 1$ $0 <= |V| <= 1$ $0 <= |\theta| <= 1$

The circulatory flow within the two-dimensional drift is governed by the following differential equations, which express the conservation of mass, momentum, and energy requirements written now in nondimensional variables:

conservation of mass

$$\frac{\partial U}{\partial X}+\frac{\partial V}{\partial Y}=0$$

combined *x* and *y* conservation of momentum

$$\left(\frac{H}{L}\right)^4\left(\frac{Ra}{Pr}\right)\left[\frac{\partial}{\partial X}\left(U\frac{\partial U}{\partial X}+V\frac{\partial U}{\partial Y}\right)\right]-\left(\frac{H}{L}\right)^2\left(\frac{Ra}{Pr}\right)\left[\frac{\partial}{\partial Y}\left(U\frac{\partial V}{\partial X}+V\frac{\partial V}{\partial Y}\right)\right]$$

$$=\frac{\partial\theta}{\partial X}-\frac{\partial^3 U}{\partial Y^3}+\left(\frac{H}{L}\right)^2\left[\frac{\partial}{\partial Y}\left(U\frac{\partial^2 V}{\partial XY}+V\frac{\partial^2 U}{\partial X^2}\right)\right]+\left(\frac{H}{L}\right)^4\frac{\partial^3 V}{\partial X^3}$$

conservation of energy

$$Ra\left(\frac{H}{L}\right)^2\left(U\frac{\partial\theta}{\partial X}+V\frac{\partial\theta}{\partial Y}\right)=\left(\frac{H}{L}\right)^2\frac{\partial^2\theta}{\partial X^2}+\frac{\partial^2\theta}{\partial Y^2}$$

The boundary conditions for these differential equations are expressed as

$U = V = 0$ for $X = 0$ and $X = 1$, and for $Y = 0$ and $Y = 1$ ("no slip")

$$\frac{\partial\theta}{\partial Y} = 0 \quad \text{for} \quad Y = 0 \quad \text{and} \quad Y = 1 \quad \text{(insulated walls)}$$

$\theta = 0$ for $X = 0$
$\theta = 1$ for $X = 1$

Considering the form of these equations and the fact that $(H/L)^2 << 1$, it is natural to find a solution expressed in powers of $(H/L)^2$ since higher order terms can be neglected. Thus, we assume

$$U = U_o + \left(\frac{H}{L}\right)^2 U_1 + \left(\frac{H}{L}\right)^4 U_2 + \ldots$$

$$V = V_o + \left(\frac{H}{L}\right)^2 V_1 + \left(\frac{H}{L}\right)^4 V_2 + \ldots$$

$$\theta = \theta_o + \left(\frac{H}{L}\right)^2 \theta_1 + \left(\frac{H}{L}\right)^4 \theta_2 + \ldots$$

These expressions are substituted into the differential equations for mass, momentum, and energy conservation given above. The terms are collected in powers of the parameter $(H/L)^2$. Since $(H/L)^2$ in principle can have any value, it is necessary that the expressions multiplied by the various powers of $(H/L)^2$ must each be satisfied individually. This process gives the following set of differential equations:

Zeroth order $(H/L)^0$ equations

$$\frac{\partial U_o}{\partial X} + \frac{\partial V_o}{\partial Y} = 0$$

$$\frac{\partial \theta_o}{\partial X} - \frac{\partial^3 U_o}{\partial Y^3} = 0$$

$$\frac{\partial^2 \theta_o}{\partial Y^2} = 0$$

First order $(H/L)^2$ equations

$$\frac{\partial U_1}{\partial X} + \frac{\partial V_1}{\partial Y} = 0$$

$$-\frac{Ra}{Pr}\left[\frac{\partial}{\partial Y}\left(U_o \frac{\partial U_o}{\partial X} + V_o \frac{\partial U_o}{\partial Y}\right)\right] = \frac{\partial \theta_1}{\partial X} - \frac{\partial^3 U_1}{\partial Y^3} + \frac{\partial^3 V_o}{\partial X \partial Y^2} - \frac{\partial^3 U_o}{\partial Y \partial X^2}$$

$$Ra\left(U_o \frac{\partial \theta_o}{\partial X} + V_o \frac{\partial \theta_o}{\partial Y}\right) = \frac{\partial^2 \theta_o}{\partial X^2} + \frac{\partial^2 \theta_1}{\partial Y^2}$$

Second order $(H/L)^4$ equations

$$\frac{\partial U_2}{\partial X} + \frac{\partial V_2}{\partial Y} = 0$$

$$\frac{Ra}{Pr}\left[\frac{\partial}{\partial X}\left(U_o \frac{\partial U_o}{\partial X} + V_o \frac{\partial U_o}{\partial Y}\right)\right] - \frac{Ra}{Pr}\left[U_o \frac{\partial U_1}{\partial X} + V_o \frac{\partial U_1}{\partial Y} + U_1 \frac{\partial U_o}{\partial X} + V_1 \frac{\partial U_o}{\partial Y}\right] =$$

$$\frac{\partial \theta_2}{\partial X} - \frac{\partial^3 U_2}{\partial Y^3} + \frac{\partial^3 V_1}{\partial X \partial Y^2} - \frac{\partial^3 U_1}{\partial X \partial Y^2} + \frac{\partial^3 V_o}{\partial X^3}$$

$$Ra\left(U_o \frac{\partial \theta_1}{\partial X} + V_o \frac{\partial \theta_1}{\partial Y} + U_1 \frac{\partial \theta_o}{\partial X} + V_1 \frac{\partial \theta_o}{\partial Y}\right) = \frac{\partial^2 \theta_2}{\partial Y^2} + \frac{\partial^2 \theta_1}{\partial X^2}$$

The third- and higher-order equations are similar to the second-order equations.

Solution to Differential Equations for the Core Flow

The solution of the differential equations correct through the first-order terms is

$$U = \frac{1}{6} \cdot K_1 \cdot \left(Y^3 - \frac{3}{2} \cdot Y^2 + \frac{1}{2} \cdot Y \right)$$

$$V = 0$$

$$\theta = K_2 + K_1 \cdot X + \frac{1}{120} \cdot RaK_1^2 \cdot \left(\frac{H}{L} \right)^2 \cdot \left(Y^5 - \frac{5}{2} \cdot Y^4 + \frac{5}{3} \cdot Y^3 \right)$$

where K_1 and K_2 are integration constants to be determined.

These equations represent the core flow away from the $X = 0$ and $X = 1$ ends of the drift. Note that U is not identically zero at $X = 0$ and $X = 1$ as the boundary conditions require. However, the average value of U across the drift height is zero, so the $X = 0$ and $X = 1$ boundary conditions are satisfied in an average sense. Similarly, the temperature θ is not constant at either the hot end or the cold end. The way the solutions are corrected to meet the boundary more exactly is described later, but first, an expression for heat flow is needed.

Heat Flow from Hot End to Cold End of Channel

The net heat flow from the hot end of the drift to the cold end is a combination of conduction through the air and the energy carried by the flow. It is given by the following integral. Note that the integral does not depend on position X in the channel.

$$Q = \int_0^H \left(k_o \frac{\partial T}{\partial X} - \rho_o C_{po} u T \right) dy$$

Carrying out the integration gives

$$Q = k_o \cdot \Delta T_o \cdot \left(\frac{H}{L} \right) \cdot \left[K_1 + \frac{K_1^3}{362880} \cdot \left(\frac{H}{L} \cdot Ra \right)^2 \right]$$

Evaluation of Integration Constants to Meet Boundary Conditions

A simple way to evaluate K_1 and K_2 is to set the average value of θ equal to 0 at $X = 0$ and equal to 1 at $X = 1$. This procedure gives $K_1 = 1$ and $K_2 = 0$. This satisfies the boundary conditions at $X = 0$ and $X = 1$ only in an average sense. Better yet, the previous expressions can be corrected by including the equations for higher powers of $(H/L)^2$ or we can consider the end wall effects separately by a boundary-layer approach. The boundary-layer approach is selected because it

converges more quickly. Furthermore, an integral formulation is used. The boundary-layer thickness at the end walls is denoted by δ. From symmetry, δ is the same on the cold wall and the hot wall. Thus, we will impose symmetry about the center of the drift and consider just the cold wall. The end conditions are denoted by the subscript "*e*."

The symmetry condition of $\theta = 0.5$ for $X = 0.5$, $Y = 0.5$ requires that

$$K_2 + \frac{1}{2}K_1 + Ra\left(\frac{H}{L}\right)^2 \frac{K_1}{1440} = \frac{1}{2}$$

The boundary conditions at the cold wall are: (i) all velocities be zero, and (ii) the temperature be constant and equal to the cold-wall temperature. These conditions require that

$$U_e = V_e = \theta_e = 0 \qquad \frac{\partial \theta_e}{\partial Y} = 0 \qquad \text{at} \quad X = 0$$

There are also conditions required to match the boundary layer to the core flow at the edge of the boundary layer and to make the boundary-layer flow merge smoothly with the core flow; these conditions are expressed as

$$U_e = U \qquad V_e = V = 0 \qquad \theta_e = \theta \qquad \text{at} \quad X = \delta$$

$$\frac{\partial U_e}{\partial X} = \frac{\partial U}{\partial X} \qquad \frac{\partial V_e}{\partial X} = \frac{\partial V}{\partial X} = 0 \qquad \frac{\partial \theta_e}{\partial X} = \frac{\partial \theta}{\partial X} \qquad \text{at} \quad X = \delta$$

For an integral solution, physically reasonable functions are assumed for the velocities and temperature, which are then made to satisfy the governing equations in an integral sense. The unknown in these functions is the boundary layer thickness, δ.

Suitable functional forms for the velocities and temperature that satisfy all the above boundary conditions are

$$U_e = K_1\left(Y^3 - \frac{3}{2}Y^2 + \frac{1}{2}Y\right)\left(\frac{X}{\delta}\right)^2\left[1 - \frac{4}{3}\left(\frac{X}{\delta}\right) + \frac{1}{2}\left(\frac{X}{\delta}\right)^2\right]$$

$$V_e = \frac{K_1}{2\delta}\left(Y^4 - 2Y^3 + Y^2\right)\left(\frac{X}{\delta}\right)\left(1 - \frac{X}{\delta}\right)^2$$

$$\theta_e = \left[K_2 + K_1 X + \frac{Ra}{120}K_1^2\left(\frac{H}{L}\right)^2\left(Y^5 - \frac{5}{2}Y^4 + \frac{5}{3}Y^3\right)\right]\left(\frac{X}{\delta}\right)\left(2 - \frac{X}{\delta}\right)$$

Furthermore, the expressions for U_e and V_e satisfy the conservation of mass differential equation. Thus, only the conservation of momentum and conservation of energy equations remain to be satisfied. These equations are put into an integral form by integrating them across the boundary layer thickness. The result, for example, for the conservation of energy differential equation is

$$Ra\left(\frac{H}{L}\right)\int_0^{\delta}\int_0^{1} U_e \frac{\partial \theta_e}{\partial X} dXdY + Ra\left(\frac{H}{L}\right)^2 \int_0^{\delta}\int_0^{1} V_e \frac{\partial \theta_e}{\partial Y} dXdY = \int_0^{\delta}\int_0^{1}\left[\left(\frac{H}{L}\right)^2 \frac{\partial^2 \theta_e}{\partial X^2} + \frac{\partial^2 \theta_e}{\partial Y^2}\right] dXdY$$

Some of the integrations can be done by parts to give the final result

$$Ra\int_0^{1} U_e \theta_e\big|_{X=\delta} dY = K_1 - \int_0^{1} \frac{\partial \theta_e}{\partial Y}\bigg|_{X=\delta} dY$$

Similarly, the conservation of momentum integral reduces to

$$\int_0^{1} \theta_e\big|_{X=\delta} dY - \int_0^{\delta} \frac{\partial^2 U_e}{\partial Y^2}\bigg|_{Y=0}^{Y=1} dX - \left(\frac{H}{L}\right)^4 \int_0^{1} \frac{\partial^2 V_e}{\partial X^2}\bigg|_{X=0}^{X=\delta} dY = 0$$

By substituting in the previous functional expressions and performing the integrations, the following two equations are derived that relate the unknown parameters:

$$\frac{2}{5}\left(\frac{H}{L}K_1\right)\left[\frac{1}{4} - (\delta')^4\right] = \left[k_2 + \frac{Ra}{1440}\left(\frac{H}{L}K_1\right)^2\right](\delta')^3$$

$$\frac{Ra^2}{725{,}760}\left(\frac{H}{L}K_1\right)^3 \delta' = K_2 + \frac{Ra}{1440}\left(\frac{H}{L}K_1\right)^2$$

where $\delta' = \delta(L/H)$ is a scaled boundary-layer thickness that is more convenient for numerical work since it is not as small as δ.

These two expressions and the previous expression for the symmetry condition are sufficient to determine the three unknowns: K_1, K_2, and δ'.

Numerical Approach and Sample Calculation

Unknown coefficients were calculated using MathCad 2000. Input values for drift dimensions, air properties, and desired temperature difference from the hot end to the cold end of the drift (properties are evaluated at about 60 °C) are listed in Table A–1.

Table A–1. Inputs for Airflow		
Air viscosity	ν_o	0.191 cm^2/s
Air diffusivity	α_o	0.268 cm^2/s
Air conductivity	k_o	0.000283 W/cm K
Drift height	H	5 cm
Drift length	L	61 cm
Cold wall temperature	T_c	295 °K
Temperature difference	ΔT	32 °K
Gravity	g	9.80 m/s^2
Gas constant	R	41.65 cm^3 psi/g °K
Air expansion coefficient, calculated	$\beta_o = 1/(T_c + \Delta T)$	3.058×10^{-3} 1/°K
Raleigh number, calculated	Ra	2.342×10^5

Equations are solved by inputting guesses for unknowns K_1, K_2, and δ' and then finding the solution. Solve symmetry condition

$$K_2 + 0.5 \cdot K_1 + \left(\frac{H}{L} \cdot K_1\right)^2 \cdot \frac{Ra}{1440} = 0.5$$

conservation of energy

$$0.4 \cdot \left(\frac{H}{L} \cdot K_1\right) \cdot \left(0.25 - (\delta')^4\right) = {\delta_x}^3 \cdot K_2 + \left[\left(\frac{H}{L} \cdot K_1\right)^2 \cdot \frac{Ra}{1440}\right]$$

conservation of momentum

$$\left(\frac{H}{L} \cdot K_1\right)^3 \cdot \frac{Ra \cdot \delta_x}{725760} = K_2 + \left(\frac{H}{L} \cdot K_1\right)^2 \cdot \frac{Ra}{1440}$$

Core Flow and Temperature

Velocity and temperature (nondimensional) distributions in the core region are shown in Figure A–1.

Peak velocity of core flow in the X-direction (nondimensional), i.e., velocity in upper half of the drift is from the hot end to the cold end, and in the reverse direction for the lower half, is

$$u_{max} = 0.0016\left(\frac{g \cdot \beta_o \cdot H^3 \cdot \Delta T_o}{\nu_o \cdot L}\right) = 0.016\frac{m}{s}$$

Flow and Temperature in the End-Wall Region

The end-wall X and Y velocities are described by the following equation and illustrated in Figure A–2a:

$$U_e = K_1 \cdot \left(Y^3 - \frac{3}{2} \cdot Y^2 + \frac{1}{2} \cdot Y\right) \cdot \left(\frac{X}{\delta'}\right)^2 \cdot \left[1 - \frac{4}{3} \cdot \left(\frac{X}{\delta'}\right) + \frac{1}{2}\left(\frac{X}{\delta'}\right)^2\right]$$

$$V_e = \frac{K_1}{2 \cdot \delta'} \cdot \left(\frac{X}{\delta'}\right) \cdot \left(1 - \frac{X}{\delta'}\right)^2 \cdot \left(Y^4 - 2 \cdot Y^3 + Y^2\right)$$

The end-wall temperature distribution is described by the following equation and illustrated in Figure A–2b:

$$\theta_e = \left(\frac{X}{\delta'}\right) \cdot \left(2 - \frac{X}{\delta'}\right) \cdot \theta$$

Moisture Transport

The moisture transport is computed using the following observations and assumptions.

- The flow from the hot end to the cold end carries wetter air to the cold end.
- The reverse flow from the cold end to the hot end carries drier air back to the hot end.
- The air has a 100 percent relative humidity at the hot end. When the air gets to the cold end, it will be supersaturated and some moisture will condense on the target. The air will still have a 100 percent relative humidity, but because it is colder, the actual mass of water in the air will be less.
- The airflow from one end to the other is equal to the average density of the air times the average velocity in either the upper (hot to cold) or lower (cold to hot) half of the tube.
- Same airflow rate occurs in the circular channel as in the two-dimensional channel.

Inputs and calculations results for the sample problem are found in Table A–2. An estimate of 5.5 g/h of water was calculated for the sample problem for the entire length of the drift.

Instead of assuming that the entire amount of condensate occurs at the cold end, a distribution along the drift can be estimated by discretizing the moisture algorithm. To obtain estimates of the distribution of condensation along the drift, temperature and integrated velocity values can be calculated for a set of axial positions. Then, the condensation rate for each section of the drift can be estimated. Where temperature and axial velocity values change rapidly, a finer discretization can be used. The results in Section 3.3 utilized the discretized approach.

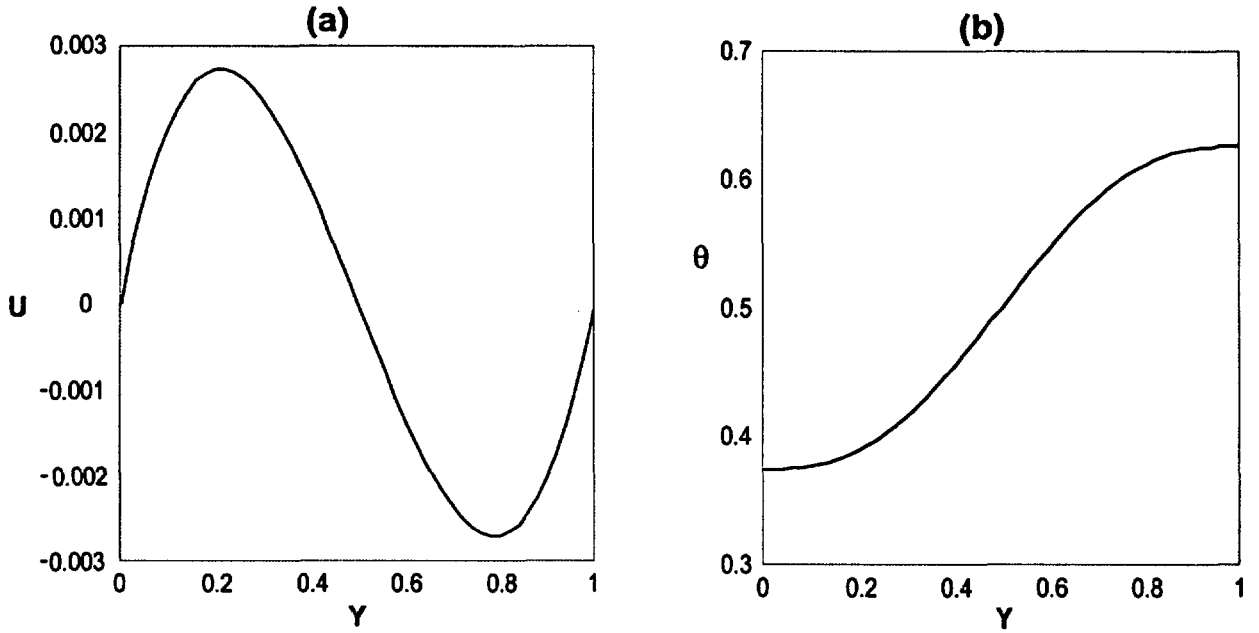

Figure A–1. Nondimensional *X*-Velocity (a) in the Core Region as a Function of Vertical Position, and Similarly Nondimensional Temperature Distribution (b) at $X = 0.5$

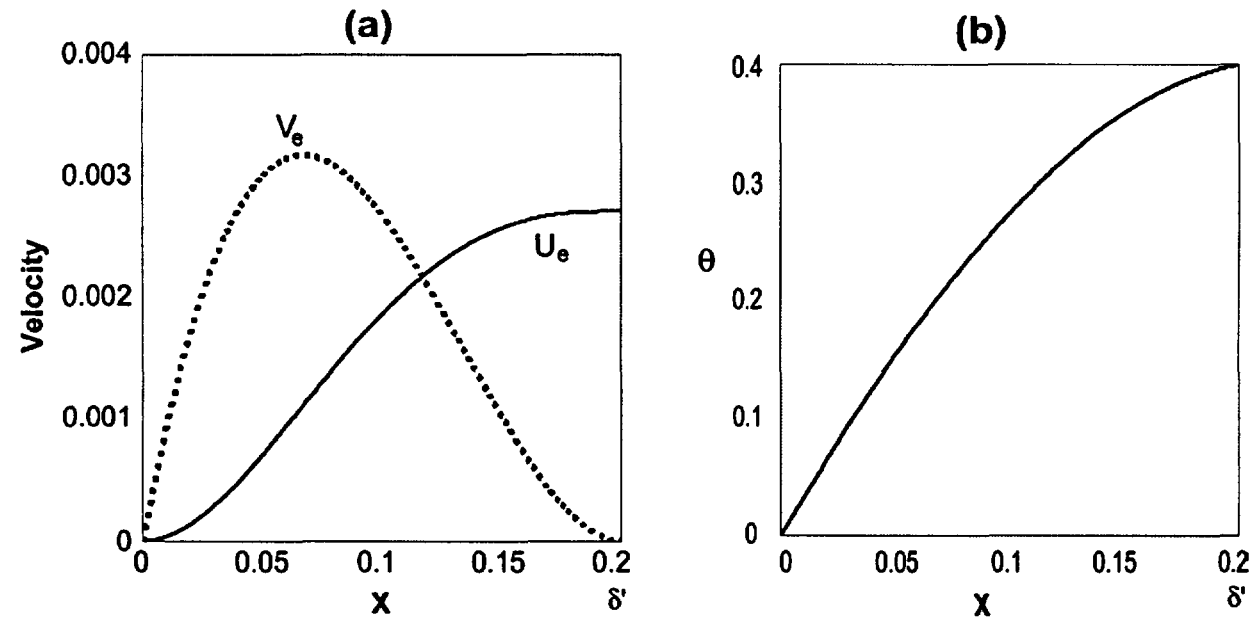

Figure A–2. Plot of Velocities (a) in the End-Wall Region $0 < X < \delta'$ at the *Y* Elevation That Corresponds to the Peak Core Flow Velocity. Note That the *X* Velocity Blends Smoothly to the Core Velocity for $X = \delta'$ and the *V* Velocity Decreases to Zero at $X = \delta'$. Plot of End-Wall Temperature (b) for $Y = 0.5$. Note That the Temperature Gradually Increases from Its Value at $X = \delta'$ to a Value of 0.5 at $X = 0.5$, for This Value of $Y = 0.5$.

Table A–2. Inputs and Calculations for Estimating Condensation Rate. See also, Table A–1.			
Parameter	**Symbol**	**Value or Equation**	**Values**
Calculation of constants	K_1, K_2, δ'	$K_1 = 0.339$, $K_2 = 0.204$, $\delta' = 0.203$	–
Relative humidity	RH	–	1
Partial pressure of air in the air-moisture mixture	P_o	–	14.7 psi
Pressure of saturated air as a function of temperature	$PV(T)$	$PV(T) := C \cdot e^{A\cdot\left(\frac{9}{5}T - B\right)}$	A = 0.0259 °K^{-1} B = 460 K C = 0.075 psi
Absolute humidity of air, gram of moisture per gram of dry air	$\omega(T)$	$\omega(T) := \omega_o \cdot \frac{PV(T)}{P(T)} \cdot RH$	ω_o = 0.622 g/g
Density of air	ρ	$\rho(T, \Delta T) := \frac{(P(T + \Delta T) + P(T))}{(2 \cdot T + \Delta T) \cdot R}$	–
Reference mass flow rate		$U_c(\Delta T) := \frac{g \cdot \beta_o \cdot H^3 \cdot \Delta T}{6 \cdot \nu_o \cdot L}$	–
Average velocity in the hot or cold half of the drift (by integrating the core velocity distribution)		$U_{ave}(\Delta T) := \frac{1}{32} \cdot U_c(\Delta T) \cdot K_1$	1.18190 cm/s
Mass flow rate of air in the upper or lower half of the drift		$m_{air}(T, \Delta T) := \rho(T, \Delta T) \cdot U_{ave}(\Delta T) \cdot \frac{\pi}{4} \cdot \frac{H^2}{2}$	0.018 g/s
Amount of moisture condensed on the target is the difference in the absolute humidities at the hot and cold ends of the drift times the flow rate of dry air		$m_{cond}(T, \Delta T) := m_{air}(T, \Delta T) \cdot (\omega(T + \Delta T) - \omega(T))$	1.533 × 10^{-3} g/s
Amount of moisture condensed per hour for the entire drift		$M := 3600 \cdot s \cdot m_{cond}(T_c, \Delta T_o)$	5.518 g/hr

APPENDIX B

Notes:
1. All dimensions in meters unless otherwise specified.
2. HTC□B is the heat transfer coefficient (W/m^2/K) at the interface between obstacles. If not specified, there is no thermal contact resistance at interface.
3. Tb is the specified constant boundary temperature.

	□BJECT	MATERIAL
	Ceramic Tube	Alumina Ceramic
	Lexan Enclosure	Lexan
	Cold Wall	Lexan
	□uter Insulation	Fiber Frax
	Heater Cartridge	Commercial Heater
	Heater Stand	Alumina Ceramic
	Tube Support	Lexan
	Sand	Dry Sand or Wet Sand

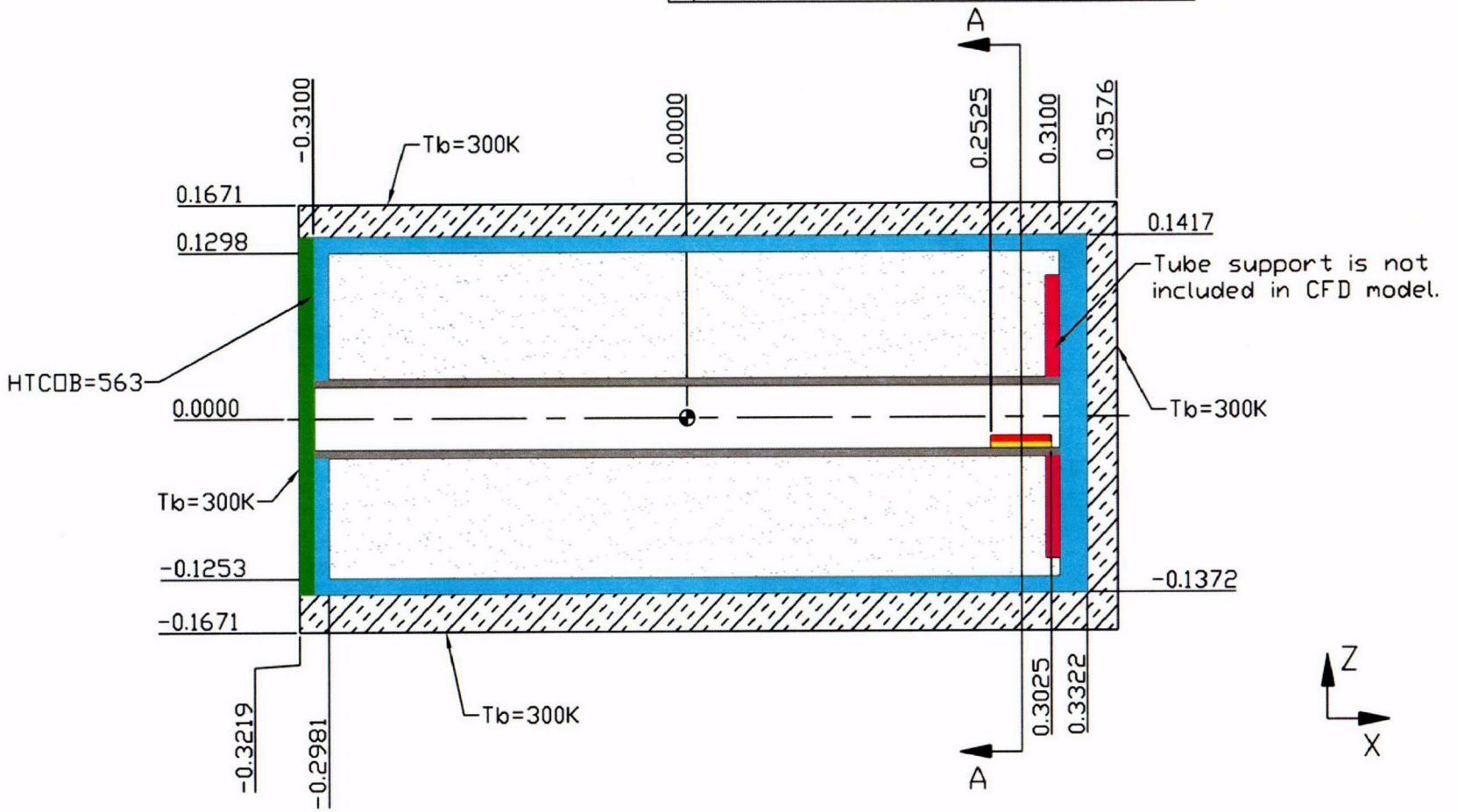

B-1

C-20

Notes:
1. All dimensions in meters unless otherwise specified.
2. HTCOB is the heat transfer coefficient (W/m^2/K) at the interface between obstacles. If not specified, there is no thermal contact resistance at interface.
3. Tb is the specified constant boundary temperature.

OBJECT	THERMAL CONDUCTIVITY
Ceramic Tube	3.4 W/m/K
Lexan Enclosure	0.19 W/m/K
Cold Wall	0.19 W/m/K
Outer Insulation	0.035 W/m/K
Heater Cartridge	10.0 W/m/K
Heater Stand	6.8 W/m/K
Tube Support	0.19 W/m/K
Sand	Dry= 0.22 W/m/K or Wet=1.76 W/m/K

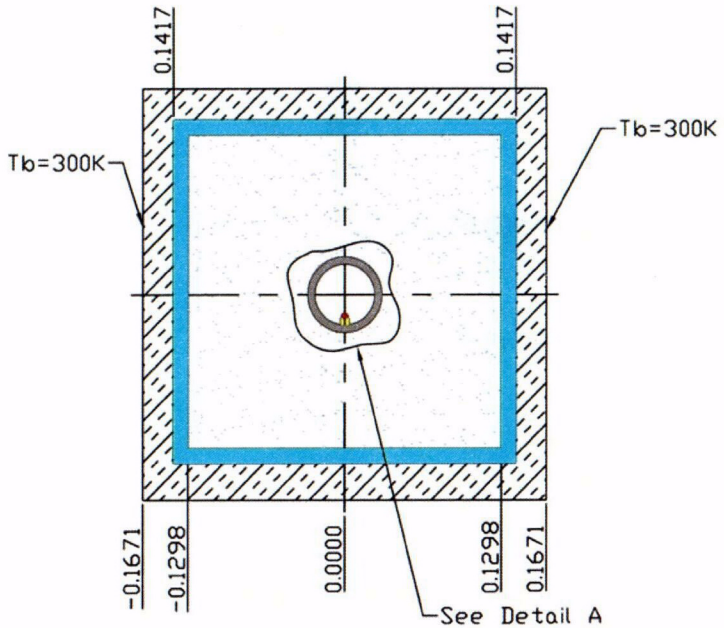

VIEW A-A

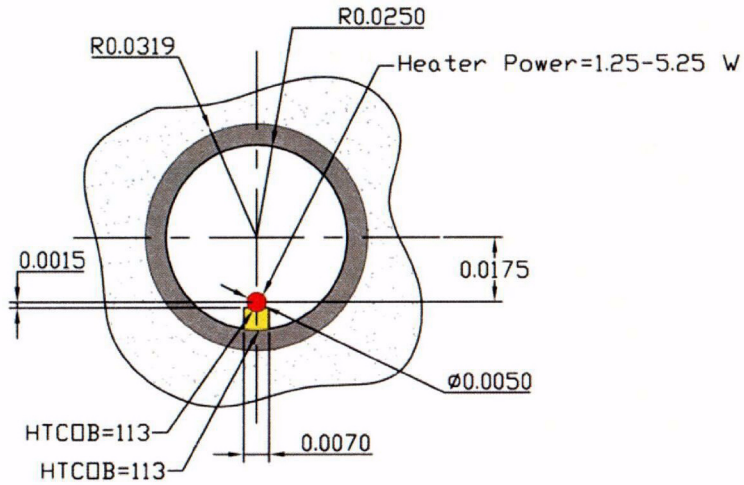

Detail A (Scale 3:1)

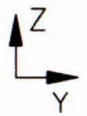

B-2

C-21

APPENDIX C

Table C–1. Thermocouple locations and Steady State Temperature Values for Test #11 [3.4129 W = 1 BTu; 2.54 cm = 1 in; (°C x 5/9) 2 = °F]						
Start Time: 6/17/02 13:52 End Time: 7/29/02 5:25			Elapsed Time (hrs)	457.58	735.37	925.53
			Power Setting	20	25	12
			Watts	3.37	5.251	1.246
X (cm)	Y (cm)	Z (cm)	Thermocouple	Temperature °C	Temperature °C	Temperature °C
27.92	-1.905	-0.675	1	41.1781	51.84537	33.05496
27.92	0	-0.675	2	46.29116	62.28556	35.1638
27.92	1.905	-0.675	3	39.64968	47.96846	32.40895
27.92	-0.635	0.595	4	47.86348	63.50646	35.52465
27.92	0.635	0.595	5	42.75806	50.35131	34.37265
27.92	-1.27	1.23	6	44.62497	59.77575	34.23965
27.92	0	1.23	7	46.21467	61.5268	34.0168
27.92	1.27	1.23	8	44.48262	53.75829	34.81575
27.92	-0.635	2.1825	9	43.52301	57.29099	32.57877
27.92	0.635	2.1825	10	42.02228	54.16846	32.09471
24.11	-1.905	-0.675	11	33.35506	38.30071	29.87211
24.11	0	-0.675	12	51.95407	67.92826	37.65773
24.11	1.905	-0.675	13	37.88166	44.77739	32.16328
24.11	-0.635	0.595	14	43.90245	54.89777	34.75159
24.11	0.635	0.595	15	42.78068	53.37944	33.88207
24.11	-1.27	1.23	16	40.95464	50.80732	33.00101
24.11	0	1.23	17	38.43228	47.16297	31.67129
24.11	1.27	1.23	18	40.47603	49.84657	32.79505
24.11	-0.635	2.1825	19	40.45761	50.06663	32.61442
24.11	0.635	2.1825	20	36.94755	45.4008	30.66127
20.3	-1.905	0.595	21	33.05038	38.35341	29.3739
20.3	0	0.595	22	33.71485	40.19595	29.37975
20.3	1.905	0.595	23	33.13459	39.02233	29.20809
20.3	-0.635	1.865	24	34.97042	42.71809	29.701
20.3	0.635	1.865	25	33.93431	40.86665	29.31777
20.3	0	2.1825	26	31.1022	35.74501	28.39556
16.49	0	-2.2625	27	29.80112	33.28619	27.9277
16.49	-0.635	-1.945	28	29.54628	32.83951	27.86158
16.49	0.635	-1.945	29	29.70615	33.05983	27.91271
16.49	-1.905	-0.675	30	29.8512	33.41199	27.94959
16.49	0	-0.675	31	31.0097	35.49188	28.34391
16.49	1.905	-0.675	32	29.84045	33.31157	27.97177
16.49	-0.635	0.595	33	31.49035	36.68591	28.35841
16.49	0.635	0.595	34	31.58237	36.97579	28.34813
16.49	-1.27	1.23	35	32.00455	37.76794	28.46032
16.49	0	1.23	36	31.60984	37.16975	28.33718
16.49	1.27	1.23	37	31.54921	37.00302	28.29816
16.49	-0.635	2.1825	38	31.5992	37.43888	28.28911
16.49	0.635	2.1825	39	30.29643	34.58441	27.99962
12.68	-1.905	0.595	40	30.4255	34.80655	27.96998
12.68	0	0.595	41	30.27691	34.69159	27.91562
12.68	1.905	0.595	42	30.13252	34.33663	27.8647
12.68	-0.635	1.865	43	29.90216	34.14224	27.77461
12.68	0.635	1.865	44	29.89643	34.14446	27.79501
12.68	0	2.1825	45	29.51625	33.16158	27.71317

Table C–1. Thermocouple locations and Steady State Temperature Values for Test #11 [3.4129 W = 1 BTu; 2.54 cm = 1 in; (°C x 5/9) 2 = °F] (continued)						
Start Time: 6/17/02 13:52 End Time: 7/29/02 5:25			Elapsed Time (hrs)	457.58	735.37	925.53
			Power Setting	20	25	12
			Watts	3.37	5.251	1.246
X (cm)	Y (cm)	Z (cm)	Thermocouple	Temperature °C	Temperature °C	Temperature °C
6.33	-0.635	-2.2625	46	28.67588	31.51936	27.38302
6.33	0.635	-2.2625	47	28.6173	31.49888	27.32738
6.33	-1.27	-1.31	48	28.56409	31.37731	27.34691
6.33	0	-1.31	49	28.51461	31.30313	27.29672
6.33	1.27	-1.31	50	28.49377	31.21626	27.29491
6.33	-0.635	-0.675	51	28.6653	31.853	27.32846
6.33	0.635	-0.675	52	28.57036	31.44366	27.32661
6.33	-0.635	0.595	53	28.89345	32.34942	27.32532
6.33	0.635	0.595	54	28.93893	32.46056	27.36815
6.33	-1.27	1.23	55	28.91063	32.54995	27.34156
6.33	0	1.23	56	28.85668	32.33055	27.36267
6.33	1.27	1.23	57	28.94735	32.63799	27.36839
6.33	-0.635	2.1825	58	28.87816	32.40024	27.35844
6.33	0.635	2.1825	59	28.86836	32.38092	27.33048
-1.29	0	-2.2625	60	27.9399	30.48407	26.98458
-1.29	-0.635	-1.945	61	28.10499	30.56632	27.17214
-1.29	0.635	-1.945	62	28.04636	30.52738	27.14444
-1.29	-1.905	-0.675	63	28.21405	30.84788	27.19841
-1.29	0	-0.675	64	28.18293	30.76573	27.12219
-1.29	1.905	-0.675	65	28.1244	30.7399	27.09247
-1.29	-1.905	0.595	66	28.15076	30.94093	27.06295
-1.29	0	0.595	67	28.04644	30.8322	26.99912
-1.29	1.905	0.595	68	28.2686	31.11285	27.12182
-1.29	-0.635	1.865	69	28.17943	31.01674	27.0635
-1.29	0.635	1.865	70	28.13401	30.97228	27.02637
-1.29	0	2.1825	71	28.0718	30.81081	27.03328
-10.18	-0.635	-2.2625	72	27.34514	29.50301	26.64094
-10.18	0.635	-2.2625	73	27.26457	29.40511	26.60804
-10.18	-1.27	-1.31	74	27.25876	29.42025	26.60789
-10.18	0	-1.31	75	27.30931	29.43856	26.62278
-10.18	1.27	-1.31	76	27.19776	29.34779	26.57622
-10.18	-0.635	-0.675	77	27.33496	29.58245	26.66182
-10.18	0.635	-0.675	78	27.30223	29.53465	26.60472
-10.18	-0.635	0.595	79	27.35594	29.72064	26.61174
-10.18	0.635	0.595	80	27.41363	29.81421	26.61983
-10.18	-1.27	1.23	81	27.44249	29.88568	26.61675
-10.18	0	1.23	82	27.44812	29.89587	26.6112
-10.18	1.27	1.23	83	27.3725	29.8374	26.55955
-10.18	-0.635	2.1825	84	27.38531	29.78238	26.55818
-10.18	0.635	2.1825	85	27.35752	29.71252	26.5782
-20.34	0	-1.945	86	26.50425	28.33162	26.03764
-20.34	-1.27	-0.9925	87	26.64796	28.49392	26.1505
-20.34	1.27	-0.9925	88	26.49833	28.32488	26.01306
-20.34	-1.27	0.9125	89	26.71344	28.6892	26.1857
-20.34	1.27	0.9125	90	26.68432	28.67429	26.12019

Table C–1. Thermocouple locations and Steady State Temperature Values for Test #11 [3.4129 W = 1 BTu; 2.54 cm = 1 in; (°C x 5/9) 2 = °F] (continued)						
Start Time: 6/17/02 13:52 End Time: 7/29/02 5:25			Elapsed Time (hrs)	457.58	735.37	925.53
			Power Setting	20	25	12
			Watts	3.37	5.251	1.246
X (cm)	Y (cm)	Z (cm)	Thermocouple	Temperature °C	Temperature °C	Temperature °C
-20.34	0	1.865	91	26.72483	28.72063	26.2074
-27.96	0	-1.6275	92	25.79383	27.58461	25.47964
-29.23	0	-0.04	93	25.98882	27.71624	25.56824
-27.96	0	1.5475	94	26.2274	27.99854	25.7759
26.65	0	-3.215	95	33.29305	38.58984	29.21745
26.65	0	-4.485	96	32.4748	37.38732	28.88287
26.65	0	-5.755	97	31.69784	36.25758	28.63701
26.65	0	-7.025	98	31.16803	35.47448	28.42392
26.65	0	-8.295	99	30.82316	34.91045	28.29403
26.65	0	-9.565	100	30.64996	34.64814	28.21037
16.49	0	-3.215	101	29.78418	33.45782	27.84938
16.49	0	-4.485	102	29.8383	33.50899	27.82711
16.49	0	-5.755	103	29.8019	33.4541	27.82755
16.49	0	-7.025	104	29.71667	33.29901	27.78339
16.49	0	-8.295	105	29.6335	33.17862	27.73594
16.49	0	-9.565	106	29.59864	33.06408	27.76657
26.65	0	10.755	107	29.97945	33.76126	27.8733
26.65	0	9.485	108	30.10077	33.92054	27.9749
26.65	0	8.215	109	30.21125	34.16321	27.9547
26.65	0	6.945	110	30.42156	34.45941	28.09561
26.65	0	5.675	111	30.71054	34.91332	28.2193
26.65	0	4.405	112	31.13308	35.70356	28.37377
26.65	0	3.135	113	31.78969	36.69422	28.65063
16.49	0	10.755	114	29.46079	32.8324	27.72905
16.49	0	9.485	115	29.44736	32.84034	27.72251
16.49	0	8.215	116	29.49873	32.96558	27.73126
16.49	0	6.945	117	29.53921	33.03182	27.74193
16.49	0	5.675	118	29.65556	33.26392	27.79137
16.49	0	4.405	119	29.7907	33.51558	27.85928
16.49	0	3.135	120	29.85397	33.61417	27.88386
-33	0	0	T1	25.7	25.5	26
-0.5	0	12.5	T2	26.8	26.5	26
-0.5	0	14.5	T3	27.8	29.6	26.8
33	0	0	T4	26.6	26.5	25.8
-32	0	7.5	T5	–	22.8	22.2

Table C–2. Thermocouple Locations and Steady State Temperature Values for Test #14 [3.4129 W = 1 BTu; 2.54 cm = 1 in; (°C x 5/9) 2 = °F]							
Start Time: 8/15/02 14:09 End Time: 10/1/02 9:05			Elapsed Time (hrs)	284.98	592.99	783.22	1088.93
			Power Setting	20	12	6	2
Thermocouple Location			Watts	3.37	1.246	0.343	0.057
X (cm)	Y (cm)	Z (cm)	Thermocouple	Temperature °C	Temperature °C	Temperature °C	Temperature °C
27.92	0	-0.675	1	52.14444	36.6067	28.604	25.33929
27.92	-1.27	1.23	2	52.78992	35.87604	28.08357	25.12291
27.92	1.27	1.23	3	44.54196	32.53519	27.0588	25.04298
24.11	-1.905	-0.675	4	38.51546	30.2109	26.62254	25.00461
24.11	1.905	-0.675	5	35.48307	29.48216	26.54546	25.06456
24.11	0	1.23	6	41.88054	31.59799	26.82949	24.97368
24.11	-0.635	2.1825	7	42.86834	31.64485	26.55181	24.83913
24.11	0.635	2.1825	8	34.97725	28.425	25.84402	24.82186
20.3	0	0.595	9	35.5464	28.41511	25.8052	24.81299
20.3	-0.635	1.865	10	35.75593	28.28692	25.69083	24.78532
20.3	0.635	1.865	11	36.0062	28.46065	25.82659	24.84208
16.49	0	-2.2625	12	30.15403	26.58571	25.39326	24.76043
16.49	-1.905	-0.675	13	30.55552	26.69186	25.38246	24.73331
16.49	1.905	-0.675	14	31.04156	26.77035	25.3855	24.74688
16.49	-0.635	0.595	15	32.67846	27.33929	25.51526	24.74173
16.49	0.635	0.595	16	32.11357	27.09081	25.41689	24.72734
16.49	0	1.23	17	31.94116	26.97363	25.42184	24.73708
12.68	-1.905	0.595	18	30.79189	26.5574	25.28997	24.65575
12.68	1.905	0.595	19	31.00315	26.59262	25.30259	24.70455
12.68	0	2.1825	20	30.31657	26.47748	25.28614	24.67939
6.33	-0.635	-2.2625	21	29.35693	26.27955	25.314	24.73687
6.33	0.635	-2.2625	22	29.31256	26.245	25.27529	24.72776
6.33	0	-1.31	23	29.47472	26.26122	25.26662	24.73137
6.33	-1.27	1.23	24	29.71799	26.20205	25.18235	24.65051
6.33	0	1.23	25	29.78456	26.23438	25.20927	24.64289
6.33	1.27	1.23	26	29.75891	26.26677	25.25455	24.68372
-1.29	0	-2.2625	27	28.60566	25.8868	25.08949	24.55896
-1.29	-1.905	-0.675	28	28.60221	25.82812	25.01534	24.50321
-1.29	1.905	-0.675	29	28.73937	25.8901	25.05943	24.56504
-1.29	0	0.595	30	28.7697	25.87138	25.03929	24.54344
-1.29	-0.635	1.865	31	28.83746	25.89222	25.05389	24.54023
-1.29	0.635	1.865	32	28.76848	25.87789	25.06015	24.53968
-10.18	-1.27	-1.31	33	27.85126	25.49355	24.86536	24.40622
-10.18	1.27	-1.31	34	27.83218	25.48931	24.84587	24.39215
-10.18	-0.635	0.595	35	27.94697	25.50177	24.86084	24.38968
-10.18	0.635	0.595	36	28.0298	25.51554	24.84855	24.37845
-10.18	0	1.23	37	28.005	25.48887	24.80044	24.35666
-10.18	-0.635	2.1825	38	27.9914	25.49098	24.82615	24.3846
-10.18	0.635	2.1825	39	28.02282	25.50914	24.83533	24.38646
-20.34	0	-1.945	40	26.90998	24.9502	24.50081	24.11389
-20.34	-1.27	0.9125	41	27.44776	25.22543	24.69559	24.3347
-20.34	1.27	0.9125	42	27.2975	25.09259	24.55434	24.21981
-20.34	0	1.865	43	27.30305	25.10341	24.59981	24.21334
-27.96	0	-1.6275	44	26.33648	24.45103	24.02713	23.6856
-29.86	0	-0.04	45	26.35107	24.42645	23.9925	23.66704
-27.96	0	1.5475	46	26.58757	24.62109	24.17705	23.78738

Table C–2. Thermocouple Locations and Steady State Temperature Values for Test #14 [3.4129 W = 1 BTu; 2.54 cm = 1 in; (°C x 5/9) 2 = °F]							
Start Time: 8/15/02 14:09 End Time: 10/1/02 9:05			Elapsed Time (hrs)	284.98	592.99	783.22	1088.93
			Power Setting	20	12	6	2
Thermocouple Location			Watts	3.37	1.246	0.343	0.057
X (cm)	Y (cm)	Z (cm)	Thermocouple	Temperature °C	Temperature °C	Temperature °C	Temperature °C
26.65	0	-3.215	47	35.04161	28.4796	25.89266	24.7374
26.65	0	-4.485	48	33.30888	27.76808	25.7156	24.74428
26.65	0	-5.755	49	32.49576	27.46045	25.59672	24.69922
26.65	0	-7.025	50	31.92546	27.22713	25.52848	24.67258
26.65	0	-8.295	51	31.55324	27.0961	25.54198	24.70004
16.49	0	-3.215	52	30.36642	26.58138	25.31429	24.60561
16.49	0	-4.485	53	30.40291	26.60903	25.32923	24.60992
16.49	0	-5.755	54	30.39752	26.63936	25.37081	24.62282
16.49	0	-7.025	55	30.37785	26.61955	25.35098	24.61384
16.49	0	-8.295	56	30.30412	26.61567	25.36763	24.64795
26.65	0	3.135	57	32.25414	27.29952	25.54636	24.65713
26.65	0	4.405	58	31.86095	27.16215	25.50583	24.66401
26.65	0	5.675	59	31.44565	27.01299	25.46297	24.64803
26.65	0	6.945	60	31.13681	26.90362	25.45241	24.65293
26.65	0	8.215	61	31.2667	27.04643	25.61473	24.99815
16.49	0	3.135	62	30.88595	26.83581	25.52539	24.91213
16.49	0	4.405	63	30.86793	26.83046	25.51304	24.87539
16.49	0	5.675	64	30.76774	26.76694	25.45102	24.8466
16.49	0	6.945	65	30.59721	26.67347	25.39838	24.74325
16.49	0	8.215	66	30.44546	26.59675	25.30308	24.65726
-33	0	0	T1	25.8	25.5	26.7	26.2
-0.5	0	12.5	T2	25.9	25.3	25.1	24.5
-0.5	0	14.5	T3	27.1	25.8	25.1	24.6
33	0	0	T4	27.2	25.3	25.2	24.6
-32	0	7.5	T5	21.3	20.9	20.9	20.8

Table C–3. Thermocouple Locations and Steady State Temperatures Values Measured for Test 16, Dry Test Phase. Values of Power Supplied to the Heater Cartridge Were 3.52 W [12.0 BTu/h] and 5.51 W [18.8 Btu/h] Test #16d and Test #16e. [3.4129 W = 1 BTu; 2.54 cm = 1 in; (°C x 5/9) 2 = °F]					
				Test 16d	Test 16e
x (cm)	y (cm)	z (cm)	Thermocouple ID	Temperature, °C	Temperature, °C
26.65	0	-3.215	1	52.10	65.41
26.65	0	-4.485	2	45.57	55.62
26.65	0	-5.755	3	42.06	50.34
26.65	0	-7.025	4	39.69	46.73
26.65	0	-8.295	5	37.75	43.76
26.65	0	-9.565	6	36.15	41.40
26.65	0	-1.31	7	89.13	119.20
26.65	0	1.865	8	58.21	74.21
26.65	0	2.5	9	50.79	63.23
26.65	0	3.135	10	47.21	58.57
26.65	0	4.405	11	43.45	53.01
26.65	0	5.675	12	40.56	48.67
26.65	0	6.945	13	38.41	45.40
26.65	0	8.215	14	36.81	43.02
16.49	0	1.865	15	43.56	53.66
16.49	0	2.5	16	38.16	45.24
-12.72	0	1.865	17	27.06	29.46
-12.72	0	2.5	18	26.06	27.57
16.49	0	3.135	19	37.38	43.98
16.49	0	4.405	20	36.09	42.00
16.49	0	5.675	21	34.94	40.23
16.49	0	6.945	22	33.84	38.54
16.49	0	8.215	23	33.22	37.60
-12.72	0	3.135	24	26.17	27.68
-12.72	0	4.405	25	26.10	27.47
-12.72	0	5.675	26	25.88	27.14
-12.72	0	6.945	27	25.82	27.02
-12.72	0	8.215	28	25.71	26.85
31.095	0	-1.945	29	50.17	61.64
33	0	-1.945	30	43.51	51.61
35.54	0	-1.945	31	32.15	34.72
26.65	0	11.3138	32	33.15	37.54
16.49	0	11.3138	33	30.99	34.20
-12.72	0	11.3138	34	25.00	25.81
26.65	-8.255	-0.04	35	37.05	43.00
16.49	-8.255	-0.04	36	33.82	38.33
-12.72	-8.255	-0.04	37	25.89	26.95
26.65	0	13.0918	38	32.19	36.09
16.49	0	13.0918	39	30.25	32.98
-12.72	0	13.0918	40	25.26	26.07
26.65	0	15.6318	41	24.79	24.77
16.49	0	15.6318	42	25.70	25.66
-12.72	0	15.6318	43	24.06	23.61
external			44	24.23	23.73